Title
Secondary Species Emission and Behavior for Electrospray Thrusters

Author
Uchizono, Nolan Michael

Publication Date
2022

Peer reviewed|Thesis/dissertation

UNIVERSITY OF CALIFORNIA
Los Angeles

Secondary Species Emission and Behavior for Electrospray Thrusters

A dissertation submitted in partial satisfaction
of the requirements for the degree
Doctor of Philosophy in Aerospace Engineering

by

Nolan Michael Uchizono

6/2022

ABSTRACT OF THE DISSERTATION

Secondary Species Emission and Behavior
for Electrospray Thrusters

by

Nolan Michael Uchizono
Doctor of Philosophy in Aerospace Engineering
University of California, Los Angeles, 6/2022
Professor Richard E. Wirz, Chair

Electrospray propulsion devices employ strong electric fields to extract high velocity droplets and molecular ions from a liquid propellant. When these constituents strike downstream surfaces, impact processes can lead to the emission of a diverse set of secondary species, including electrons, atomic ions, molecular ions, and subsidiary droplets. The objective of this research is to examine the emission and transport of secondary species in electrospray thrusters to understand the effects on thruster life, performance, spacecraft interactions, and terrestrial facility effects.

This dissertation presents theoretical, analytical, and experimental investigations of electrospray operation in vacuum facilities to show that secondary species emission (SSE) plays a significant role in the behavior of electrospray thrusters during ground testing. First, an analysis of SSE mechanisms and onset thresholds showed that SSE occurs in the regimes where electrospray thrusters commonly operate. Therefore, SSE must be carefully considered for accurate measurements and determination of performance and life.

A series of experiments were conducted to investigate the consequence of SSE on electrospray thruster operation. A beam target biasing experiment was conducted to demonstrate the impact of

SSE on thruster-to-facility coupling, which introduces significant uncertainty in thruster lifetime measurements. A novel "SSE probe" diagnostic was developed and used to obtain the first-ever angular distributions of positive and negative SSE yields for an electrospray thruster. An optical emission spectroscopy study was conducted to show that glow discharges observed in electrospray thrusters during vacuum operation are a consequence of SSE; this observation is in direct contrast to common postulations that glows are intrinsic to electrospray operation.

Two analytical models were developed to study SSE impact on thruster performance and lifetime. The first model was a one-dimensional heat and mass flux analysis of an ionic liquid ion source, which showed that SSE-induced Ohmic dissipation can significantly affect thruster performance. The second model, named the "Electrospray SSE Control-volume Analysis for Resolving Ground Operation of Thrusters" (ESCARGOT) invokes conservation of charge to derive a set of governing equations that describes the emission and transport of secondary species throughout an electrospray thruster and testing facility. The model relies on geometric factors obtained from numerical simulations, and experimentally-obtained SSE yields to correct for SSE-induced current measurement uncertainty in thruster performance and life testing. Therefore, the ESCARGOT model serves as an important link to determine accurate in-space thruster life and performance predictions based on terrestrial qualification testing.

Overall, this work reveals the critical importance of SSE to electrospray thruster performance, life, facility effects, and space interactions; and provides both experimental and modeling techniques to assess their impact for a range of operating and test conditions.

The dissertation of Nolan Michael Uchizono is approved.

Daniel Q. Eckhardt

John K. Ziemer

Tim S. Fisher

Ann R. Karagozian

Mitchell R. Spearrin

Richard E. Wirz, Committee Chair

University of California, Los Angeles

6/2022

TABLE OF CONTENTS

List of Figures

List of Tables

ACKNOWLEDGMENTS

I would first like to thank my advisor, Prof. Richard Wirz, for providing guidance and opportunities to succeed throughout my time at UCLA. In addition to your role as my mentor, thank you for sharing your experiences as a father, and for our many philosophical discussions on the space and electric propulsion. Your insights have been invaluable in helping me plan my future. I am also grateful to have a fantastic graduate committee: Prof. Ann Karagozian, Prof. Tim Fisher, Prof. Mitchell Spearrin, Dr. John Ziemer, and Dr. Dan Eckhardt. It gives me great pride to say that I have been your student.

Thank you to Ian Allfrey, Travis Valentine, Nathan Bolte, and Tommy Roche at TAE Technologies for introducing me to pulsed power and the wonderful world of plasma physics, and for tolerating my penchant for never putting tools away. To the AFRL alumni - Carrie Hill, Michael Holmes, Robbie Lobbia, and Sasha MacDonald: thank you for your mentorship and friendship, and for encouraging me to pursue a PhD. I owe a great deal to Dan Eckhardt for lending invaluable guidance over the years, and for being a major advocate in cultivating my career. I am grateful to Adam Collins for his mentorship, for spending an obscene amount of time listening to me troubleshoot my models, and for going above and beyond in helping me collect data for my dissertation. I also owe my sincerest thanks to Colleen Marrese-Reading, Steven Arestie, and John Ziemer at JPL for their technical mentorship - I am privileged to have had the opportunity to work with you on the CMT development effort.

I am grateful to the Plasma & Space Propulsion Lab members for their camaraderie and support over the years. Between the absurd philosophical discussions (e.g. “topological isomorphism of sandwiches”), skillful crafting of backronyms, and sharing of favorite restaurants and recipes, you all have made the graduate school experience memorable and fun. Putzing around in the lab, investing unhealthy amounts of time working on “petty projects”, and following up with cheeky pints will be the thing I miss most about graduate school. Chris Dodson, Gary Li, Stephen Samples, Ani Thuppul, Peter Wright, Angelica Ottaviano, McKenna Davis-Breddan, Mary Konopliv,

Henry Huh, Shehan Parmar, and Patrick Crandall - working with all of you has made me a better researcher. I am proud to call you my colleagues and friends.

I would like to thank my in-laws, Kathy and Pope Moseley for generously offering space in their home through the Winter 2020 surge of the COVID-19 pandemic. It was in those months that I completed the first few chapters of this dissertation. Caring for our newborn daughter during those months was immeasurably less stressful thanks to your hospitality. Thank you for your support throughout my PhD experience, especially for taking so much time to look after Nova. Pope, I genuinely appreciate the feedback on my fellowship proposals, and the advice on grant writing.

I dedicate this work to the three most important women in my life: my mother (Rachel), my wife (Ariana), and my daughter (Nova). Mom: I appreciate that you overlooked the destruction of your lawn to let me play "rocket scientist" with vinegar and baking soda rockets in the back yard. Thank you for nurturing, supporting, and encouraging me throughout every stage of my life. Ariana: I unequivocally could not have completed my PhD without you. Thank you for everything. For your unwavering and enthusiastic support of my research over the years, for your compassion and being a shoulder to cry on when my experiments weren't working, for being my "rubber ducky" when I needed to bounce ideas off of someone, for not once getting sick of me throughout our time spent in COVID lockdown, for proofreading my papers and listening to my presentations, for being my sixth unofficial funding agency, for being such an amazing mother to our daughter - for everything, I am so grateful. I love you so much. Nova: Thank you for giving me such a beautiful new context to view the world. Your persistence and focus have been an inspiration to me as I worked on my dissertation. Thank you for your patience while I finish my graduate research, and for being such a wonderful daughter. You fill your parents with so much love and happiness.

The research conducted in this dissertation was supported by the NASA Space Technology Graduate Research Opportunity under Grant No. 80NSSC20K1186.

VITA

2012	B.S. (Electrical Engineering), Cal Poly San Luis Obispo.
2012 - 2013	Electronics Technician II, Meggitt Defense Systems, Inc.
2013 - 2014	Pulsed Power Engineer, Tri Alpha Energy, Inc.
2014 - 2017	Electric Propulsion Research Engineer III, Air Force Research Laboratory.
2017 - 2020	Graduate Student Researcher, Plasma & Space Propulsion Laboratory, UCLA
2019	M.S. (Mechanical Engineering), UCLA.
2019	Teaching Assistant, MAE 250C Compressible Flow, UCLA
2020 - 2022	NSTGRO Fellow, UCLA Plasma and Space Propulsion Lab, UCLA.
2021 - 2022	Visitng Technologist, NASA Jet Propulsion Laboratory.

PUBLICATIONS

Facility effect characterization for electrospray thruster systems via charge conservation. N. M. Uchizono and R. E. Wirz, Journal of Electric Propulsion, (2022) In Review

A diagnostic for quantifying secondary species emission from electrospray devices. N. M. Uchizono, R.E. Wirz, A. L. Collins, C. Marrese-Reading, S. M. Arestie, and J. K. Ziemer, Review of Scientific

Instruments, (2022) In Review

Positive and negative secondary species emission behavior for an ionic liquid electrospray. N. M. Uchizono, C. Marrese-Reading, S. M. Arestie, A. L. Collins, J. K. Ziemer, and R. E. Wirz, Applied Physics Letters, (2022) In Review

Emission spectra of glows produced by ionic liquid ion sources. N. M. Uchizono, P. L. Wright, A. L. Collins, and R. E. Wirz, Applied Physics Letters, (2022) In Review

The role of secondary species emission in vacuum facility effects for electrospray thrusters. N. M. Uchizono, A. L. Collins, C. Marrese-Reading, S. M. Arestie, J. K. Ziemer, and R. E. Wirz, Journal of Applied Physics 130 (14), 143301 (2021)

Mass flux and current density distributions of electrospray plumes. A. Thuppul, A. L. Collins, P. L. Wright, N. M. Uchizono, and R. E. Wirz, Journal of Applied Physics 130 (10), 103301 (2021)

Comment on 'Jet propulsion by microwave air plasma in the atmosphere'. Peter Wright, Stephen Samples, Nolan Uchizono, and Richard Wirz. AIP Advances 10, 099101 (2020)

Emission Modes in Electrospray Thrusters Operating with High Conductivity Ionic Liquids. Nolan M. Uchizono, Adam L. Collins, Anirudh Thuppul, Peter L. Wright, Daniel Q. Eckhardt, John Ziemer, and Richard E. Wirz. MDPI Aerospace 7, no. 10: 141. (2020)

Tunable reflectionless absorption of electromagnetic waves in a plasma-metamaterial composite structure. Nolan Uchizono, Stephen Samples, and Richard Wirz. 2020 Plasma Sources Sci. Technol. 29 085009

CHAPTER 1

Introduction

1.1 Miniature Spacecraft and Micropropulsion

In 1999, California Polytechnic State University San Luis Obispo and Stanford University jointly developed the standardized small satellite form factor called the "CubeSat" [15]. In the ensuing two decades, the technical and economical accessibility of CubeSats have driven a renaissance in small spacecraft development and flight, creating a technology pull for low-power and high-efficiency propulsion capabilities. The total number of launched small-scale satellites (0.1 kg to 50 kg) has increased exponentially since the inception of the CubeSat, as shown in Figure 1.1. Notably, the number of small satellites equipped with propulsion is a fraction of the total number of satellites.

The lack of propulsion on CubeSats can be attributed to three factors: (1) limited lifetime of space-rated CubeSat components and therefore no need for propulsion systems, (2) Range Safety limitations on pressurized or energetic propellants to protect primary payloads, and (3) technical challenges in miniaturizing mainstream propulsion technologies. With improvements in the lifetime of off-the-shelf CubeSat subsystems, propulsion capability has become a critical area of need for increasing the mission capabilities of CubeSats [16]. Furthermore, in an attempt to mitigate the rise in orbital space debris, the Federal Communications Commission (FCC) recently proposed a requirement for any spacecraft operating above 400 km to employ some form of propulsion [17]. The propulsion requirement would ensure that all spacecraft have a minimum capacity to perform limited collision avoidance maneuvers, or end-of-life deorbiting. Due to stakeholder feedback,

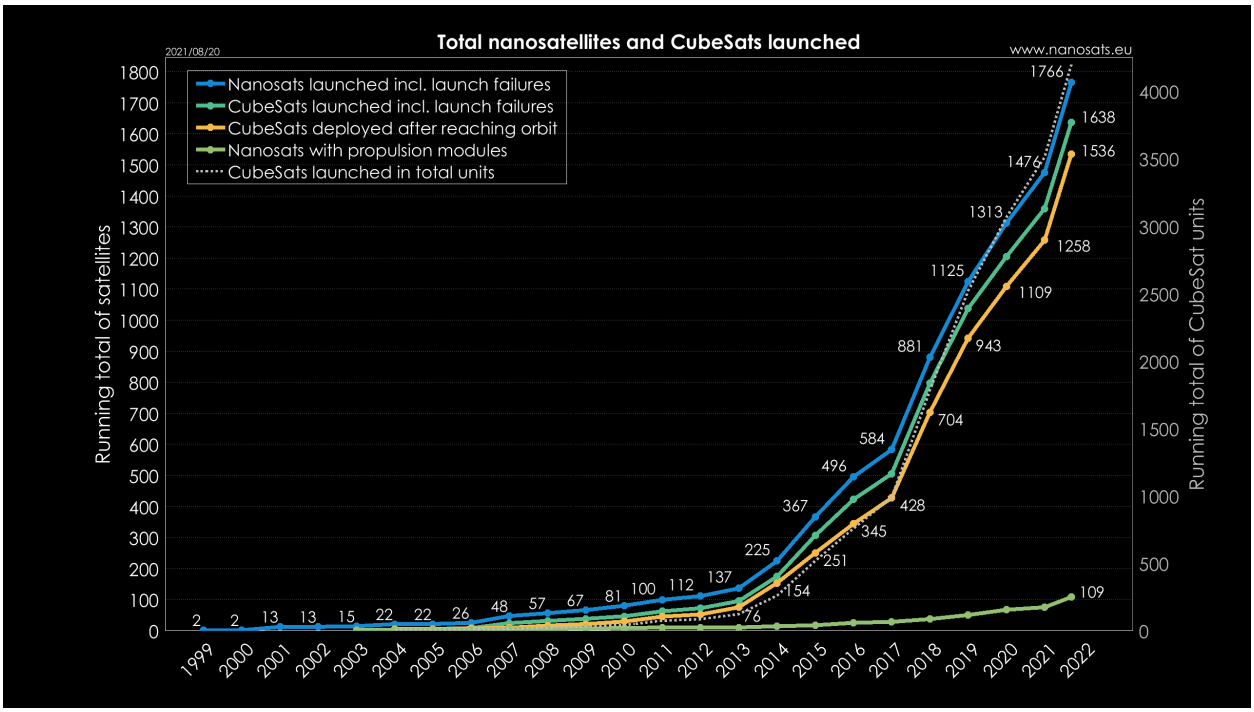

Figure 1.1: Running total of CubeSats launched over time. CubeSats generally lack propulsion capabilities, but are becoming more popular as mission needs emerge. Figure credit from Erik Kulu's Nanosat Database [1].

the FCC pushed the orbit threshold for the propulsion requirement to 600 km. The space debris issue is unsustainable given current community practices [18], thus a universal propulsion requirement is inevitable. Given the mission-pull, and the policy-push, micropropulsion is poised for unprecedented growth, yet the space community is not currently equipped to meet the demand for CubeSat-scale micropropulsion.

Electrospray thrusters are attractive as primary propulsion systems for meeting future spacecraft compliance needs, and for enabling high-risk/high-reward scientific missions on CubeSat platforms [19]. Electrosprays are inherently microscale devices, consuming extremely small amounts of propellant and power. Since electrosprays rely on non-energetic, liquid-phase propellants, Range Safety and primary payload stakeholder concerns are ameliorated.

1.2 Electrospray Propulsion

Electrosprays operate by applying a strong electrostatic field to a conductive liquid meniscus. The electric traction force balances against surface tension, deforming the curved meniscus into a cone [20]. The electric field is enhanced at the cone's apex due to its tight radius of curvature, where an electrically-forced jet forms in response to the field singularity, extracting fluid from the meniscus [21]. The electrified jet is an inherently unstable flow that may undergo different electrohydrodynamic instabilities, leading to breakup of the jet into droplets or clusters. The development of electrospray technology for the application of mass spectrometry of biological macroparticles was awarded the Nobel Prize in Chemistry in 2002 [22, 23], and has found unique applications via electrospinning fabrication of nanoscale fibers [24, 25], or thin film deposition [26]. The subject of this dissertation is the development of another compelling application for electrosprays - spacecraft propulsion.

Electrospray thrusters are a class of micro-scale electric propulsion device that produce thrust by electrostatically emitting and accelerating charged species from a liquid-phase propellant. Electrosprays were initially developed for propulsion applications in the 1960's through the mid-1970's [27], and again since the early-2000's [28, 29, 30, 31]. The latter development effort has sought to exploit electrosprays for low-noise disturbance reduction systems enabling future space-based observatories, such as the Laser Interferometer Space Antenna (LISA) and Habitable Exoplanet Observatory (HabEx) [31, 32, 33]. A vital area of research for electrospray propulsion to support space science missions is the improvement of electrospray thruster lifetime to meet mission requirements [33]

When electrospraying, the conical shape of the meniscus is sustained by feeding fluid to the emission site through several different methods, depending on the desired thruster performance [34, 35]. An electrospray thruster that provides very high specific impulse ideally operates in the "purely-ionic regime" where the thruster only emits monomer ions, and is often referred to as an ionic liquid ion source (ILIS) or liquid-ion thruster [36, 3]. ILIS thrusters are passively fed,

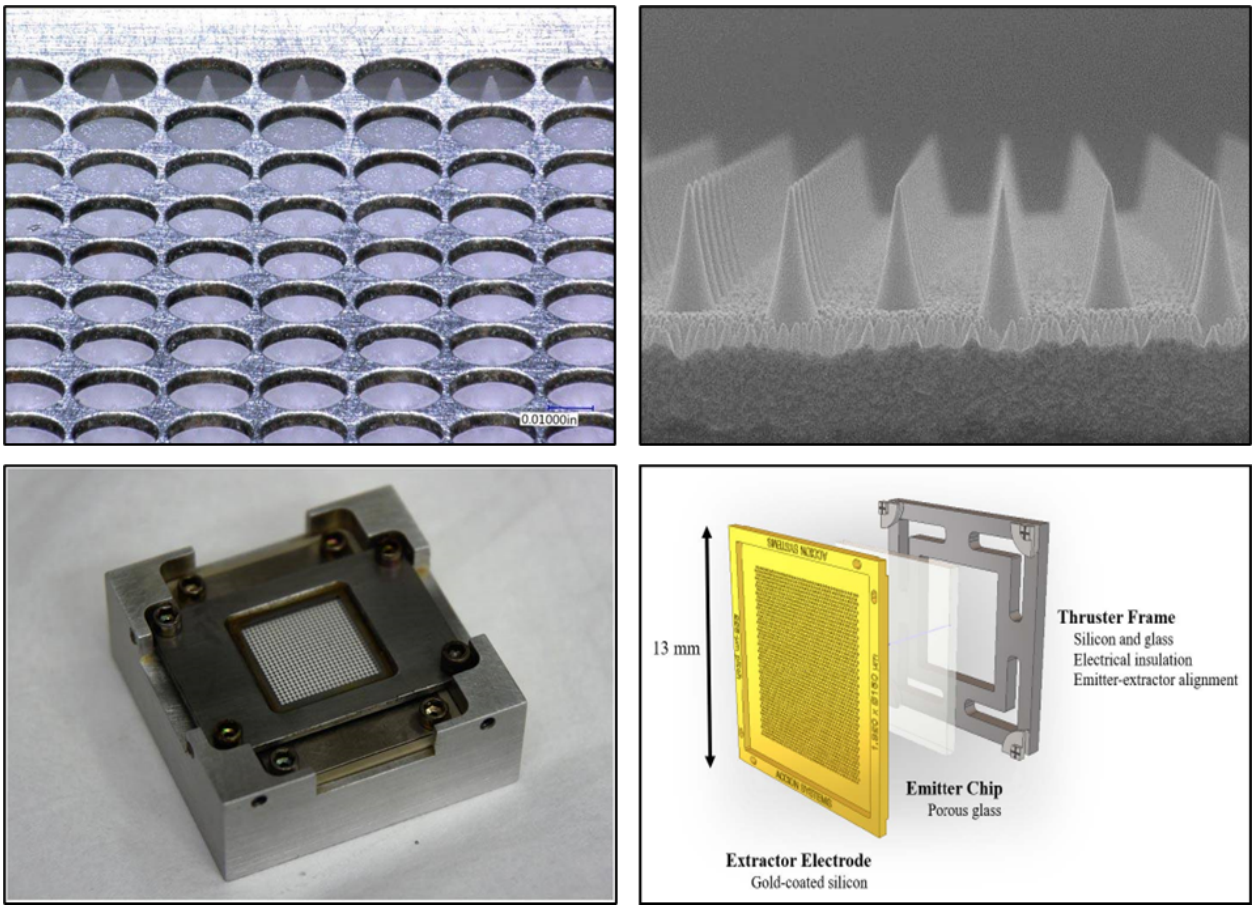

Figure 1.2: Two examples of ionic liquid ion source (ILIS) thrusters that employ emitters made from sharpened porous media. The left two images are of the Air Force Electrospray Thruster Series 2 (AFET-2) [2, 3]. The right two images are of the Accion TILE thruster [4].

consisting of either an externally-wetted needle emitter [36], or a machined porous material [37]. Figure 1.2 shows two examples of ILIS thrusters that have emitters made of a machined porous medium. A separate, yet closely-related technology called liquid metal ion sources (LMIS) or field-effect electric propulsion (FEEP) makes use of liquid metals to produce positively-charged ions [38, 39, 13].

The discrepancy between the high predicted efficiency of ILIS thrusters (80% to 91%) [40, 41] and their lower actual efficiency (24% to 60%) [42, 3] is not yet fully understood. A major performance-limiting mechanism for ILIS thrusters has recently been identified as "anomalous

mass loss" [3]. Room temperature ionic liquids have negligible vapor pressures, so ILIS thrusters should ideally have a 100% mass utilization efficiency, hence any unexplained neutral mass loss from an ILIS thruster is considered "anomalous". In addition to performance limitations, ILIS thrusters have relatively short lifespans. Prior research efforts have established emitter arcing, propellant impurities, and electrochemical effects as key contributors to thruster lifetime limitations [43, 44, 45, 46]. These effects have been ameliorated through the use of emitter bias polarity alternation, distal electrodes, and appropriate conditioning and handling of propellant to push state-of-the-art ILIS thrusters to lifetimes of $\sim$500 hours [47, 48]. Flight lifetimes for ILIS thrusters have not been publicly disclosed. The root cause of persisting ILIS thruster lifetime limitations remains unresolved.

Higher thrust-to-power ratio can be achieved at the cost of lower specific impulse by operating an electrospray in droplet-mode, where the thruster ideally emits a monodisperse population of droplets. Droplet-mode thruster feed systems contrast from their ILIS thruster counterparts in that propellant is actively-fed via capillary needle emitter [49, 50]. Two examples of capillary droplet-mode thrusters are shown in Figure 1.3. To date, droplet-mode thrusters are considered the most technologically matured embodiment of electrospray propulsion, given their successful flight on the LISA Pathfinder mission [31]. While demonstrated lifetimes for droplet-mode thrusters ($\sim$3,400 hours) exceed those of ILIS thrusters, they still fall short of the $>$40,000 hours needed to meet mission requirements for LISA or HabEx. The main life-limiting mechanism for droplet-mode thrusters has been identified as overspray, which causes mass flux impingement on the extraction and acceleration grids [51]. Strategies for improving droplet-mode thruster lifetime includes characterizing the causes of overspray, increasing electrode capacity to absorb propellant, and minimizing lifetime uncertainty by improving model and measurement fidelity [52].

All electrospray plumes have polydisperse populations of charged species consisting of single ions, oligomeric clusters, and droplets [53]. SSE behavior is highly dependent on the nature of the incident species, so plume polydispersity will affect which secondary species we expect to observe. For ILIS thrusters, polydispersity influences thruster efficiency, where a plume con-

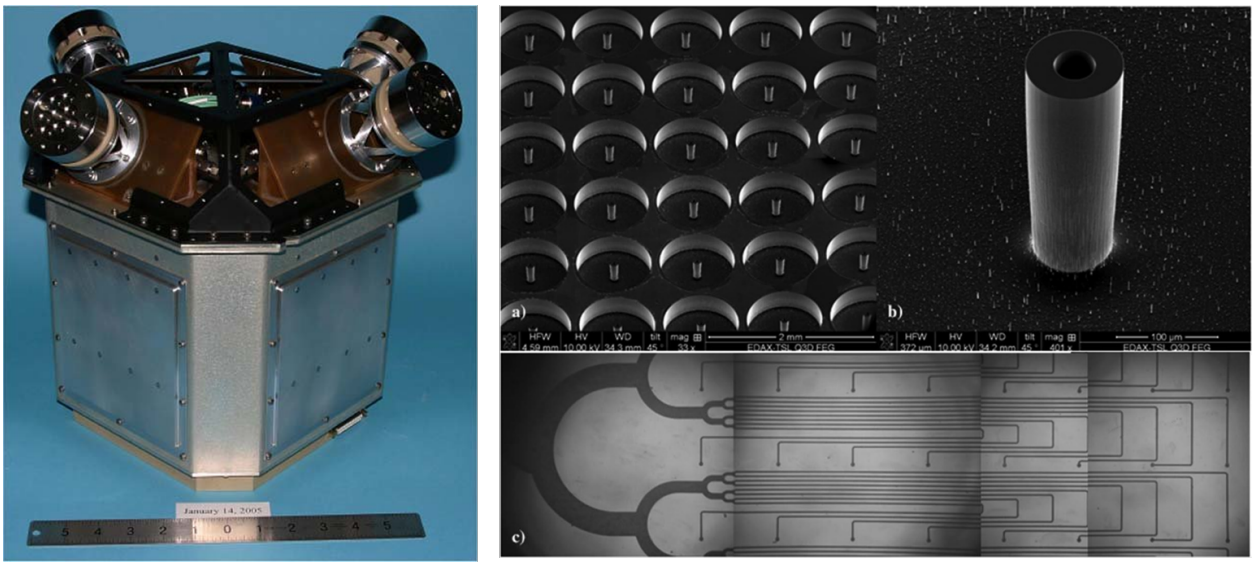

Figure 1.3: Two examples of droplet-mode thrusters that rely on actively-controlled flow through capillaries. The left image is of the Busek Colloid MicroNewton Thruster [5, 6]. The right images show micrographs of the capillaries and propellant channels of a micro-fabricated electrospray thruster [7].

sisting entirely of monomers is desired. The presence of droplets in ILIS thrusters is detrimental to performance [54], yet largely avoidable with appropriately designed porous substrates [3, 35]. In droplet-mode thrusters, polydispersity contributes to plume expansion and impingement on the electrodes, which detrimentally affects thruster life [55, 56, 51, 57]. A small fraction of solvated ions are emitted naturally as a consequence of charged droplet dynamics in the plume, yet the contribution of ion emission to thruster performance is negligible [58, 55, 57]. Although droplets constitute the majority of mass flux in the plume, ions may contribute to a non-negligible amount of current in droplet-mode electrosprays (as high as 15% of the plume current [58])

1.3 Research Motivation: Facility Effects and Spacecraft Interactions

Electric propulsion (EP) system usage on spacecraft has increased considerably over the last decade due to the need for enhanced mission flexibility and longer mission lifetimes. Applications that leverage EP range from large commercial satellite constellations [59], to advanced sci-

entific [32] and human exploration missions [60]. With increased demand for EP devices comes the need to accurately predict, test, and evaluate their performance and lifetime. The "test-like-you-fly" paradigm is an approach that seeks to recreate the operational environment as closely as possible to reduce the risk of on-orbit failure [61]. While test-like-you-fly is considered a core philosophy of spacecraft systems integration, it may be prohibitively challenging to adequately emulate Low-Earth Orbit or Geostationary environments in terrestrial facilities [62]. For example, Hall effect thruster behavior and lifetime are highly dependent on the ambient neutral gas pressure [63, 64, 65, 66, 67, 68], yet developing a vacuum facility that can achieve Low-Earth Orbit pressures ($\sim$10 nPa to 700 nPa [69]) while processing the flow of exhausted propellant is technically and economically unfeasible. Subsequently, a heavy emphasis has been placed on improving first-principles modeling for performance and life prediction, as well as advanced on-orbit diagnostics for evaluating thruster health. "Facility effects" have been the subject of extensive study for Hall effect thrusters due to thruster sensitivity to background pressure and electrical coupling effects [68, 70, 71]. However, the study of thruster-facility interactions with electrospray devices is still in its infancy.

A critical consideration for EP systems is the interaction between the thruster and spacecraft. Mission success is paramount, so it is necessary to fully understand how a thruster may influence the behavior of other subsystems. For EP devices, spacecraft interactions may entail electromagnetic interference (EMI), spacecraft charging, and plume interception [72]. Electrospray thrusters are quiescent electrostatic devices, so the EMI introduced by an electrospray is negligible, especially compared to Hall effect thrusters. For all EP systems, particle-surface interactions caused by impingement of the plume on downstream surfaces can lead to erosion or charging of spacecraft components [73, 74, 75]. Electrospray thrusters rely on the acceleration of conductive liquid propellants, so plume impingement on spacecraft components is particularly concerning, as it may lead to shorting or contamination of the spacecraft.

The research discussed herein will demonstrate how “secondary species emission” (SSE) is the main mechanism through which electrospray thrusters interact with ground testing facilities,

and a major consideration for spacecraft interactions. In contrast to the term "secondary emission" that is commonly used to discuss secondary electron emission [76], SSE includes the ejection of secondary electrons, atomic ions, molecular ions, oligomeric clusters, and droplets. Facility effects must be appropriately taken into account when performing qualification testing of electrospray thrusters, or when attempting to experimentally validate numerical models. Accordingly, the objective of the presented work is to rigorously examine SSE in the context of electrospray propulsion.

1.4 Dissertation Overview

Chapter 2 presents a review of literature and evaluation of onset thresholds, showing that SSE is always present when conducting ground testing of an electrospray thruster. Chapter 3 examines the consequences of SSE on electrospray thruster testing in terrestrial facilities. Experimental results show how SSE generates currents that cause thruster-to-facility coupling, contributing to considerable measurement uncertainty during testing. A novel diagnostic is presented for both measuring SSE-corrected plume currents, and quantifying the spatial distribution of SSE within an electrospray plume. Post-testing microscopy of surfaces exposed to electrospray plumes confirms the onset of SSE phenomena discussed in Chapter 2. A heat and mass flux model tests the hypothesis that SSE-induced Ohmic dissipation contributes to performance and lifetime limitations in electrospray thrusters. The origins of glow in electrospray thrusters are discussed, and arguments are presented that photon emission cannot be caused by the evaporation of ions. An experimental study is presented that indicates SSE processes are responsible for electrospray thruster glow. Chapter 4 presents a formalism for describing SSE transport in an electrospray testing facility. The formalism is used to derive the Electrospray SSE Control-volume Analysis for Resolving Ground Operation of Thrusters (ESCARGOT) model, which may be used to resolve discrepancies between experimental measurements and computational modelling results. Chapter 4 also describes the computational and experimental methods used to determine the two major parameters employed by the

ESCARGOT model: geometric factor and SSE yields. Chapter 5 presents a series of suggestions for mitigating facility effects for electrosprays. Chapter 6 reiterates the objective of the proposed work, summarizes the current findings, and suggests future work.

CHAPTER 2

Theory of Secondary Species Emission (SSE)

SSE is a general term encompassing the many complex interfacial phenomena initiated by the high-velocity impact of charged species on a solid or liquid surface [77]. SSE can be categorized into two general classes: ion impact effects, and droplet impact effects. Ion impact effects consist of: (1) polyatomic ion-induced electron emission (IIEE), (2) sputtering, and (3) molecular dissociation. Droplet impact effects consist of: (1) splashing, and (2) shock-induced desorption. SSE results in a diverse population of secondary species, including electrons, ions, oligomeric clusters, and droplets. The charge state of secondary species may be positive, negative, or neutral. The following chapter consists of discussion of the different identified SSE mechanisms, and presents thresholds for their respective onset in the context of electrospray propulsion.

2.1 Ion Impact Effects

2.1.1 Polyatomic Ion-Induced Electron Emission (IIEE)

Secondary electron emission describes the liberation of an electron due to an incident charged particle [76]. The energy distributions of electrons emitted via IIEE are effectively independent of primary particle energy and species, and peak at less than 10 eV [78, 79]. The molecular ions produced by electrospray devices exhibit higher electron emission yields than monatomic ions, with yield as high as 10's to 100's of electrons per incident particle [80]. Polyatomic IIEE has been extensively studied for impact energies on the order of 10 keV to 1000 keV [81, 82, 83, 84, 85], whereas electrospray thruster energies are on the order of 1 keV to 10 keV [86, 36, 37]. Magnusson

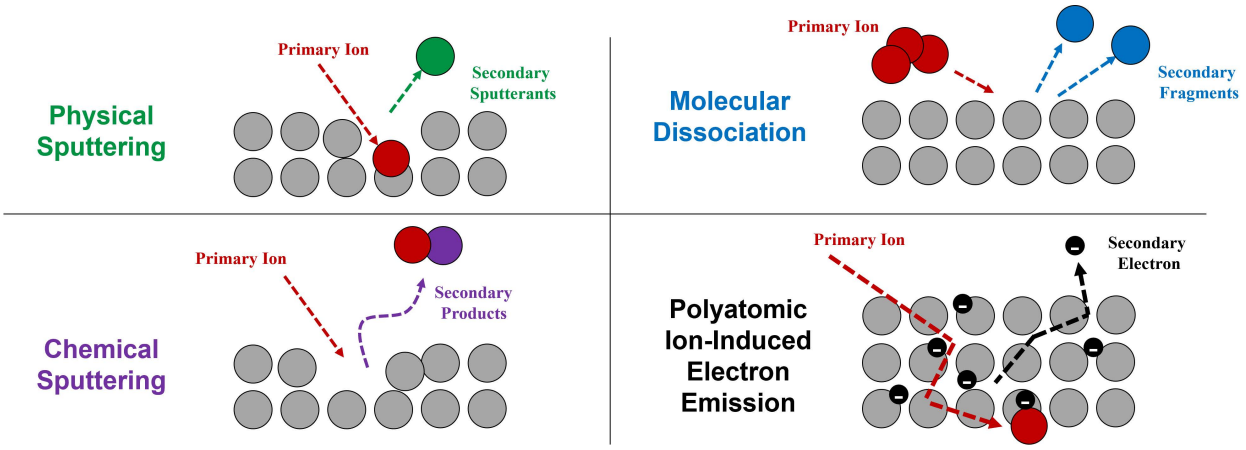

Figure 2.1: Diagrams representing different ion impact effects that occur when an electrospray molecular ion strikes a surface.

et al. [87] provide a detailed review of the physical mechanisms that contribute to polyatomic IIEE in the regimes relevant to electrospray thrusters, as well as a comparison of semi-empirical and analytical models predicting secondary electron yield.

2.1.2 Sputtering

Monatomic ion impacts on solid surfaces may liberate material from the substrate in a process generally referred to as "sputtering". Collision cascades caused by an impact may induce electronic excitation or ionization as electrons rapidly transition from valence bands in the target surface to eigenstates of liberated atoms [88, 89]. Hence, material released from a solid surface (i.e. sputterants) can have a positive, negative, or neutral charge state. Electronegative primaries are more likely to produce positive secondary sputterants, and electropositive primaries are more likely to produce negative secondary sputterants [88]. For non-reactive noble gases, sputtering is dominated by momentum and energy transfer alone. However, chemically-reactive primary ions (i.e. hydrogen or oxygen) cause "chemical sputtering", where the main form of material removal occurs via chemical reaction and subsequent evaporation of volatile byproducts [90, 91].

2.1.3 Molecular Dissociation

Molecular ion impact mechanics are unique from monatomic impacts in that molecular ions have more degrees of freedom to dissipate energy in the impact process [92, 91]. Therefore, in addition to sputtering of the target material, the incident molecular ion may also undergo several processes that result in a diverse set of species that contribute to the ejected secondary population. Collision-induced dissociation or surface-induced dissociation occur when the kinetic energy of an incident molecule is converted into internal energy during an impact, cleaving bonds and dissociating the molecule into smaller fragments [93, 94, 95]. Different types of molecular dissociation may result in either positive, negative, or neutral secondary species. Homolytic dissociation will result in the production of two neutral free radicals, whereas heterolytic dissociation will result in a cation/anion pair [96]. Resonant or dissociative electron capture of neutral particles is plausible either from metal donors in the target, or from secondary electrons present at the impact site [97, 98, 99]. Depending on the chemical composition of incident molecule and surface material, protonation/deprotonation and formation of salts due to adduction of the surface material also contribute to the secondary population [99]. While it's clear that positive, negative, or neutral SSE may be induced by molecular ion impacts, further study is necessary to identify the chemical composition of secondary species and characterize their emission properties, such as yield and charge-to-mass ratio.

2.1.4 Onset Thresholds for Ion Impact Effects

Magnusson et al. used the "TRansport of Ions in Matter" (TRIM) software to evaluate stopping power of incident species, finding that EMI^+ cations impacting stainless steel have a threshold of 49 eV for onset of electron emission, and 1.32 keV for unity electron yield. Owing to the kinetic emission assumption and neglect of intramolecular dynamics, it is reasonable to divide these values by the molecular mass of the cation (i.e. 111 u for EMI^+) and use the specific energy to generalize the threshold to anions and clusters. Specific energy of emitted species is calculated assuming no

loss in the potential energy during acceleration, giving a straightforward relationship of:

$$e = \frac{q}{m_s}\phi_A, \tag{2.1}$$

where e is specific energy, q is charge, ϕ_A is accelerating potential, and m_s is the species mass. Accelerating potential is evaluated as

$$\phi_A = \phi_{em} - \phi_{TC}, \tag{2.2}$$

where ϕ_{em} is the emitter bias and $\phi_{TC} \approx 400\,\mathrm{V}$ is the voltage drop across the Taylor cone [56]. Figure 2.3 shows the specific energy of monomers and dimers for [EMI]Im and [EMI]BF_4 as a function of accelerating potential, along with the IIEE onset thresholds. Onset of electron emission occurs at $0.44\,\mathrm{eV\,u^{-1}}$ (red dashed line), and unity electron yield occurs at $11.89\,\mathrm{eV\,u^{-1}}$ (blue dashed line).

The $0.44\,\mathrm{eV\,u^{-1}}$ onset threshold is sufficiently low that polyatomic IIEE should always contribute to SSE in ILIS thrusters. Droplet-induced electron emission has not been conclusively observed, but it is likely negligible due to the extremely high mass of droplets compared to ions, resulting in very low specific energies. However, the invariable presence of ions in the plume of droplet-mode electrospray thrusters implies that secondary electrons may occur in this class of thruster, as well.

The thresholds for onset of secondary ion production due to sputtering and dissociation are reported in literature as $1\,\mathrm{eV\,u^{-1}}$ (black dashed line in Fig. 2.3), though suppressed levels of fragmentation may occur between $0.1\,\mathrm{eV\,u^{-1}}$ and $1\,\mathrm{eV\,u^{-1}}$ [100, 101, 102, 103]. The origin of fragmentation thresholds in literature are unclear, but appear to arise empirically based on the observation of fragmented species in mass spectrometry data. The cluster dissociation threshold is reported in the controlled deposition community as 1 eV per atom [104, 105, 106], which is ultimately a lower threshold for dissociation than those reported in the mass spectrometry community owing to the large atomic masses of cluster constituents.

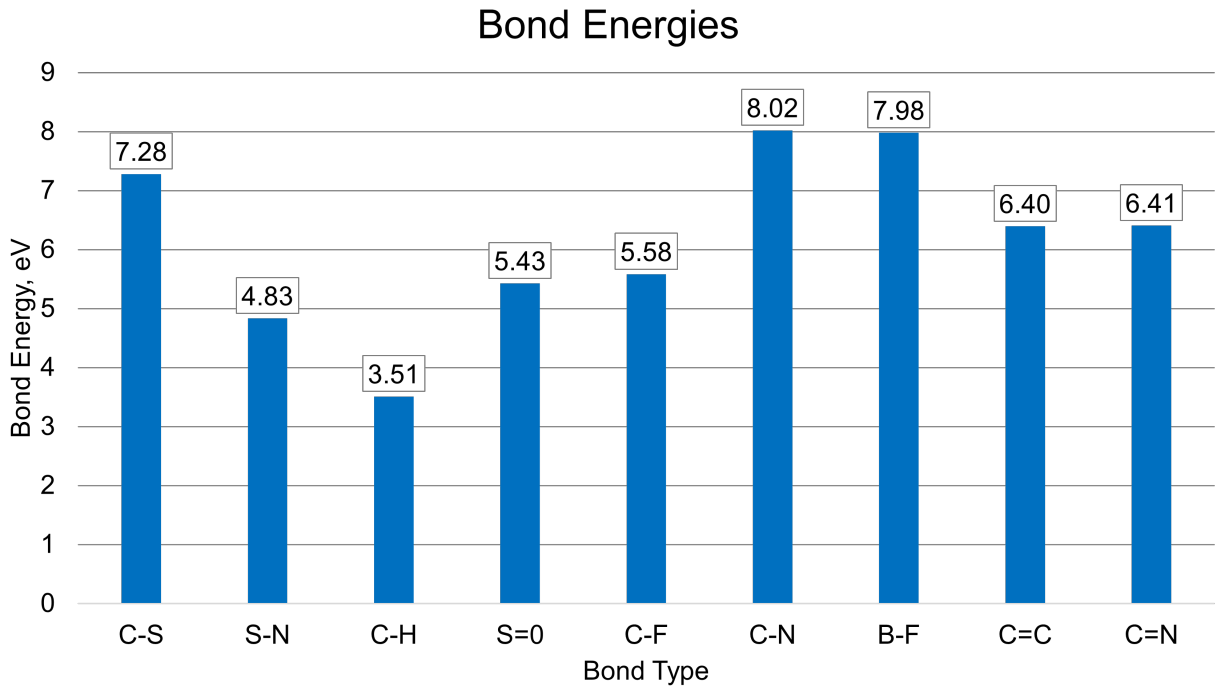

Figure 2.2: Bond energies for each atomic bond within the [EMI]Im and [EMI]BF_4 ionic liquid propellants.

Neglecting the specific chemical pathways of dissociation, a simplified model of the dissociation threshold can be obtained by considering the energy conservation of a molecule impacting a surface. A classical molecular model treats atoms and bonds as masses interconnected by springs. It is reasonable to assume that all kinetic energy is converted to internal energy of the molecule during impact. The timescale of an ion or cluster impact is on the order of >1 ps [107], which is much greater than molecular vibrational timescales of ∼10 fs to 100 fs [108], so it is reasonable to further assume that kinetic energy from impact equalizes rapidly between the bonds. In the described scenario, an impacting molecule evenly distributes energy among its bonds until the weakest bond breaks, which represents the dissociation threshold. The plot in Figure 2.2 shows the bond energies for each atom in [EMI]Im and [EMI]BF_4, with the C−H bond having the lowest energy at 3.51 eV and the C−N and B−F bonds having the highest energy at ∼8 eV.

The $[EMI]^+$ cation has 12 bonds and a molecular mass of 111 u, the Im^- anion has 19 bonds

and a molecular mass of 280 u, and the BF_4^- anion has 4 bonds and a molecular mass of 110 u. Assuming the weakest bond energy for each respective ion, the specific energy threshold may be estimated by

$$e_{th} = \frac{NE_B}{m_{ion}}, \tag{2.3}$$

where N is the number of bonds in the molecule, E_B is the bond energy, and m_{ion} is the mass of the molecular ion. Substituting the above values into equation 2.3 gives e_{th} of $0.66\,\mathrm{eV\,u^{-1}}$, $0.32\,\mathrm{eV\,u^{-1}}$, and $0.37\,\mathrm{eV\,u^{-1}}$ for $[EMI]^+$, Im^-, and BF_4^-, respectively. Estimated values using the presented threshold model agree well with empirically observed thresholds described above.

It is worth emphasizing again that the described processes may cause positive, negative, or neutral species. The existence of oppositely-charged secondary species is important to consider, since the secondary species will backstream to the thruster and be attracted to the emitter bias. Since ion emission is present in all electrospray devices, and the specific energy threshold for onset of secondary ion emission is sufficiently low, it likely contributes to SSE in all electrospray ground testing situations.

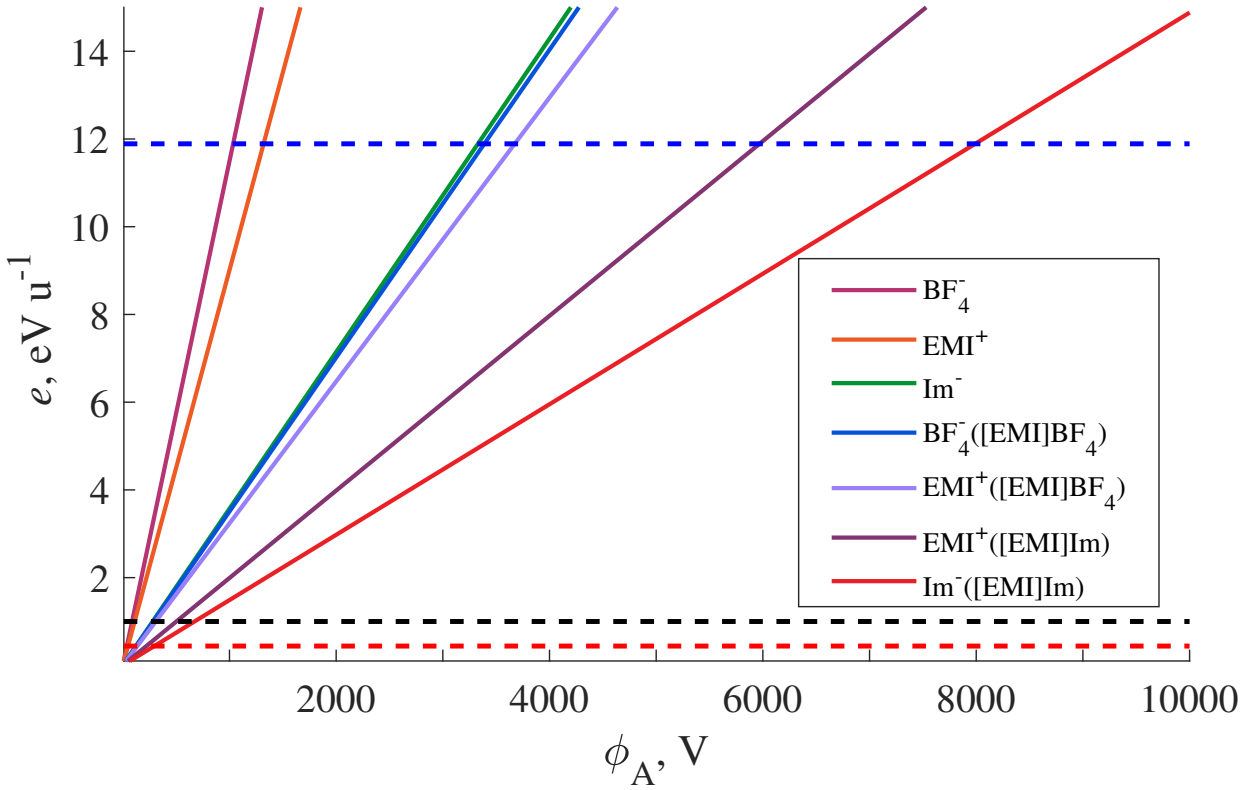

Figure 2.3: Specific energy thresholds for onset of secondary ion and electron emission by incident monomers and dimers of [EMI]Im and [EMI]BF_4. The red dashed line represents onset of electron emission ($0.44\,\mathrm{eV\,u^{-1}}$). The black dashed line represents onset of ion dissociation ($1\,\mathrm{eV\,u^{-1}}$). The blue dashed line represents the specific energy where predicted electron yield becomes unity, and begins increasing linearly ($11.89\,\mathrm{eV\,u^{-1}}$).

2.2 Droplet Impact Effects

As primary species mass increases, the slope of the specific energy line in Figure 2.3 decreases until clusters become large enough to fall below the thresholds for ion impact effects. At these regimes, impact behavior is better described by hydrodynamic phenomena. Hence the distinction between "ion" and "droplet" impact effects. The two droplet impact effects relevant to electrosprays are (1) shock-induced desorption, and (2) splashing.

2.2.1 Shock-Induced Desorption

Higher-order oligomer clusters and droplets have specific energies below the secondary ion emission threshold at accelerating potentials relevant to electrospray thrusters. While dissociation of incident ions is suppressed below the $1\ \mathrm{eV\,u^{-1}}$ threshold, SSE may occur in the form of desorption. Constituents released by desorption consist of secondary droplets born from the primary droplet, and vaporized fluid from the accumulated liquid on the surface. Desorbed species are either neutral, or retain the charge state of the incident primary droplet. The key difference between desorption and conventional splashing is that, with desorption, the moving shock causes a temperature jump in the droplet, inducing evaporation and allowing for higher mass loss than splashing alone. Desorption is distinct from sputtering or other ion impact processes in that the resulting mass spectra are effectively free of signals due to dissociated ions, which is an advantage of massive cluster impact mass spectrometry [100]. Mahoney et al. [101] proposed a shock wave model to explain the desorption of massive cluster impacts at low specific energies. When droplets impact a surface at velocities exceeding the acoustic speed of the liquid, a moving shock wave forms inside of the droplet, causing a large pressure and temperature spike. By applying the Rankine-Hugoniot equations to the impact interface, Mahoney et al. [101] were able to recover the heat of vaporization of the electrosprayed fluid within $\sim 12\%$ agreement of known values. High-speed imaging experiments performed by Field et al. [109] provide qualitative evidence that supports the notion of travelling shocks induced by high-velocity droplet impacts.

In terms of droplet size, the bounds of validity for shock theory are defined by the length-scale limits of continuum mechanics, and droplet diameters that impact at the acoustic speed. Mahoney et al. derive equations for minimum and maximum droplet diameters [101]:

$$D_{min} = \frac{1}{2}\tau c_0, \tag{2.4}$$

$$D_{max} = 2\left(\frac{6(\varepsilon_0\gamma)^{1/2}\phi_A}{\rho c_0^2}\right)^{2/3}, \tag{2.5}$$

where ε_0 is vacuum permittivity, γ is surface tension, ϕ_A is the accelerating potential, ρ is density, c_0 is the liquid's acoustic speed, and $\tau \approx 1\,\mathrm{ps}$ is the timescale of molecular vibrations.

The charge of droplets emitted by an electrospray lies between 0.5 and 1 of the Rayleigh stability limit, giving the following relationship for the bounds of droplet diameters [110, 111]:

$$(72\gamma\varepsilon_0/\rho^2\xi^2)^{1/3} < D < (288\gamma\varepsilon_0/\rho^2\xi^2)^{1/3}, \tag{2.6}$$

where ξ is the charge-to-mass ratio of the droplet. Tandem retarding potential and time-of-flight spectrometry published by Gamero-Castaño and Cisquella-Serra [58] give a range of ξ for [EMI]Im droplets between $142\,\mathrm{C\,kg^{-1}}$ and $1000\,\mathrm{C\,kg^{-1}}$.

To analyze the range of validity of shock theory in ionic liquid nanodroplets, we select $\phi_A = 6\,\mathrm{kV}$, corresponding to the nominal beam voltage used in the Colloid MicroNewton Thruster [31]. Substituting property values for [EMI]Im from Table B.1, into equations 2.4 and 2.5 gives minimum and maximum droplet diameters of 0.625 nm and 83.5 nm, respectively. Substituting the range of values for ξ into equation 2.6 gives an expected droplet diameter range of 21.4 nm to 125 nm. For the most part, we expect shock theory to be valid for describing the desorption process over most of the droplet diameters. However, some low-ξ droplets may be too large to induce a strong shock in the fluid upon impact. The threshold for onset of shock-induced desorption is the acoustic speed of the ionic liquid (i.e. $\sim 1250\,\mathrm{m\,s^{-1}}$ for [EMI]Im).

2.2.2 Splashing

Droplets travelling below the acoustic speed will not induce a travelling shock wave in the fluid, and the behavior is better described by splashing hydrodynamics. Three dimensionless numbers used to define the threshold for onset of splashing are the Reynolds, Weber, and Ohnesorge num-

bers. Reynolds number ($Re = \rho VD/\mu$) is the ratio of inertial to viscous forces. Weber number ($We = \rho v^2 D/\gamma$) gives the relative importance of a fluid's inertia to its surface tension. Ohnesorge number ($Oh = \mu/\sqrt{\rho\gamma D}$) relates viscous to inertial and surface tension forces. Splashing thresholds are reported as a power-law fit obeying the relationship $K_c = Oh \times Re^n$. The splashing threshold for macroscopic droplets impacting a dry surface has been experimentally and numerically determined at $K_{ds} = Oh \times Re^{1.25} \sim 50$ over a wide range of fluid parameters, with the exact parameter value varying with surface roughness [112, 113]. It remains uncertain whether macroscopic droplet impact trends are applicable to nanodroplets, since experimental observations of droplet impacts at the nanoscale are incredibly challenging. Nanodroplet behavior studies rely almost exclusively on theoretical frameworks or molecular dynamics (MD) simulations [114, 115, 116].

For nanodroplet impacts on dry surfaces, MD simulations by Li et al. [115] have determined the splashing threshold to be $K_{nd} = Oh \times Re^{0.5} = 3.25$, which agrees well with trends observed by Koplik and Zhang [116]. The discrepancy between macro- and nanodroplet splashing thresholds can possibly be attributed to the source of initial perturbations for instabilities that drive droplet breakup. Surface defects and trapped air pockets may serve as nucleation points for film instabilities that cause macroscopic droplet breakup [117]. By contrast, MD simulations often utilize ideal smooth surfaces as a target for incident nanodroplets [116, 115]. The initial disturbance that prompts nanodroplet breakup in MD simulations occurs when the amplitude of capillary waves on the droplet's surface becomes larger than the thickness of the spreading liquid film [115].

The vacuum environment in which electrospray thrusters operate challenges the applicability of well-established droplet splashing thresholds, which are mainly performed at atmospheric pressures. Experimental evidence shows that splashing due to droplet impacts on dry surfaces is suppressed in vacuum, which is attributed to the removal of trapped gas at the liquid-solid interface, thus suppressing breakup instabilities [118, 119]. However, molecular dynamics simulations indicate that this trend does not hold for nanodroplet impacts, and that the onset of splashing is not qualitatively affected by the removal of surrounding gas [116]. A further complication of vacuum operation is that the negligible vapor pressure of ionic liquids will lead to accumulation of propel-

lant on surfaces that intercept the plume. Any droplet impacts for electrospray thrusters operating in vacuum may occur on a thin liquid interface, rather than a clean solid. The splashing threshold for macroscopic droplets has been experimentally determined at $K_{tf} = Oh \times Re^{1.17} \sim 63$ for a thin film [120, 121], though the splashing threshold for nanodroplets on thin films remain unknown.

2.2.3 Onset Thresholds for Droplet Impact Effects

It's useful to put the power-law splashing thresholds into terms contextualized for electrospray propulsion systems. The charge-to-mass ratio (ξ) and accelerating potential (ϕ_A) are key performance metrics for evaluating thrust [30], and both have been experimentally resolved for [EMI]Im in a droplet-mode thruster [86, 58]. Therefore, we seek to express the thresholds for onset of droplet splashing in terms of ξ and ϕ_A. The diameter of a droplet charged to the Rayleigh limit is [21]:

$$D = 2\left(\frac{q_r}{8\pi\sqrt{\gamma\varepsilon_0}}\right)^{2/3} \tag{2.7}$$

By dimensional arguments, the charge-to-mass ratio of a droplet can be represented as

$$\xi = \frac{q_r}{m} = \frac{6q_r}{\rho\pi D^3}, \tag{2.8}$$

which may be rearranged to give q_r as a function of ξ:

$$q_r = \frac{\rho\pi D^3\xi}{6} \tag{2.9}$$

Equation 2.9 can be substituted into equation 2.7, giving an expression for droplet diameter as a function of charge-to-mass ratio:

$$D = \frac{1}{2}\left(\frac{48\sqrt{\gamma\varepsilon_0}}{\rho\xi}\right)^{2/3} \tag{2.10}$$

Conservation of energy gives $v^2 = 2\xi\phi_A$, which can be substituted along with equation 2.10 to

express Reynolds and Weber numbers as

$$Re = \frac{2\sqrt{2}(6\sqrt{\rho\gamma\varepsilon_0})^{2/3}}{\mu}\frac{\sqrt{\phi_A}}{\xi^{1/6}} \tag{2.11}$$

$$We = \left(\frac{48\sqrt{\rho\varepsilon_0}}{\gamma}\right)^{2/3}\xi^{1/3}\phi_A \tag{2.12}$$

Equation 2.12 can be rearranged to give an expression for ξ as a function of Weber number:

$$\xi = \frac{1}{\rho\varepsilon_0}\left(\frac{\gamma}{48}\right)^2\left(\frac{We}{\phi_A}\right)^3 \tag{2.13}$$

The power-law splashing thresholds may be recast by expressing *Oh* in terms of *Re* and *We*:

$$Oh \times Re^n = \sqrt{We}Re^{n-1} = K_c, \tag{2.14}$$

which may be rearranged to give *We* at the splashing threshold as a function of *Re*:

$$We = K_c^2 Re^{2(1-n)} \tag{2.15}$$

Equation 2.11 may be substituted into equation 2.15 to give *We* as a function of ξ and ϕ_A:

$$We = K_c^2\left(\frac{2\sqrt{2}(6\sqrt{\rho\gamma\varepsilon_0})^{2/3}}{\mu}\frac{\sqrt{\phi_A}}{\xi^{1/6}}\right)^{\frac{2}{(1-n)}} \tag{2.16}$$

Finally, we substitute equation 2.16 into equation 2.13 and move all ξ terms to the left hand side of the equation to arrive at an expression for evaluating the splashing thresholds in terms of

electrospray thruster performance parameters and propellant properties:

$$\xi = \left(\frac{1}{\rho \varepsilon_0} \left(\frac{\gamma}{48} \right)^2 \left(\frac{K_c^2}{\phi_A} \right)^3 \left(\frac{36(8\phi_A)^{3/2}(\rho\gamma\varepsilon_0)}{\mu^3} \right)^{\frac{2}{(1-n)}} \right)^{\frac{1}{(2-n)}} \tag{2.17}$$

Figure 2.4 shows equation 2.17 plotted for the dry surface ($K_{ds} = 50$, $n = 1.25$), thin film ($K_{tf} = 63$, $n = 1.17$), and nanodroplet ($K_{nd} = 3.25$, $n = 0.5$) limits. Droplet charge is assumed to lie between 0.5 and 1 times the Rayleigh limit [111], giving a locus of possible ξ for each splashing threshold. The acoustic speed ($c_0 = 1250\,\mathrm{m\,s^{-1}}$) is also shown to indicate the transition from splashing to shock-induced desorption.

To contextualize the splashing thresholds with electrospray thruster systems, we compare the expected splashing behavior of the droplet-mode thrusters operated at the University of California, Los Angeles (UCLA) and the Jet Propulsion Laboratory (JPL). A diagram of JPL's thruster setup is shown in Chapter 3.1 in Figure 3.1, and an overview of UCLA's electrospray system has been presented by Collins et al [122]. The UCLA and JPL electrospray systems operate with identical emitter and extractor geometries, and emitter-to-extraction voltages of $\sim 1.6\,\mathrm{kV}$. A key difference is that UCLA grounds the extractor while JPL operates with a $\sim 6\,\mathrm{kV}$ total bias from emitter-to-ground to better approximate the Colloid MicroNewton Thruster (CMNT) bias levels [31]. Subsequently, both setups have similar ξ profiles, yet different net acceleration potentials ($\phi_{A1} \approx 1.2\,\mathrm{kV}$ and $\phi_{A2} \approx 5.6\,\mathrm{kV}$, per equation 2.2). The marked bounds of ξ values expected in UCLA and JPL's respective droplet-mode electrospray systems are estimated to lie between $142\,\mathrm{C\,kg^{-1}}$ and $1000\,\mathrm{C\,kg^{-1}}$ [58].

The trends shown in Figure 2.4 suggest that splashing is inevitable in droplet-mode electrospray thrusters. JPL's thruster configuration operates in a regime where the entire droplet population undergoes shock-induced desorption. UCLA's thruster configuration operates in a regime where splashing is expected, and some of the higher-ξ droplets cross the desorption threshold. Observing the upper left hand corner of Figure 2.4, the UCLA thruster operates near a regime where

the desorption threshold intersects with the two macroscopic droplet splashing thresholds. The behavior at the intersecting region is unknown, but the desorption threshold is likely more accurate in this region, since the empirical splashing thresholds were established for macroscopic droplets in operating conditions that may not be valid for electrosprayed nanodroplets.

Demmons et al. [123] have reported observing backstreaming progeny droplets during thruster characterization studies performed at Busek using a thruster configuration similar to JPL's electrospray setup. Lenguito et al. [124] reported observing mass accumulation on downstream-facing elements due to an unknown "flyback mechanism," which was likely due to splashing. Mass deposition and reflection due to splashing and desorption are important to quantify, since mass accumulation on the grids determines lifetime for droplet-mode thrusters. Reflection of mass off downstream surfaces introduces uncertainty on plume diagnostics used to measure mass accumulation rate, such as quartz-crystal microbalances (QCMs). Droplets that return to the thruster and impinge on downstream-facing thruster components artificially increase the accumulation rate of mass to the grids, causing premature thruster end-of-life.

The charge state of splashed or desorbed droplets may be qualitatively evaluated by comparing the charge relaxation time ($t_r = \varepsilon\varepsilon_0/\kappa$) to the inertial timescale for a droplet splash,

$$\tau_i = D/\sqrt{2\xi\,\phi_A}, \tag{2.18}$$

where D is the droplet diameter. When $\tau_i/t_r >> 1$, the droplet's charge may equilibrate with the surface throughout the splashing process, resulting in low-ξ or charge-neutral progeny droplets. To evaluate τ_i, the minimum and maximum expected ξ values ($\xi = 142\,\mathrm{C\,kg^{-1}}$ to $1000\,\mathrm{C\,kg^{-1}}$) are substituted into equation 2.10 and equation 2.18. Figure 2.5 indicates that for acceleration potentials greater than $\sim 100\,\mathrm{V}$, even the largest expected droplets will produce charged progeny through the splashing or desorption processes.

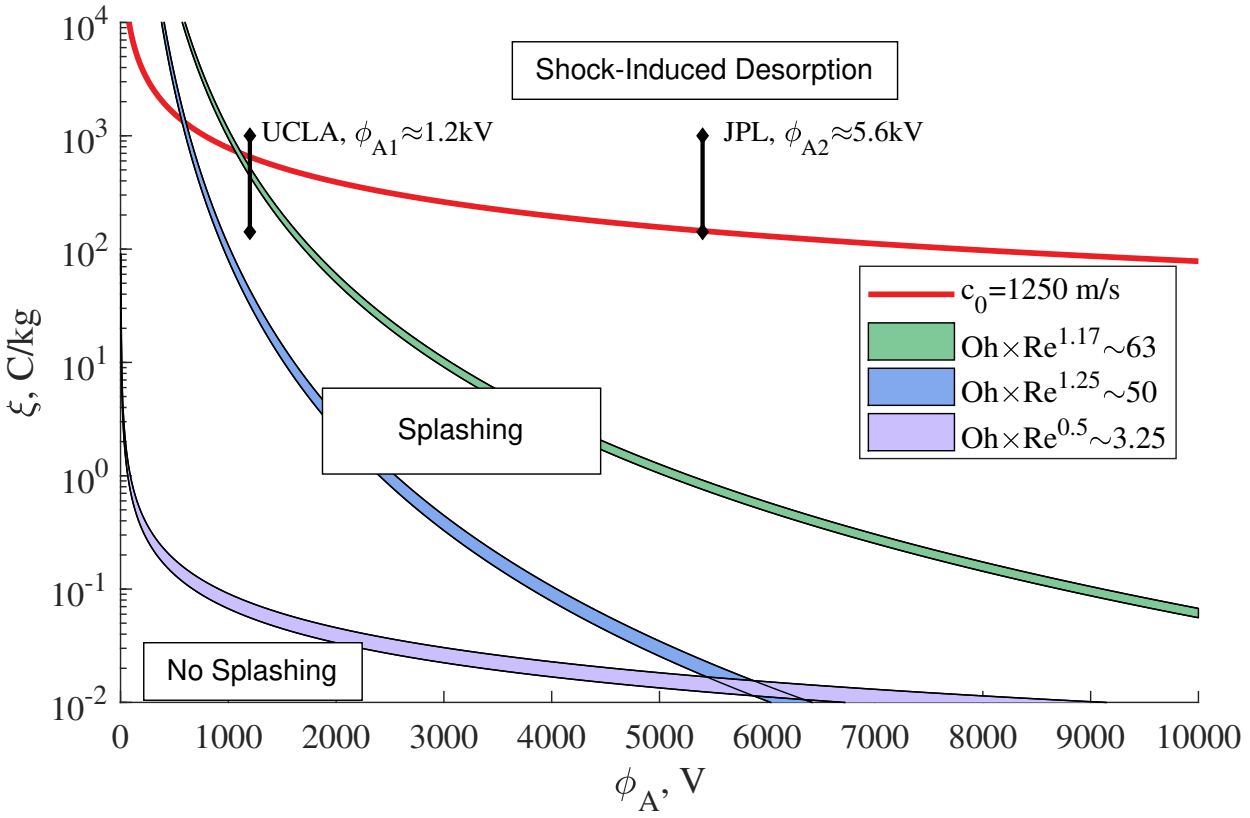

Figure 2.4: Charge-to-mass ratio thresholds for splashing and shock-induced desorption as a function of accelerating potential. The patches represent upper and lower bounds on ξ estimated by 0.5 to 1 times the Rayleigh charge limit for a droplet. Three different empirical splashing thresholds are shown. The purple patch represents the nanodroplet splashing threshold ($K_{nd} = 3.25$, $n = 0.5$). The green patch represents the thin film splashing threshold ($K_{tf} = 63$, $n = 1.17$). The blue patch represents the dry surface splashing threshold ($K_{ds} = 50$, $n = 1.25$). The red line represents the acoustic limit for [EMI]Im, above which Shock-Induced Desorption should occur. The vertical black lines indicate the range of expected ξ for droplets emitted by the UCLA and JPL electrospray thrusters at the estimated ϕ_A for each system.

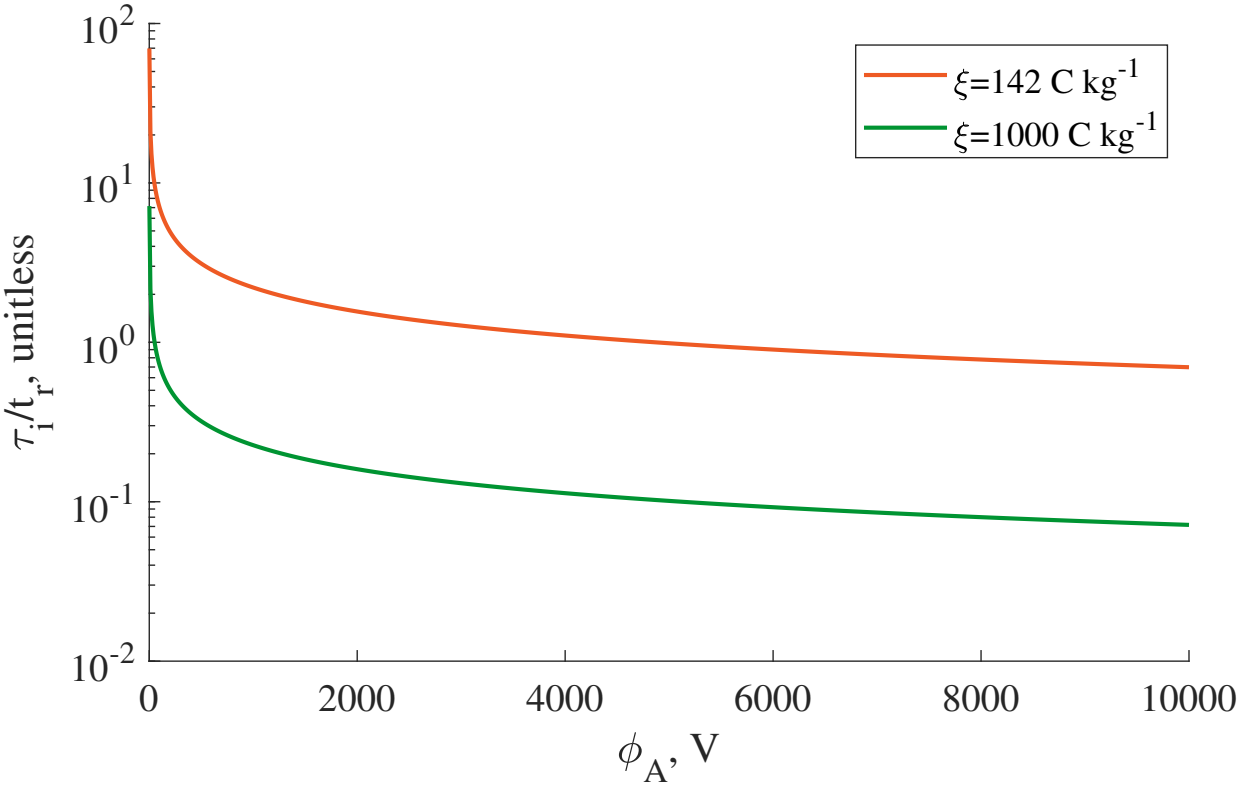

Figure 2.5: Inertial timescale of droplet splashing ($\tau_i = D_{max}/\sqrt{2\xi\phi_A}$) normalized to charge relaxation time ($t_r = \varepsilon\varepsilon_0/\kappa$). When $\tau_i/t_r >> 1$, the droplet's charge may equilibrate with the surface throughout the splashing process, resulting in low-ξ or charge-neutral progeny droplets. For reasonable accelerating potentials, we can expect a high likelihood of charged progeny droplets.

2.3 SSE Summary

Chapter 2 provided a broad overview of the complex mechanisms through which the primary species in an electrospray thruster's plume produce secondary species upon impact with a surface. The presented analyses of SSE thresholds has shown that charged secondary species are likely always present when operating electrospray thrusters in vacuum chambers, and must therefore be taken into consideration when designing and operating electrospray ground testing facilities, or evaluating the data obtained by intrusive plume diagnostics. The discussed SSE mechanisms have been presented as distinct and separate phenomena, but it is possible for concurrent production of different secondary species. For example, an ion may undergo collision-induced dissociation upon impact with a metallic surface, and also impart enough kinetic energy to liberate a secondary electron from the surface. Another possible post-emission process is the evaporation of ions from charged progeny droplets recoiling from a splashing event. Post-emission interactions may occur between the emitted secondaries that are currently unknown.

CHAPTER 3

Influence of SSE on Facility Effects and Electrospray Thruster Operation

The effects of secondary electrons have been alluded to in prior electrospray thruster studies [38, 125, 126, 127, 128, 129], and briefly hypothesized as a possible life-limiting mechanism for electrosprays [45, 126]. *In situ* electron microscopy by Terhune et al. [126] revealed that ILIS emission sites will form dendritic solid structure under electron bombardment. Modelling work by Magnusson et al. [87] and experimental work by Klosterman et al. [130] have characterized IIEE yields in conditions relevant to ILIS thruster operation. Electron backstreaming has been considered as a life-limiting mechanism by Thuppul et al. [51] in the context of space plasma electrons. However, the secondary emission of heavier, positively-charged species in electrospray devices has been largely ignored in literature, and must be considered when operating electrospray thrusters in vacuum facilities. Furthermore, analyses of the consequences that SSE may have on electrospray thruster performance and lifetime are missing from the available literature.

Since properly designed ILIS thrusters operate in the "pure ion emission" regime, splashing and desorption may be neglected. In droplet-mode thrusters, the polydisperse plume consists of both ions and droplets, so all forms of secondary ejecta must be considered. Secondary species interact with electrospray thrusters via "backstreaming", where species return to the thruster and impinge upon critical components. Backstreaming secondaries are attracted to surfaces that are biased opposite of their charge state. The objective of Chapter 3 is to present experiments and models that demonstrate several possible consequences of SSE on electrospray thrusters.

The experimental data in Chapter 3.1 demonstrates how SSE generated at facility surfaces in-

troduces considerable uncertainty to lifetime measurements. The angular current density distributions in Chapter 3.2 illustrates how secondary currents lead to uncertainty in plume measurements. Post-testing microscopy shown in Chapter 3.3 provides insight into the processes undergone when high-velocity primary species impact surfaces, revealing evidence of SSE phenomena discussed in Chapter 2. The heat and mass flux analysis in Chapter 3.4 examines the contribution of SSE-induced Ohmic dissipation to performance and lifetime limitations in ILIS thrusters. Chapter 3.5 presents arguments that SSE is the root cause of glow discharge phenomena observed in electrospray thrusters, and experimental optical emission spectra as evidence supporting the claim.

3.1 SSE-Induced Thruster-to-Facility Coupling

.

To meet the >40,000 hour lifetime requirements for the LISA or HabEx missions, UCLA and NASA JPL are jointly developing high-fidelity models of Busek's Colloid Microthruster Technology, and validating them experimentally [49, 52, 55, 131, 122]. Model validation requires precise current measurements from the emitter, extractor, and accelerator electrodes. Currents measured at the accelerator and extractor quantify the extent of plume impingement, which is the main life-limiting mechanism in droplet-mode electrospray thrusters [51]. Thruster end-of-life occurs when the porous accelerator or extractor electrodes become saturated with propellant, and either short-circuit or spray back towards upstream electrodes. Hence, plume impingement current from the extractor and accelerator are key metrics for evaluating thruster lifetime. Secondary species that backstream from the beam target towards the thruster may also strike the downstream-facing sides of the accelerator and extractor, conflating measurements of the plume impingement current with secondary species currents. JPL and UCLA both corroborate Busek's experimental observations of propellant accumulation on downstream-facing thruster components [123], which has prompted the development of an approach to effectively mitigate SSE at the beam target.

Secondary electron emission is often suppressed by either biasing the collection surface it-

self [38, 125], or biasing an intermediate grid [132]. Due to the presence of both cationic and anionic secondary species, practices generally employed in the EP community are not sufficient to suppress SSE in electrosprays. Since the testing apparatus is designed for long-duration lifetime experiments, intermediate suppression grids are unfeasible, as they may accumulate propellant and clog. Furthermore, the grids themselves emit secondary species when impinged upon by the plume, so SSE is not adequately mitigated. A novel approach was devised that employs a biased beam target, along with a separately biased "electron cage" electrode that partially frames the beam target without intercepting the plume. The trade-off with an open electron cage geometry is that the potential within the beam target geometry is inhomogeneous. The objective of the beam target biasing experiment was to identify possible facility operating regimes where SSE is mitigated, permitting lifetime tests that exclude the uncertainty introduced by SSE.

3.1.1 Beam Target Bias Experiment

Figure 3.1 shows a diagram representing the electrode configuration and nomenclature used in the beam target biasing experiment. Each electrode is monitored with a picoammeter, and the beam target is the only electrode whose bias is varied. The electron cage bias is held at $\phi_{ec} = 100\,\text{V}$, and the beam target is swept from $\phi_{bt} = -100\,\text{V}$ to $100\,\text{V}$. Presented current traces for the extractor (I_{ext}), accelerator (I_{acc}), shield (I_{sh}), electron cage (I_{ec}), and beam target (I_{bt}) are all normalized by the emitter current (I_{em}). The beam target has an area of approximately $0.15\,\text{m}$ by $0.15\,\text{m}$, and located $\sim 0.1\,\text{m}$ downstream of the thruster.

Figure 3.2 shows the current-voltage (I-V) characteristic traces for the ϕ_{bt} sweep, and Figure 3.3 shows the total I-V trace representing the sum of all measured currents shown in Figure 3.2. Ideally, the total I-V trace should be zero, yet aggregate current varies by $\pm 25\%$ over the ϕ_{bt} range, indicating that charge is lost to the vacuum chamber. A key observation from the presented I-V traces is that the total sweep range of the beam target bias is very small when compared to the emitter bias voltage voltage ($\pm 1.6\%$), yet impingement currents I_{ext} and I_{acc} experience substantial nonlinear and asymmetric variation in response. The system's I-V curve behavior indicates

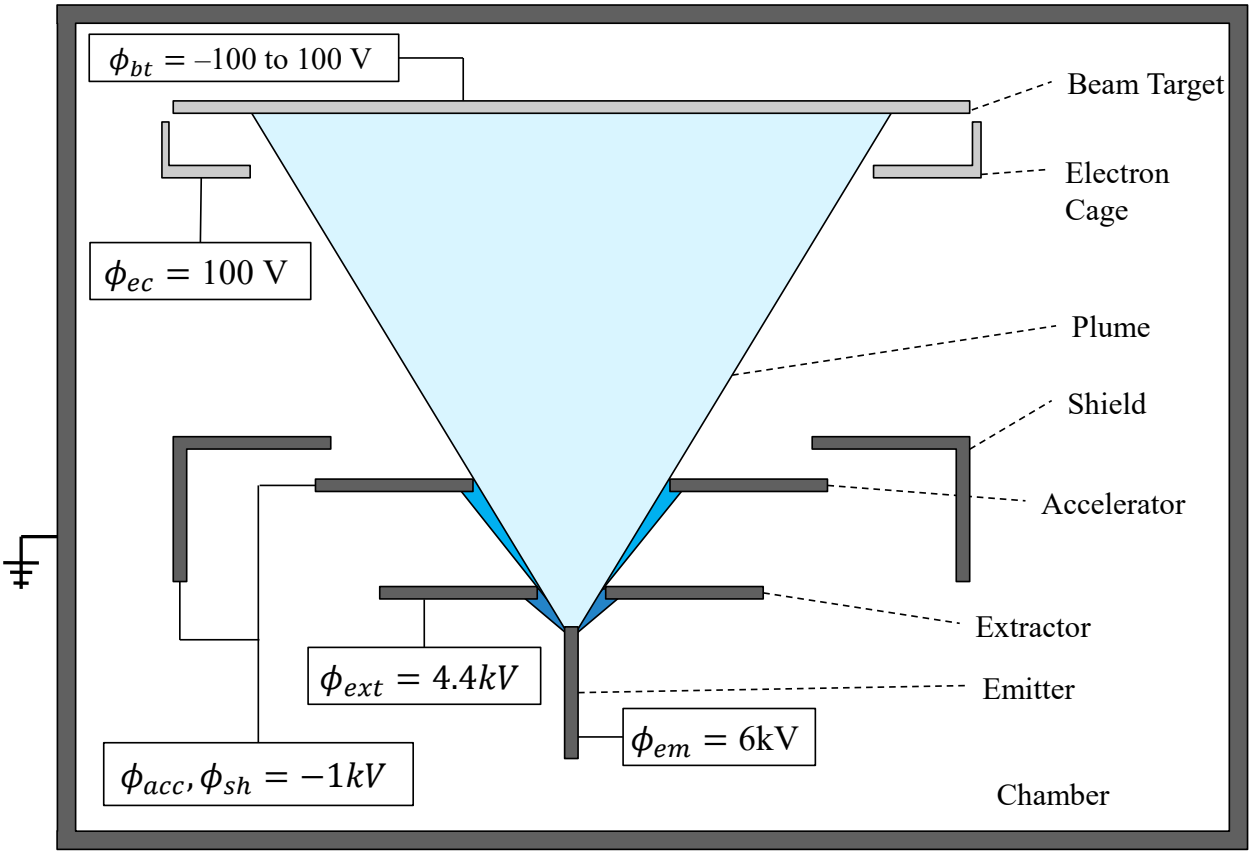

Figure 3.1: Schematic representing the thruster testing setup for JPL's electrospray thruster.

current coupling between the thruster and facility that we hypothesize is attributed to emission and transport of secondary species. While the maximum impingement current deviation is only ∼5% of the total emitter current, measured current due to overspray is indistinguishable from current due to backstreaming cations. Interpreting impingement current as exclusively due to primary incident droplets, we can apply a scaling analysis to the thruster end-of-life calculation used by Thuppul et al. [51]:

$$t_{sat} = \frac{\rho \forbar{V}_{crit} \langle \xi \rangle}{I_{imp}}, \tag{3.1}$$

where $\forbar{V}_{crit}$ is the critical accumulated propellant at which an electrode becomes saturated, $\langle \xi \rangle$ is mean charge-to-mass ratio of incident droplets, and I_{imp} is the impingement current. We take the parameters' orders of magnitude to be $\rho = O(10^3)$, $\forbar{V}_{crit} = O(10^{-7})$, $\langle \xi \rangle = O(10^2)$, and $I_{imp} = O(10^{-9})$, giving $t_{sat} = O(10^7)$. An increase in normalized I_{acc} from 0.004 to 0.01 is ef-

fectively a 2.5 times increase in current, which causes t_{sat} to drop by 60%. Understanding the observed thruster-facility coupling is vital to quantifying the uncertainty it introduces to experimental measurements to provide accurate model validation data.

3.1.2 Total Facility Current Response

Based on observations of the experimental data, electric field simulations, and qualitative arguments of charged species behavior, we postulate that the total I-V trace in Figure 3.3 can be broken into three different regimes: (1) Anionic Enhancement, (2) Secondary Mitigation, and (3) Cationic Enhancement.

The Anionic Enhancement regime occurs when $\phi_{bt} < \sim 0\,\text{V}$, where the beam target repels negative species and attracts positive species. In Anionic Enhancement, the extractor current, I_{ext} experiences increasing current as ϕ_{bt} is biased more negatively. The accelerator's ϕ_{acc}=$-1\,\text{kV}$ bias should repel negative secondary species, preventing backstreaming to the extractor and emitter. However, axisymmetric COMSOL simulations of the CMNT geometry show that the maximum potential at the accelerator's aperture is $\sim -200\,\text{V}$ [51]. High-energy negative species in the tail of their velocity distribution function may receive enough energy enhancement from ϕ_{bt} to overcome the potential at the accelerator's aperture, yet not enough energy to strike the accelerator itself. After bypassing the accelerator, negative species will be attracted to the positive bias of the extractor and emitter, resulting in the elevated extractor current seen in Figure 3.2. Space charge due to the primary plume may further increase the potential on-axis, giving the electrons a path to travel up through the accelerator.

When $0\,\text{V} < \phi_{bt} < \sim 50\,\text{V}$, secondary species backstreaming to the thruster are effectively mitigated. Some negative species may still have enough energy to overcome ϕ_{ec}, but not enough to overcome ϕ_{acc}. While positive species have greater energy enhancement, they still do not have enough energy to overcome ϕ_{ec}. Electron cage current, I_{ec} is maximized in the Secondary Mitigation regime, indicating that ϕ_{bt} slows negative species enough for the electron cage to capture

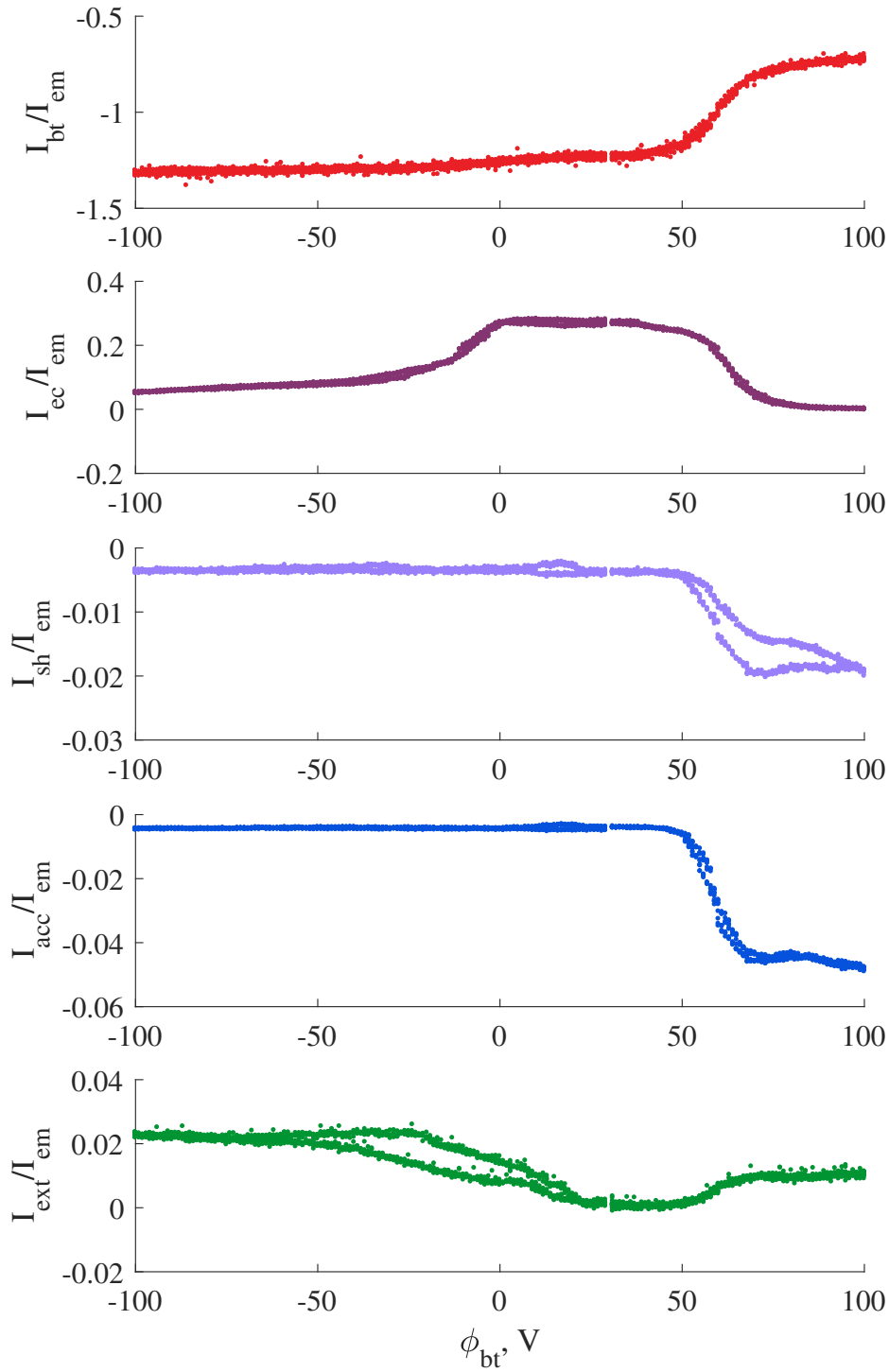

Figure 3.2: Current from the beam target (I_{bt}), electron cage (I_{ec}), shield (I_{sh}), accelerator (I_{acc}), and extractor (I_{ext}). All values are normalized by the measured emitter current (I_{em}).

secondary species. Operating in Secondary Mitigation is preferred for lifetime testing and model validation of the CMNT, since any measured current should be solely due to impingement from the plume.

The Cationic Enhancement regime occurs when $\phi_{bt} > \sim 50\,\mathrm{V}$, where negative species are heavily suppressed and positive species now receive enough energy enhancement to overcome ϕ_{ec}. Since ϕ_{acc} is negative, it strongly attracts the backstreaming positive species, causing the negative currents observed on the shield and accelerator (I_{sh} and I_{acc}, respectively). The positive current seen on the extractor grid in the Cationic Enhancement regime may be explained by a complex sequence of events. A fraction of the positive secondaries may be drawn into the accelerator aperture, whereupon encountering the positive extractor bias ($\phi_{ext} = 4.4\,\mathrm{kV}$), the cations are then repelled into the upstream-facing side of the accelerator. Since the accelerator is biased to a rather high potential, the cations themselves are accelerated to primary energies, resulting in secondary anion or electron emission. The extractor will readily collect negative species, resulting in an observed positive current.

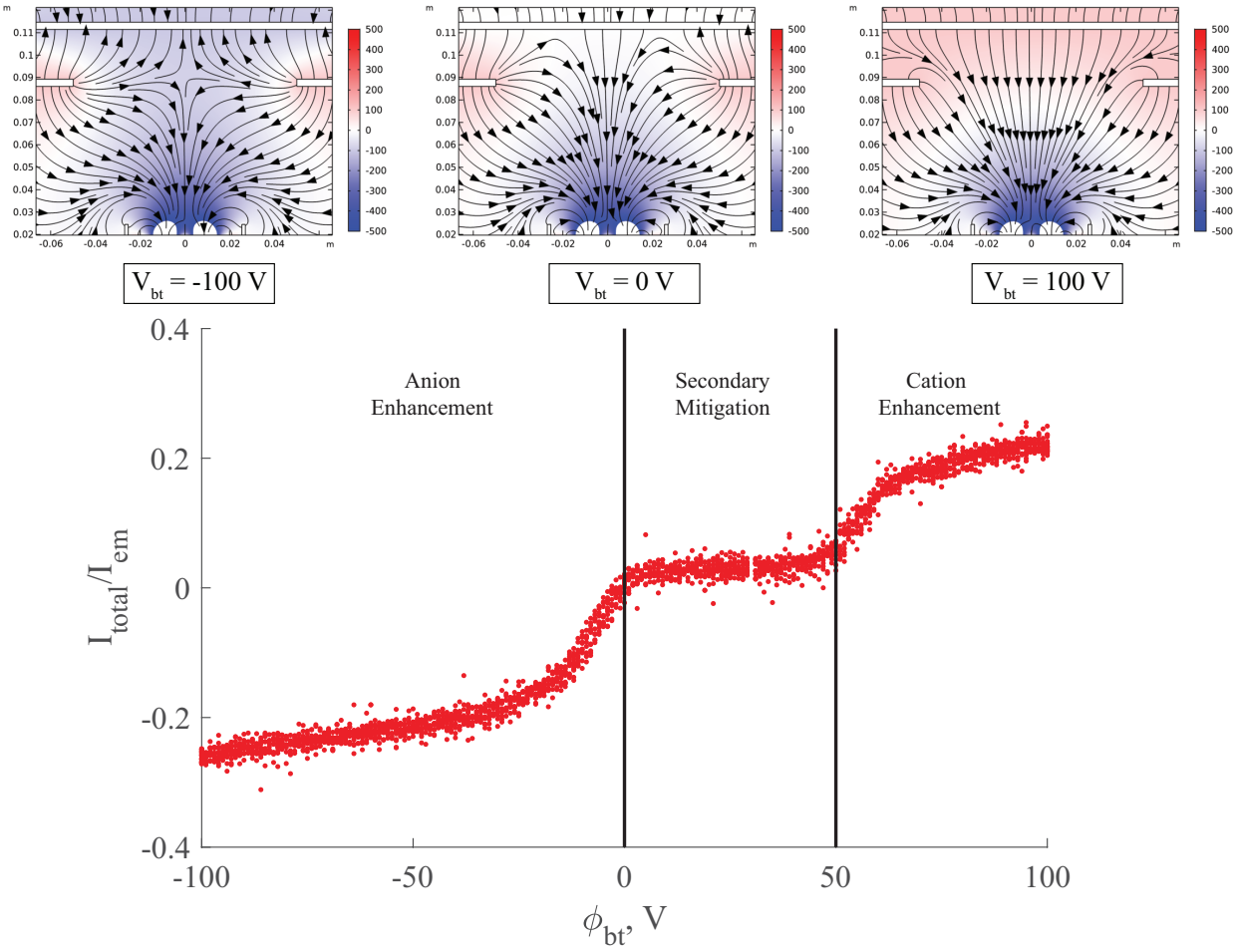

Figure 3.3: The top images show streamlines of the electric field in the region downstream of the thruster, with the overlaid surface map representing potential. The electric field lines are normalized to illustrate trends as the target's bias is varied. The bottom trace shows the sum of the normalized electrode currents plotted against beam target bias potential, indicating loss of charged species to the vacuum chamber in the labeled SSE regimes.

3.2 SSE-Induced Measurement Uncertainty

The beam of an electrospray device is inherently polydisperse due to several natural processes, including deviations in droplet diameter during jet breakup, coulombic explosions downstream of the emission site, and evaporation of ions from droplets within the beam [58, 111]. The distribution of charge-to-mass ratios in the beam also affects the terminal velocities of beam constituents – a fact that enables time-of-flight mass spectrometry techniques commonly employed to analyze polydispersity in electrosprays [58, 133, 4]. Polydispersity affects the beam structure, which manifests as spatial variation of charge-to-mass ratio and velocity distributions over the angular extent of the beam. Since SSE processes are sensitive to both charge-to-mass ratio and incident velocity of the primary species, SSE behavior should also exhibit spatial dependence. A novel "SSE Probe" and analysis technique was developed to quantify the spatial dependence of SSE behavior, and determine the impact that SSE may have on plume diagnostics.

3.2.1 Selective Secondary Species Suppression

Evaluating SSE contributions to measured currents relies on the observed bipolar sensitivity to applied voltages, and the large energy discrepancy between incident primary species ($> 1\,\mathrm{keV}$) and emitted secondary species ($< 5\,\mathrm{eV}$). Voltages applied to the collector will attract any opposite-charged secondaries back to the collection surface, while repelling same-charge secondaries. Selective suppression analysis requires three measurements to distinguish SSE current contributions to the total measured current: a null bias measurement, a positive SSE saturation measurement, and a negative SSE saturation measurement. Figure 3.4 shows an illustration of selective secondary species suppression described above.

When a null voltage bias is applied to the collector ($\phi_c = 0\,\mathrm{V}$), the measured current is

$$I_{meas}\Big|_{\phi_c=0\,\mathrm{V}} = I^P - I^S_+ + I^S_-, \tag{3.2}$$

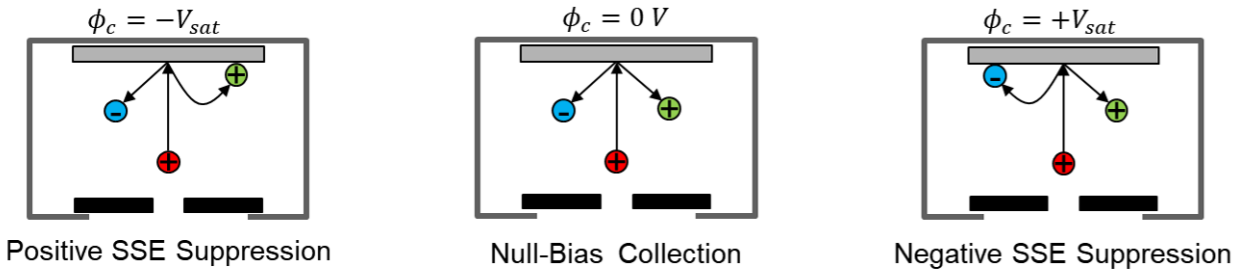

Figure 3.4: Selective secondary species suppression due to different applied potentials to a collection surface. Left: Positive SSE Suppression, Middle: Null-Bias Collection, Right: Negative SSE Suppression.

where I^P is the collected primary species, I^S_+ is the emitted positive secondary species, and I^S_- is the emitted negative secondary species. With a sufficiently positive collector bias ($\phi_c = +V_{sat}$), all emitted negative species will be suppressed and the probe will reach a positive saturation current,

$$I_{meas}\Big|_{\phi_c=+V_{sat}} = I^P - I^S_+ \tag{3.3}$$

Likewise, with a sufficiently negative collector bias ($\phi_c = -V_{sat}$), all emitted positive species will be suppressed and the probe will reach a negative saturation current,

$$I_{meas}\Big|_{\phi_c=-V_{sat}} = I^P + I^S_- \tag{3.4}$$

Subtracting equation 3.3 from equation 3.2, and equation 3.4 from equation 3.2 gives the negative and positive secondary currents as a function of measured current values:

$$\begin{aligned} I^S_- &= I_{meas}\Big|_{\phi_c=0\,\mathrm{V}} - I_{meas}\Big|_{\phi_c=+V_{sat}} \\ I^S_+ &= I_{meas}\Big|_{\phi_c=-V_{sat}} - I_{meas}\Big|_{\phi_c=0\,\mathrm{V}}. \end{aligned} \tag{3.5}$$

The equations 3.5 may be substituted into equation 3.2 to give the actual collected primary

current:

$$I^P = -I_{meas}\Big|_{\phi_c=0\,\mathrm{V}} + I_{meas}\Big|_{\phi_c=-V_{sat}} + I_{meas}\Big|_{\phi_c=+V_{sat}} \tag{3.6}$$

Secondary species have very low temperatures ($< 5\,\mathrm{eV}$), so $V_{sat} = 100\,\mathrm{V}$ is used to ensure adequate secondary suppression. Since $V_{sat} << V_{beam}$, the probe bias will not affect collection of primary species. The presented analysis is simple, yet powerful in that it mitigates current measurement uncertainties due to SSE for any biased collector electrode in an electrospray device. The following section will detail the design considerations for an "SSE Probe" whose objective is to provide precise measurements of primary and secondary currents.

3.2.2 SSE Probe Design

The SSE Probe was developed as a purpose-built diagnostic leveraging the analysis detailed in Section 3.2.1 to obtain the true current densities throughout an ionic liquid electrospray beam, as well as the spatial distribution of positive and negative SSE yields. Discussion on SSE yields will be withheld until Chapter 4.3 for the sake of context. This section will discuss the two major considerations for measurement uncertainty, and provide rationalization of probe design choices that contributed to the final embodiment of the SSE Probe. The first contributor to measurement uncertainty is collection of secondaries produced from surfaces other than the collector, which results in an enhancement in the perceived SSE yield. The second contributor to uncertainty is excessive leakage current in transmission lines, which results from finite conductivity in insulators and varies with applied bias potential. For simplicity, the presented probe design is based on a cylindrical tube geometry.

Coulombic interactions within an electrospray beam only dominate immediately downstream of the jet breakup region, so space charge contributions downstream of this "interaction region" are negligible [134, 55, 135, 136]. The presence of a single charge polarity within the beam ostensibly simplifies the analysis of current probes compared to plasma diagnostics, since considerations for

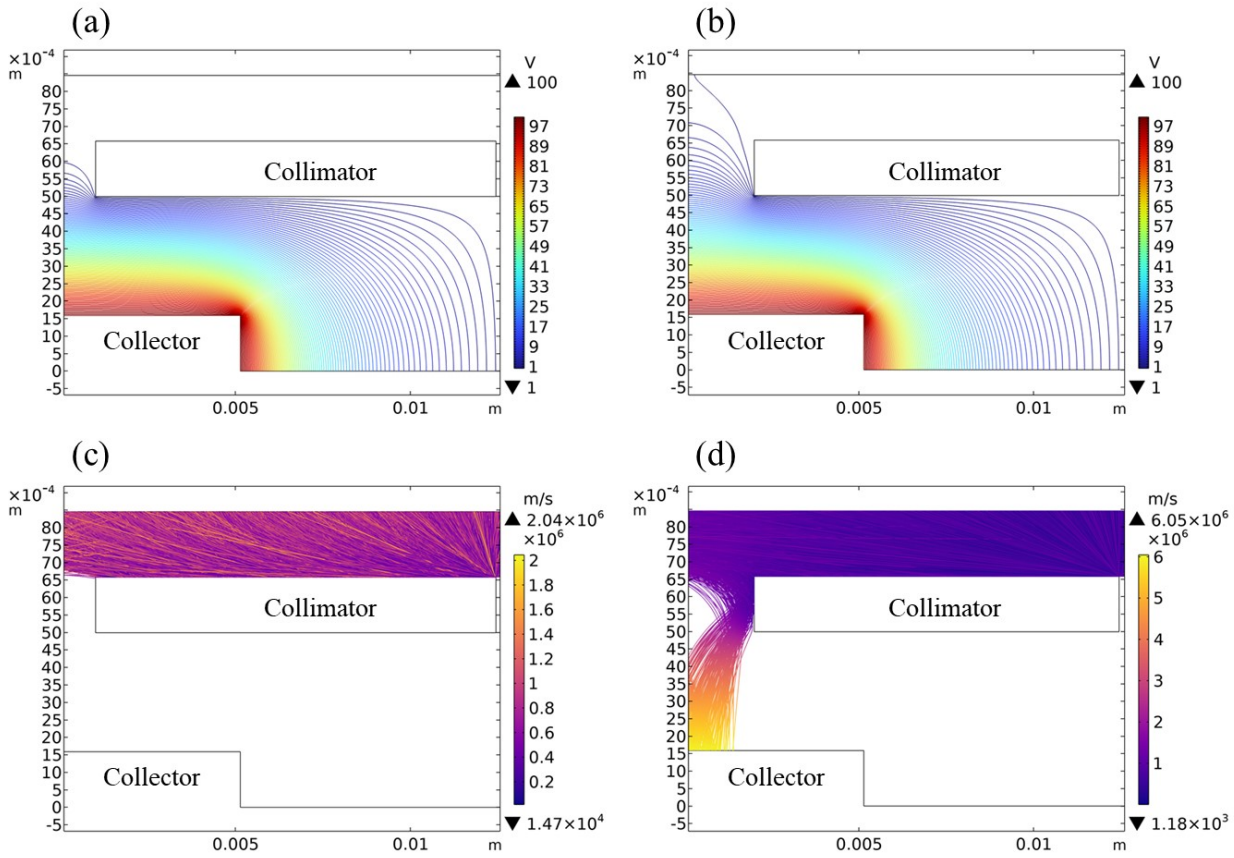

Figure 3.5: Results of a 2-D axisymmetric COMSOL study. The potential contours and particle trajectories are of two representative SSE Probe configurations, with aspect ratios $AR = 0.75$ and $AR = 0.375$. Simulated SSE are $T = 1\,\text{eV}$ electrons, since they will be the most mobile species. Plots (a) and (b) show increased penetration of the collector's electrostatic field with increased collimator aperture diameter. Plots (c) and (d) show influx of SSE from the upstream face of the collimator.

sheaths may be neglected. However, with the presence of secondary species emitted from any surface intercepted by the beam, the lack of a bulk plasma to "shield" the collector from non-localized phenomena introduces a considerable element of uncertainty in diagnostics that rely on current measurement. Since secondary species are generally emitted with very low temperatures, their trajectories are easily deflected by relatively low potentials. An excellent analogy to plasma diagnostics would be the behavior described by orbital-motion-limited ion collection theory, where the sheath is considered infinitely-thick, and therefore a biased collector will deflect the motion of charged species from everywhere within the chamber [137, 138]. As a consequence of the described orbital-motion-limited current collection behavior of secondary species, careful design considerations must be made to ensure that secondaries generated elsewhere do not contribute to current measured by the collector.

In electrostatic diagnostics, such as retarding potential analyzers, metallic grids are used to form a semi-transparent equipotential surface [139, 140, 141]. However, ionic liquids have negligible vapor pressure, so intercepted propellant will accumulate on the grids and ultimately block the beam. Furthermore, secondaries emitted from the grids themselves may contribute to measurement uncertainty if they enter the probe. Instead of a grid, the SSE Probe uses a single collimating aperture as seen in Faraday cup designs [142]. The collimating aperture is connected to ground, shielding the collector bias from attracting secondaries emitted elsewhere in the chamber. The collimators's effectiveness as a shield is related to its aperture aspect ratio, which is defined as the aperture channel's length divided by its diameter ($AR = L_{ch}/D_{ch}$).

Channel length and diameter may both be tuned to reach an ideal aspect ratio, but increasing length causes greater beam impingement upon the channel walls, generating unwanted SSE. For the presented design, aperture channel length is fixed at $L_{ch} = 1.5\,\text{mm}$, and a parametric sweep of the channel diameter was conducted using COMSOL's Electrostatics and Particle Tracking modules to evaluate an ideal diameter. Figure 3.5 shows two representative sets of results from a 2-D axisymmetric COMSOL study, where plots (a) and (b) illustrate how the equipotential contours change with aspect ratio. The collimator face is the nearest beam-facing surface to the collec-

tor, so it will serve as the greatest contributor to unwanted secondaries that may be attracted to the collector bias, introducing measurement uncertainty. Emission of undesired secondary species was simulated on the collimator face by releasing 100,000 electrons from the surface with a temperature of 1 eV. Plots (c) and (d) in Figure 3.5 clearly show the consequence of too wide an aperture diameter. The parametric sweep suggests that when $AR > 0.5$, the collimator provides adequate shielding of the collector bias voltage, minimizing the amount of externally emitted secondaries from being drawn into the probe. A channel diameter of $D_{ch} = 2\,\text{mm}$ (i.e. $AR = 0.75$) was chosen for the presented SSE Probe design. Spherical expansion of the beam is negligible in the short distance between collimating aperture and collector electrode, so the aperture area is the used for calculating current density. Since some degree of impingement on the channel walls is unavoidable, graphite was selected as the collimator material due to its low sputtering and electron emission yields [143]. Other refracotry metals (e.g. molybdenum and tungsten) would make excellent candidates, as well. One possible design consideration is "knife-edging" the chamfering of the downstream corner of the aperture to reduce the effects of SSE from the aperture wall. However, such chamfering will reduce the aperture size (and hence signal to the collector) needed to effectively suppress collection of SSE from the upstream face of the aperture plate.

With a collimator aperture diameter selected, it's important to estimate the expected current levels, since electrospray beam current densities are very small. Using the mass flux and current density measurements of the CMNT beam obtained by Thuppul et al [144], we can estimate the measured current signal. Peak current density is approximately $8\,\text{nA/cm}^2$, so a 2 mm diameter collection area will give 250 pA of signal on centerline, and as low as $\sim$1 pA at high beam angles. When measuring picoampere levels of current with an applied bias, the second critical design consideration is whether leakage currents will introduce significant measurement error.

Leakage current manifests due to finite insulation resistance in cabling that connects the current sensor to the probe. When biasing the center conductor of a coaxial cable, the insulation resistance will always allow a small amount of current to pass to ground, with leakage current proportional to the bias voltage divided by the insulation resistance, $I_{leak} = V_{bias}/R_{ins}$. For a coaxial cable,

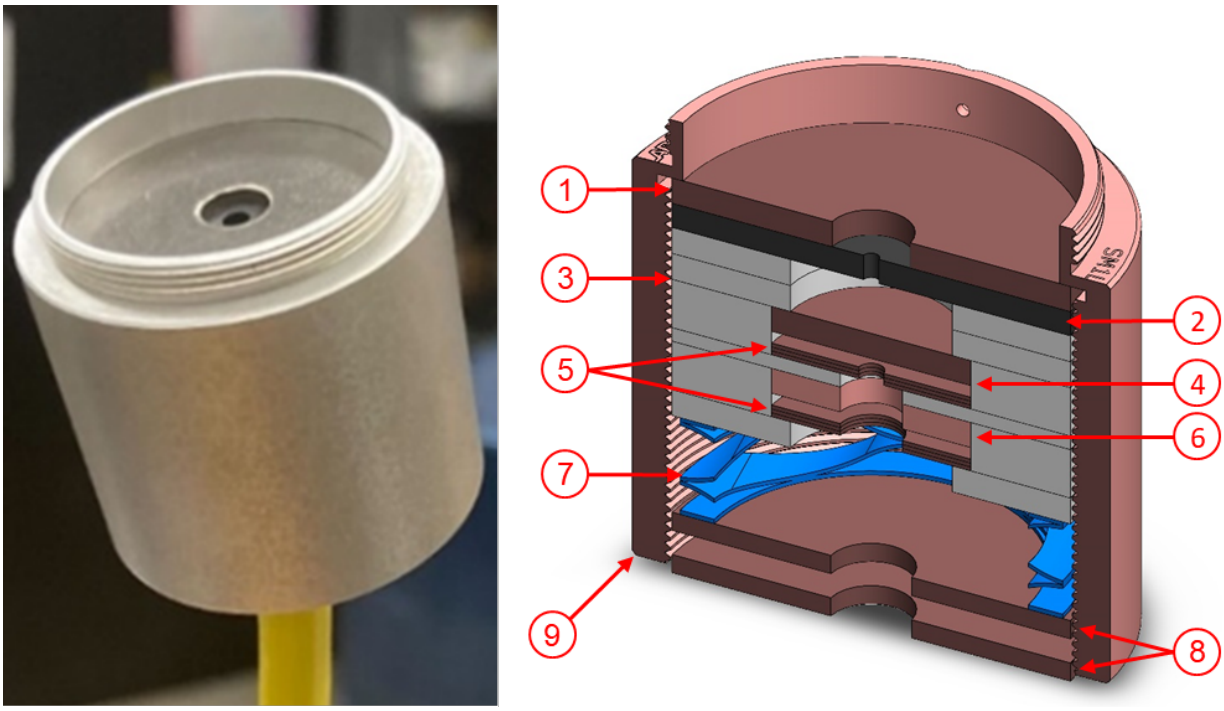

Figure 3.6: Left: SSE Probe assembly with triaxial cable installed. Right: Cross-section image of the SSE Probe, including numbered callout descriptions: (1) grounded probe cover, (2) graphite collimator, (3) polytetrafluoroethylene insulator, (4) collector electrode, (5) connector retaining rings, (6) guard electrode, (7) stacked wave disc spring, (8) shield electrode, and (9) probe body. Coloring distinguishes different key components, where copper corresponds to conductors, gray to insulators, black to the graphite collimator, and blue to the spring.

insulation resistance is estimated as

$$R_{ins} = \frac{\rho L}{A}, \tag{3.7}$$

where ρ is the resistivity, L is cable length, and A is insulator cross sectional area. An infinitesimal slice of insulator in the radial direction is

$$dR_{ins} = \frac{\rho dr}{2\pi r L}. \tag{3.8}$$

Integrating equation 3.8 gives

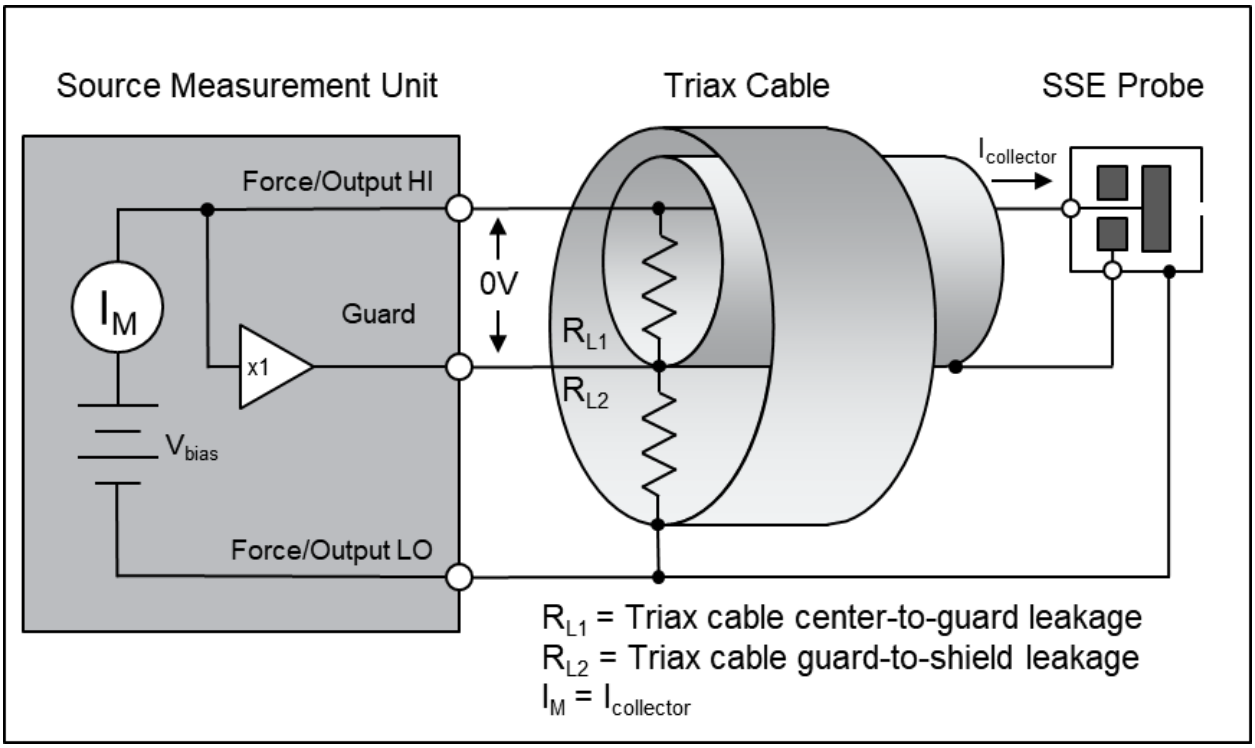

Figure 3.7: SSE Probe measurement configuration using triaxial cable. Figure adapted and modified from Keithley [8]

$$R_{ins} = \frac{\rho}{2\pi L}\int_a^b \frac{1}{r}dr = \frac{\rho}{2\pi L}\ln\left(\frac{b}{a}\right), \tag{3.9}$$

where a and b are the inner and outer conductor radii of the coax cable, respectively. Properties of a common coaxial cable (RG-58) are $a = 0.91\,\text{mm}$, $b = 3.51\,\text{mm}$, $L = 3\,\text{m}$, and $\rho = 160\,\text{T}\Omega\,\text{m}$ [145, 146], which gives $R_{ins} \approx 11.5\,\text{T}\Omega$, and $I_{leak} = 17.5\,\text{pA}$ at $V_{bias} = 200\,\text{V}$. For predicted current levels spanning 1 pA to 250 pA, a leakage current of $I_{leak} = 17.5\,\text{pA}$ introduces unacceptable error in beam measurements at higher angles. Therefore, mitigating leakage current in the signal-carrying lines is necessary for the presented SSE measurement approach, where non-zero voltage biases must be applied to the collector.

Minimizing leakage currents for low level measurements can be accomplished with triaxial cable [8]. A triaxial cable consists of a biased "signal" center conductor that carries the current

signal, a coaxial "guard" conductor that is biased to an identical voltage using a voltage follower, and a coaxial "shield" conductor that is connected to ground. Since the voltage drop between the signal and guard conductors is zero, leakage current from the measurement line should be negligible, with all leakage occurring between the guard and shield conductors.

The SSE Probe is designed around terminating a triaxial cable in a manner that minimizes leakage current within the probe itself, and consists of three internal electrodes that connect to their respective triaxial conductors: the collector electrode, a guard electrode, and a shield electrode. The collector is connected to the signal conductor of the triaxial cable. The collector and guard electrodes have identical diameters, and are axially separated by 3 mm of insulation. The guard and shield electrodes are separated by 15 mm of axial distance. The shield is connected to the body of the probe, which is made of an unanodized lens tube holder from Thorlabs. To ensure vacuum compatibility, all electrical connections are made by mechanical force applied with a wave disc spring between the guard and shield electrodes, and a threaded retaining ring that holds the assembly together. Figure 3.6 shows the complete SSE Probe assembly and a cross-section image of the probe design. Figure 3.7 shows an adapted diagram that illustrates the probe measurement setup [8].

After assembly, the SSE Probe's leakage current was measured with a Keithley 6517B Source Measurement Unit by applying a $\pm 200\,\mathrm{V}$ bias on the signal/guard conductor. Average leakage current for a 3 meter cable was found to be $\sim 600\,\mathrm{fA}$, which is a reasonable leakage current for the predicted current signals.

3.2.3 SSE-Corrected Current Density Distributions

The corrected current density distributions are shown in Figure 3.8. SSE behavior is strongly dependent on incident energy. For lower beam energies (<3 kV), the discrepancy between the uncorrected current signal and "true" current signal is very small. At higher beam energies (>3 kV), the uncorrected current signal can be up to 15% greater than the true signal. For electrospray beams

that rely on emitter bias potentials greater than $\sim 2\,\mathrm{kV}$, SSE cannot be neglected for accurate measurements of the thruster plume.

3.2.4 Energy Distribution Function Estimates of Secondary Species

Using the current-voltage (I-V) characteristics obtained while sweeping the probe shown in Figure 3.9, it's possible to examine the energy distribution function (EDF) of the secondary species. Analyzing the EDF *a posteriori* informs the validity of our low-temperature SSE assumption. Since all secondaries are produced on the collector surface, current collection behaves as a "thin sheath" plasma, so current measurements do not need to be modified to account for sheath effects. The EDF can be approximated by $f(E) \propto d^2J/dV^2$ using the method of Druyvesteyn, where J is the measured current density, and V is the probe bias voltage [147, 148]. The secondary I-V trace shown in Figure 3.9 is obtained by subtracting the current due to primary species from the total measured probe current. The positive and negative species' EDFs shown in Figure 3.9 have respective mean energies of 2.12 eV and 1.94 eV, confirming our low-temperature SSE assumption.

In the context of electrospray devices, the shape of the EDF for secondaries emitted from downstream surfaces bears little significance on behavior of the electrospray itself. However, fitting the curves to a Maxwell-Boltzmann (M-B) distribution gives possible insight into the relevant physics occurring during the impact processes. A nonlinear least squares method was used to fit M-B distributions to the secondary EDFs, which are also shown in Figure 3.9. The fitted M-B curves have temperatures of 1.04 eV and 1.16 eV for the positive and negative species, respectively. The discrepancy between calculated mean energies from the data, and the temperatures from fitted M-B distributions suggest that the EDF curves are non-Maxwellian. Some of the likely SSE mechanisms that occur in electrosprays are non-equilibrium processes, e.g. collision-cascade sputtering, molecular dissociation, or shock-induced desorption. For such non-equilibrium mechanisms, it's reasonable to expect a non-Maxwellian EDF. The measured current represents the aggregate of all currents produced by the different SSE mechanisms, so the presented EDFs likely represent a superposition of many different EDFs belonging to each species.

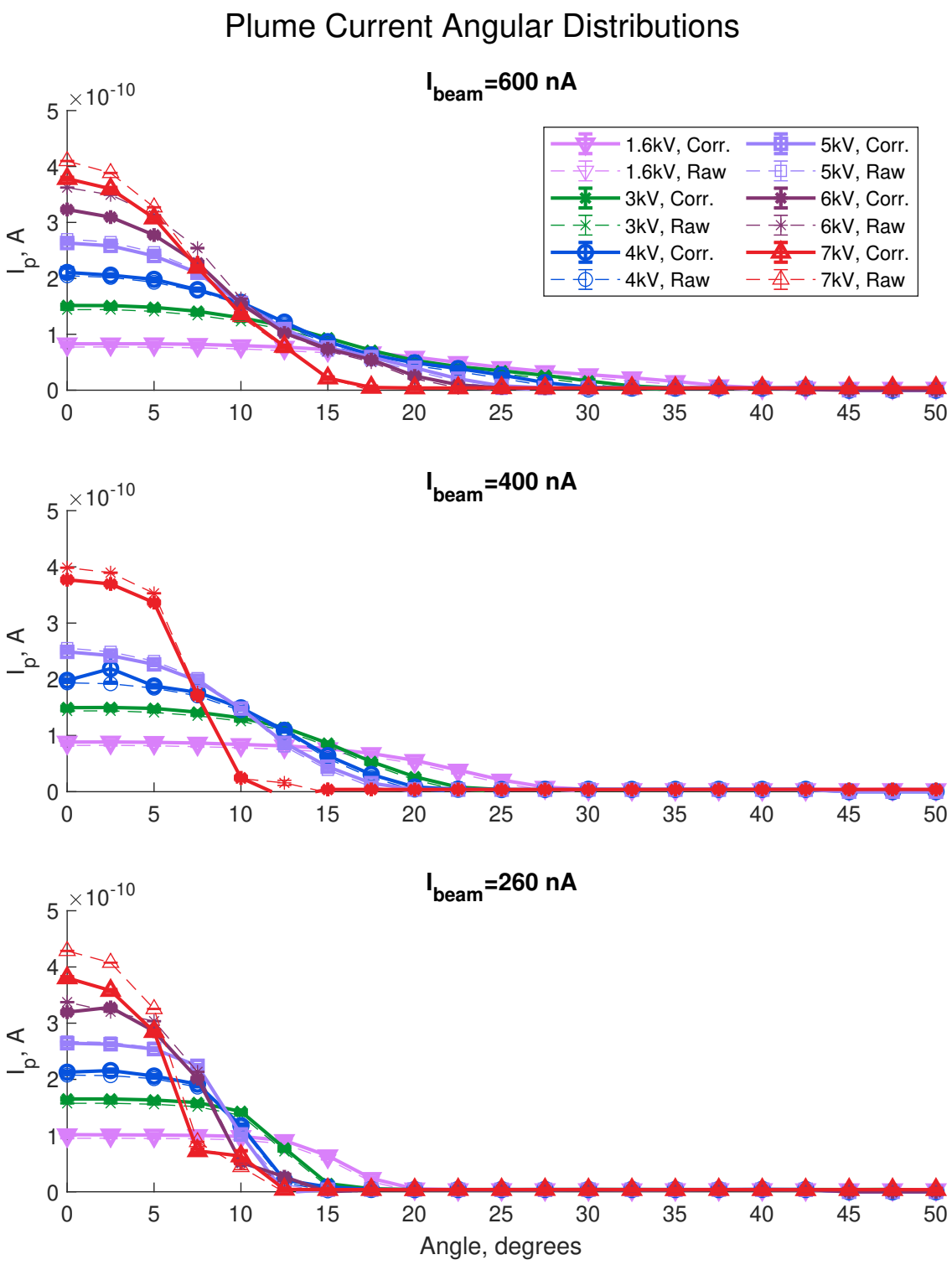

Figure 3.8: Current density distributions for the CMNT at different beam energies. Solid lines show SSE-corrected current distributions and dashed lines show uncorrected current distributions.

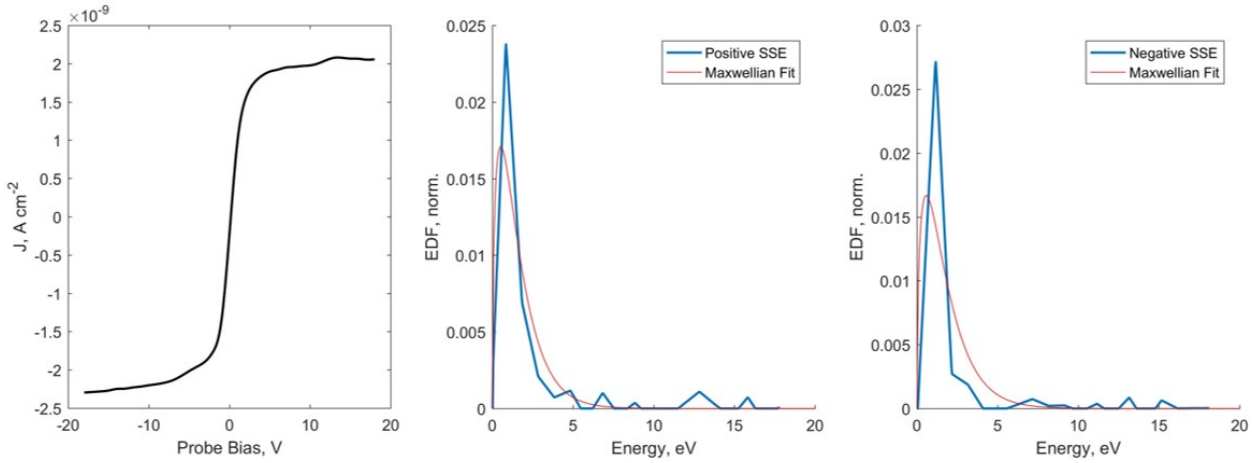

Figure 3.9: Left: Representative I-V trace obtained during the SSE Probe sweeps. Middle: EDF of positive secondary species. Right: EDF of negative secondary species.

3.3 Post-Testing Microscopy of Impinged Surfaces

This section will discuss some microscopy results of surfaces that have been exposed to high-velocity electrospray species. The first set of images comes from a beam target used at JPL to terminate the plume of the Busek CMNT, a droplet-mode electrospray. The second set of images comes from the extractor of a UCLA-developed ILIS thruster that has been heavily impinged by the plume.

3.3.1 Beam Target Microscopy - Evidence of Droplet Desorption

Metallic foams have been shown to reduce the effective sputtering rates in plasmas [149], so a nickel foam beam target was adopted by JPL in an attempt to suppress SSE during ground testing of the Busek CMNT. The nickel foam panels were arranged in a chevron-style configuration to further redirect emitted secondaries away from the thruster. Examining the beam target after several hours of nominal thruster operation (i.e. V_{beam} =6 kV) reveals qualitative insights into SSE spatial dependence. Figure 3.10 depicts ionic liquid propellant deposition from the electrospray's full plume. Mass flux across the plume exhibits a super-Gaussian distribution [144], so we should expect to see propellant accumulation trends that follow a similar profile, i.e. a majority of deposi-

tion in the center that decays with radial extent. Visual inspection of propellant deposition instead shows an annular profile, with negligible accumulation in the center of the plume pattern. Scanning electron microscopy (SEM) images of the target at different radial positions also show the absence of deposited propellant in the center of the plume, and accumulated propellant at farther radial distances. The dry patch observed at the center of the beam target is consistent with shock-induced desorption, where incident droplets undergo a non-isentropic impact process that causes the total gas-phase transition of the droplet and any accumulated liquid on the surface [100, 101]. The images in Figure 3.10 confirm the predicted onset of shock-induced desorption for nanodroplets emitted by the CMNT, as discussed in Chapter 2.2.1. By contrast, Figure 3.11 shows that UCLA's beam target does not exhibit a dry spot across the extent of the plume deposition pattern, which is sensible since UCLA's embodiment of the CMNT operates below the desorption threshold.

Secondary species behavior is strongly dependent on that of the incident primary species, so examining the propellant deposition pattern in Figure 3.10 provides inferred insights into primary plume mechanics. Plume studies conducted by Thuppul et al. [144, 150], obtained the mass flux and current density distributions of the CMNT plume. Taking the ratio of the mass flux and current density distributions gives the mean charge-to-mass ratio (ξ) of the plume, which increases monotonically with polar angle [150]. Based on the splashing thresholds shown in Figure 2.4, higher-ξ droplets should have greater incident velocity, and therefore be further into the shock-induced desorption regime. With those two trends in mind, we should see the prevalence of shock desorption increase with polar angle. Instead, we see desorption in the center of the plume, and deposition on the higher angles.

A portion of the emitted droplets undergo Coulombic fission, resulting in significant loss of charge, yet negligible loss of mass [111]. A retarding potential mass analyzer (RPMA) was developed at UCLA to identify possible neutral or low-ξ mass flux within an electrospray plume [151]. The RPMA consists of repelling electrodes similar to those found in a retarding potential analyzer, but with a quartz crystal microbalance (QCM) used in lieu of a current collector. Results of the RPMA study suggest that between 1% and 10% of the plume is comprised of a population with

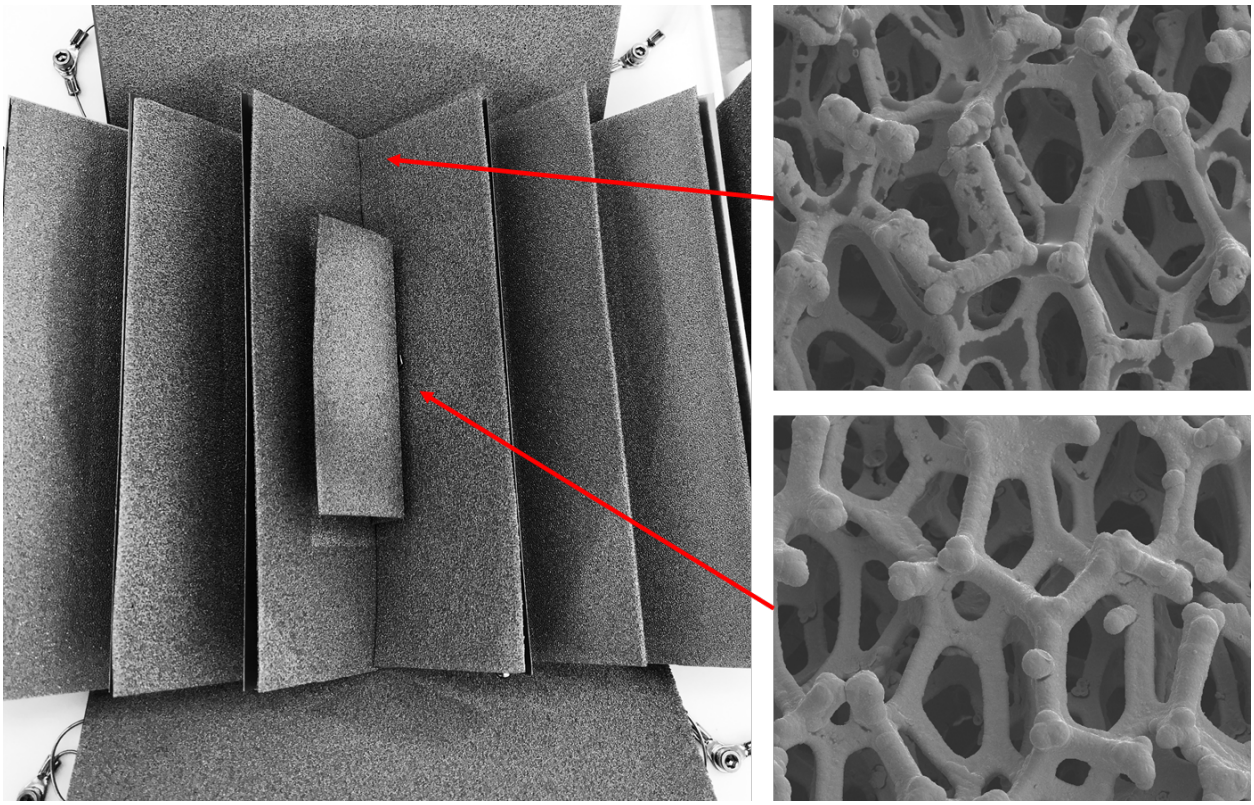

Figure 3.10: Left: Plume pattern observed on the nickel foam beam target. Right Top: SEM image of the visibly wetted region near the periphery of the plume. Propellant has clearly wetted to the foam ligaments. Right Bottom: SEM image of the visibly dry region at the center of the plume. The foam liagments appear devoid of propellant.

negligible charge, which Collins et al. [151] describe as "pseudo-neutral". If Coulombic fission occurs before the primary species are fully accelerated, then the pseudo-neutral population will have a lower terminal velocity, pushing them below the limit of shock-induced desorption. The RPMA results show that pseudo-neutral flux persists across all polar angles. This suggests that shock-induced desorption removes all accumulated propellant from the surface, hence the dry spot in the center and resulting annular deposition pattern.

In summary, the observed propellant deposition pattern may be a result of a subsidiary plume, which consists of pseudo-neutral species born from the Coulombic fission process. The hypothesized subsidiary plume is analogous to the "satellite plumes" observed in atmospheric conditions [57], where the satellite plume is instead caused by drag.

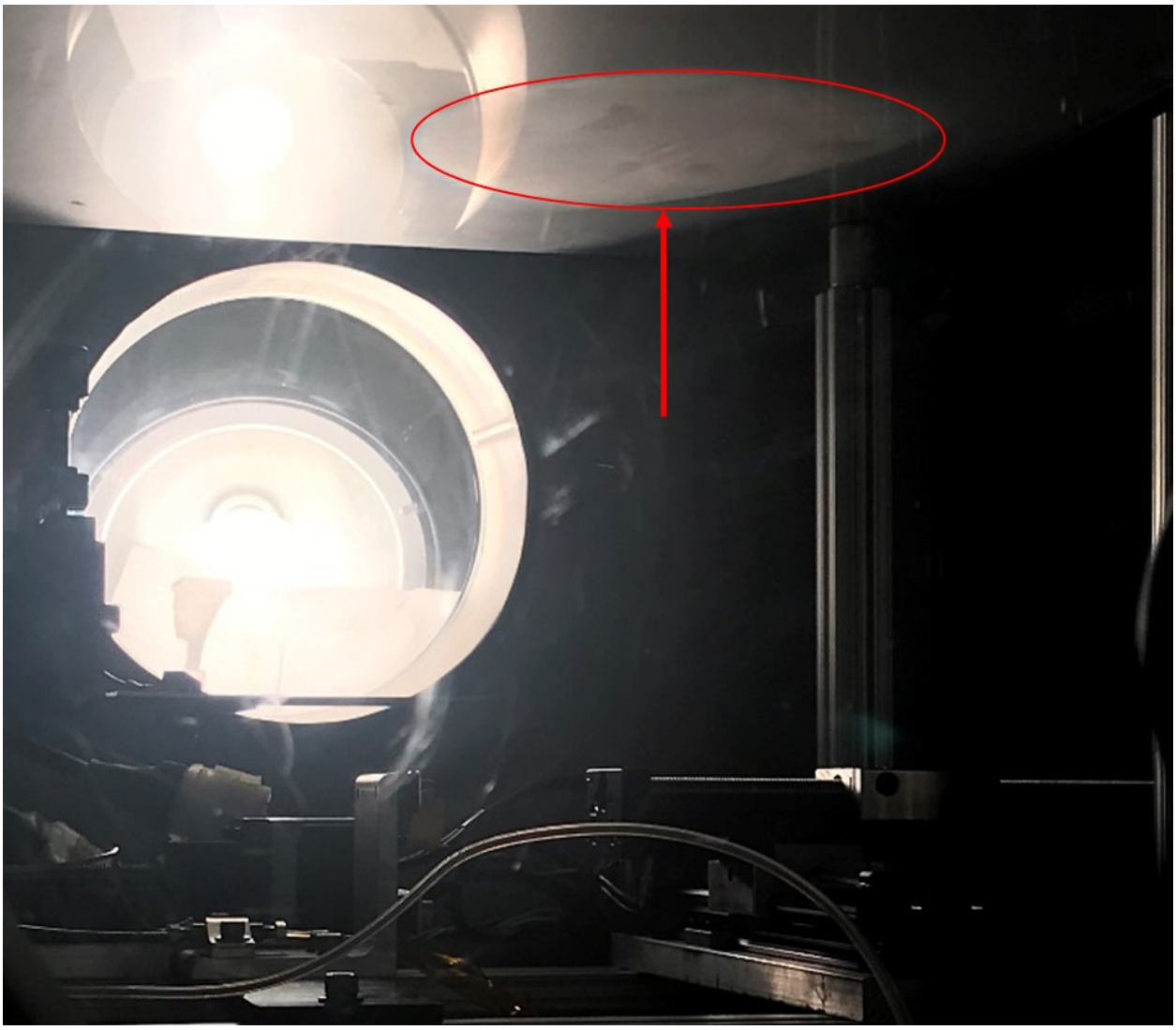

Figure 3.11: Flat plate beam target used to terminate the plume in UCLA's electrospray testing facility. The border of the plume is highlighted with a red circle. No dry patch is observed in the center of the plume deposition pattern, suggesting that UCLA's CMNT configuration operates below the desorption threshold.

3.3.2 Extractor Grid Microscopy - Evidence of Chemical Sputtering

A single-emitter porous tungsten electrospray was developed at UCLA to study transient flow in porous ILIS thrusters [152]. The thruster developed by Wright [152] consists of an electrochemically sharpened porous tungsten emitter, and a 316 stainless steel extractor. The emitter was biased up to 5 kV with respect to the grounded extractor. After 10's of hours of testing, the thruster was dismantled and inspected [153]. Figure 3.12 shows the upstream-facing side of the extractor. The discoloration observed in the upper left image resembles post-test extractor grid images shown by Lenguito et al. [124]. The bottom left image in Figure 3.12 is a control micrograph taken of the extractor prior to thruster firing, where the bottom right image shows the extractor after thruster testing. Comparing the pre- and post-test images, the steel's grain structure becomes clearly visible after exposure to the ILIS plume. The emergence of a grain structure suggests that a chemical reaction is occurring between the impinging plume species and the stainless steel.

Along the grain boundaries in stainless steel, diffusion of carbon leads to the formation of chromium carbides, and diffusion of oxygen leads to formation of iron oxides. Depletion of chromium and enhancement of oxides in the regions adjacent to the grain boundaries causes "sensitization", or decreased corrosion resistance. This process is referred to as "intergranular attack" [154]. Stainless steel is a common material used for [EMI]Im propellant storage or plumbing due to its chemical compatibility with ionic liquids. Corrosion only occurs via electrochemical reactions between the steel and ionic liquid, when the electrochemical window is exceeded within the double layer. Hence, polarity alternation is used for ILIS emitters to minimize electrochemical degradation of metal-liquid interfaces [43, 44]. Propellant storage vessels, plumbing, or grounded extractor electrodes should not experience [EMI]Im corrosion to the extent observed in the bottom-right image of Figure 3.12. Furthermore, the lack of significant deposited material at the site of observation suggests that negligible liquid-phase propellant impinged on the extractor during testing.

Given these observations, it is highly likely that the observed intergranular attack is evidence

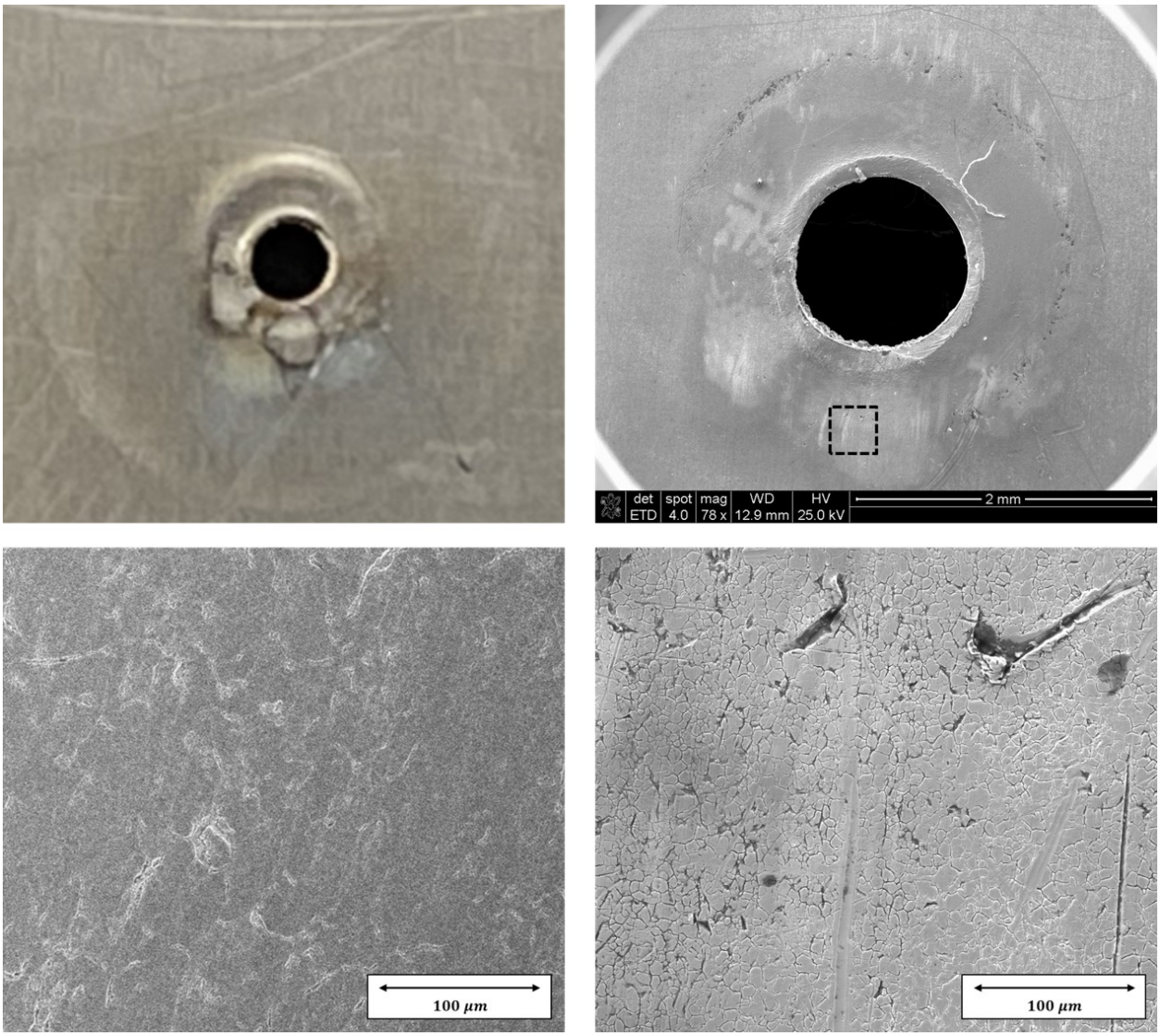

Figure 3.12: Top left: Photograph of the upstream-facing side of the extractor after testing. Blackened regions are clear signs of impingement. Top Right: SEM image of the extractor. The dashed black box represents the region of high-magnification. Bottom Left: High-magnification image of the extractor before firing the thruster. Bottom Right: High-magnification image of the extractor after firing the thruster. The indentations in the upper region of the image are artifacts of the machining process, and not due to plume impingement.

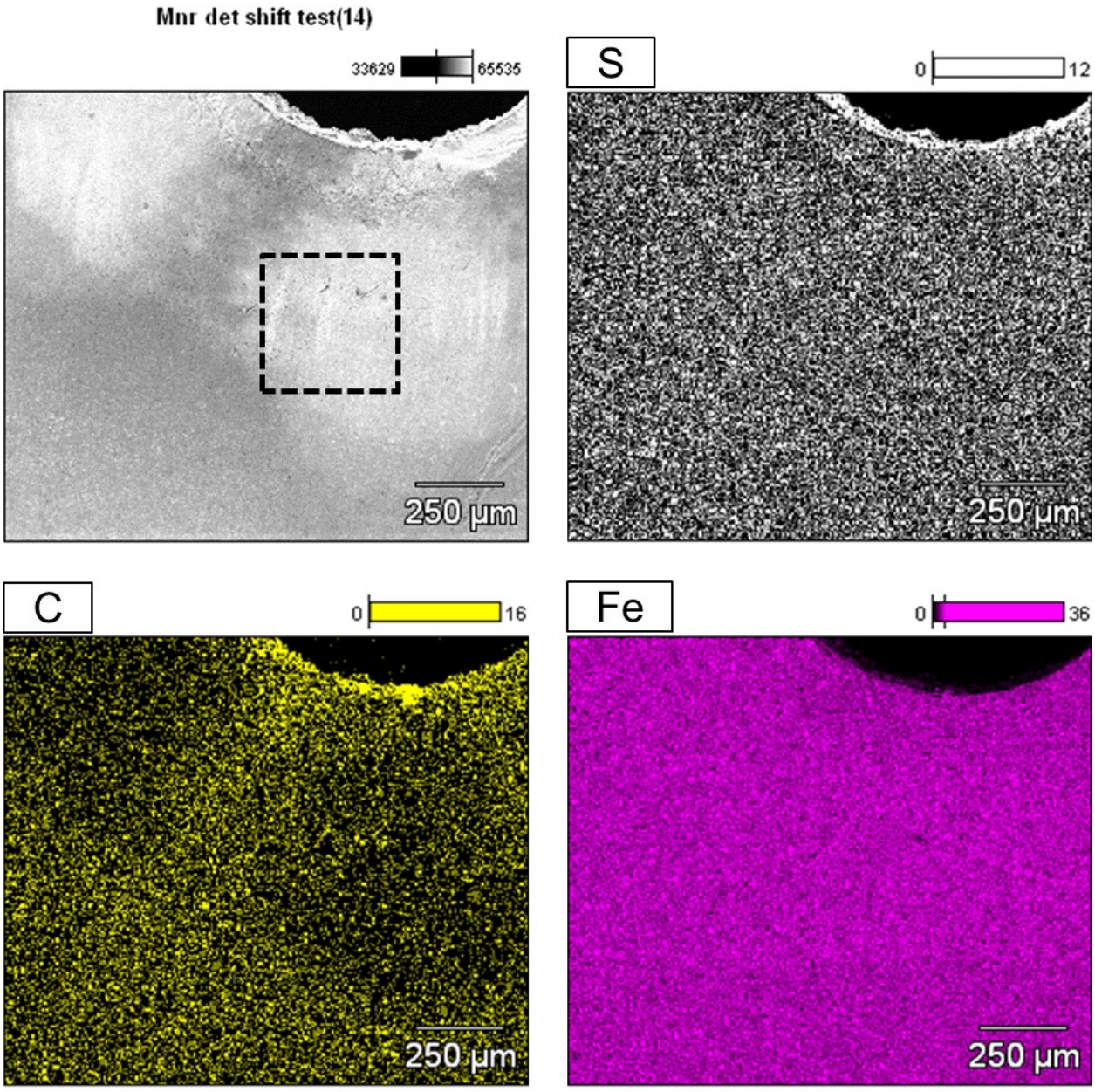

Figure 3.13: Results of EDS spectroscopy of the extractor. The top left image shows the region of interest. The top right, bottom left, and bottom right images show the spatially-resolved results of the EDS scans for sulfur, carbon, and iron, respectively.

of chemical sputtering, since lack of an applied bias on the extractor would preclude electrochemical decomposition. When ions strike the surface, they dissociate into fragments of the primary molecules, which may include compounds that preferentially react with carbides and oxides within the grain boundary.

Energy-dispersive X-ray spectroscopy (EDS) was performed on the extractor to evaluate the makeup of atomic species on the surface. The results of the EDS scan are shown in Figure 3.13, where the dashed square box in the upper left image represents the same image boundary highlighted in Figure 3.12. The "flower-petal" deposition shapes on the extractor are likely due to off-axis emission sites that arose during testing of the emitter [152]. Sulfur is typically a good indicator of propellant deposition for [EMI]Im, yet the trace impurity levels of sulfur in stainless steel obscure indications of propellant deposition on the surface. Instead, there appears to be a deficit of carbon that corresponds to the "flower-petal" shapes see with optical and SEM microscopy. Since chromium carbides are vulnerable to corrosion (i.e. intergranular attack), it is plausible that reactive secondary species interact with chromium carbides to preferentially erode the grain boundaries.

3.4 SSE-Induced Ohmic Dissipation

During performance testing of the Air Force Electrospray Series 2 (AFET-2), Natisin et al. [3] reported a mass utilization efficiency of $\sim$40% measured using total thruster mass loss, showing that the commonly-assumed 100% mass utilization efficiency is invalid. One of the proposed mechanisms for anomalous mass loss is thermal decomposition of the ionic liquid propellant due to transient arcing events. Given the theoretical evidence of SSE discussed in Chapter 2 and experimental evidence of backstreaming secondary currents in Chapter 3.1, it is possible that secondary species may directly impinge upon the emitter. Therefore, it is sensible to explore the sensitivity of ILIS emitters to steady-state heating caused by secondary impingement.

Ionic liquid properties are highly sensitive to temperature changes, with viscosity and con-

ductivity being arguably the most important and sensitive properties. An increase from 25 °C to 30 °C results in a $\sim$ 15% decrease in viscosity and a $\sim$ 36% increase in conductivity for [EMI]Im [155, 156]. For [EMI]BF_4, the same $\Delta T = 5$ °C results in a $\sim$ 17% decrease in viscosity and a $\sim$ 13% increase in conductivity [157, 158]. For porous bulk ILIS devices, viscosity directly affects volumetric flow rate, which scales as $Q \propto 1/\mu$ per Darcy's law describing flow through a porous medium [37]. An order-of-magnitude analysis by Higuera [159] suggests that finite electrical conductivity controls ion evaporation current. Self-heating via Ohmic and viscous dissipation has been considered previously in literature, where Gamero [160] found ΔT for droplet emission to be high enough that it violates the isothermal assumptions used to derive electrospray scaling laws. Recent computational modelling by Magnani and Gamero [161] indicate a temperature rise of $\Delta T \approx$25 °C at the emission site for an ion-mode electrospray due to viscous and Ohmic dissipation. Another important temperature-dependent property of ionic liquids is the vapor pressure, which becomes finite at elevated temperatures (>120 °C for [EMI]Im [162]). SSE-induced Ohmic dissipation is a heating mechanism distinct from the self-heating considered in previous studies [160, 161], which is caused by the flow of current due to secondary species impinging on the emission site. It is hypothesized that evaporation and decomposition of propellant at the emission site due to SSE-induced Ohmic dissipation is a possible explanation for the anomalous neutral mass loss reported when testing the AFET-2 thruster [3].

To support the hypothesis of neutral mass loss via Ohmic dissipation caused by backstreaming secondary species, the following Chapter derives an analytical heat and mass flux model of a porous bulk emitter. Using the analytical model, the sensitivity of neutral mass loss to backstreaming secondary current will be examined. The geometry of an emitter can be modeled as a segment of a spherical shell. Assuming axisymmetry and that temperature gradients in the polar-direction are small, an emitter may be modeled as a steady, one-dimensional heat transfer problem. From Fourier's law of heat conduction,

$$\frac{dT}{dr} = -\frac{q''}{k}, \tag{3.10}$$

where q'' is heat flux, k is thermal conductivity, T is temperature, and r is the radial distance. Per

the Stefan-Boltzmann law, radiative heat flux is

$$dq''_{rad} = \varepsilon_e \sigma_{sb} dA_s (T^4 - T_\infty^4) \tag{3.11}$$

where ε_e is emissivity, $\sigma_{sb} = 5.67 \times 10^{-8} \mathrm{W/m^2K^4}$ is the Stefan-Boltzmann constant, dA_s is a differential element of surface area, and T_∞ is ambient temperature. Assuming that the cross sectional area varies slowly along the length of the emitter, the energy equation reduces to:

$$\frac{d^2T}{dr^2} + \frac{\varepsilon_e \sigma_{sb} P}{kA_c}(T_\infty^4 - T^4) = 0, \tag{3.12}$$

where A_c is the mean cross-sectional area and P is the mean perimeter of the emitter's cross section. Equation 3.12 may be linearized by taking a first-order Taylor series expansion of the radiation heat transfer term, giving a linear second-order ordinary differential equation:

$$\frac{d^2T}{dr^2} + \frac{4\varepsilon_e \sigma_{sb} P T_\infty^3}{kA_c}(T_\infty - T) = 0 \tag{3.13}$$

We apply an isothermal boundary condition at the emitter base ($T(r=0) = T_\infty$), and use equation 3.10 as a constant heat flux boundary condition at the emitter tip. Applying the boundary conditions results in an expression for the temperature profile of an emitter:

$$\begin{aligned} T(r) &= -c_0 \exp(ar) + c_0 \exp(-ar) + T_\infty, \\ c_0 &= \frac{q''}{k\, a} \frac{\exp(ah)}{\exp(2ah)+1}, \\ a &= \left(\frac{4\varepsilon_e \sigma_{sb} P T_\infty^3}{kA_c} \right)^{1/2}, \end{aligned} \tag{3.14}$$

where h is the emitter height, and q'' is the applied heat flux boundary condition, which we will elaborate after discussing the mass flux model.

Neutral mass loss is caused by evaporation and decomposition of the ionic liquid. The temperature-dependent mass loss due to vaporization may be modeled with the Langmuir equation [163, 164,

165]:

$$\dot{m}_{vap}(T) = K_1 K_2 \frac{\exp(-\Delta H_{vap}/RT)}{T^{1/2}}, \tag{3.15}$$

where R is the universal gas constant, $\Delta_{vap}H$ is the enthalpy of vaporization, and K_1 and K_2 are empirical constants discussed in Appendix A. Mass loss due to decomposition can be modeled by the Arrhenius equation [163, 162]:

$$\dot{m}_{dec}(T) = K_2 K_3 \exp(-E_a/RT), \tag{3.16}$$

where E_a is activation energy and K_3 is another empirical scaling constant discussed in Appendix A.

Neutral mass loss rate from the total emitter surface is found by substituting equation 3.14 into equations 3.15 and 3.16, and integrating over the length of the emitter. The aggregate neutral mass loss rate at a given temperature is then the sum of the mass loss rates,

$$\dot{m}_{neut}(T) = \dot{m}_{vap}(T) + \dot{m}_{dec}(T) \tag{3.17}$$

The choice of input parameters for the presented heat and mass flux model are informed by performance values from the AFET-2 operating at its 700 µA setpoint, since these are the only published performance results using a total mass loss measurement, which does not neglect neutral mass flux [2, 3]. Natisin et al. [3] reported an emission current of $I_{em} \approx 1.2\,\mu A$ per emitter, emission voltage of $\phi_{em} = 1850\,V$, emitter height of $h \approx 300\,\mu m$, and total average neutral mass flow rate of $\dot{m}_{neut} = 0.86\,\mu g\,s^{-1}$. While the AFET-2 was tested with [EMI]BF_4, empirically obtained values for K_1, K_2, and K_3 are unavailable in literature. Thermophysical properties for [EMI]Im are very similar to those of [EMI]BF_4, so the empirical constants for [EMI]Im were used for the presented analysis.

Modern porous bulk electrospray thrusters are fabricated out of porous borosilicate glass [35, 42, 2] or xerogel/aerogel substrates [166, 167]. Micro- and nano-scale porous materials are excel-

lent insulators, with thermal conductivity ranging from $0.001\,\mathrm{W\,m^{-1}\,K^{-1}}$ to $0.1\,\mathrm{W\,m^{-1}\,K^{-1}}$, often much lower than any gases or liquids they contain [168, 169]. Subsequently, we neglect heat conduction through the porous substrate, and only consider the thermal conductivity of [EMI]BF_4. Remaining thermophysical properties used in the presented analysis are shown in Table B.1.

The constant q'' boundary condition applied in equation 3.14 is a balance between SSE-induced Ohmic dissipation, and cooling due to evaporation and decomposition mass loss. The heating caused by backstreaming secondary species that are accelerated to the emitter potential is a given by,

$$q''_{bs} = j_{bs}\phi_{em}, \tag{3.18}$$

where j_{bs} is the backstreaming secondary current density, which is used as a free parameter to explore the thermal response of the system. Cooling due to evaporation and decomposition are

$$q''_{vap} = \frac{\Delta H_{vap}}{M}\dot{m}_{vap}, \tag{3.19}$$

$$q''_{dec} = \frac{E_a}{M}\dot{m}_{dec}, \tag{3.20}$$

where $M = 0.226\,\mathrm{kg\,mol^{-1}}$ is the molar mass of [EMI]BF_4. The total heating applied to the emitter is then

$$q'' = q''_{bs} - q''_{vap} - q''_{dec} \tag{3.21}$$

An initial guess for the temperature profile neglects the cooling contribution, and then evaluates them iteratively until the temperature profile converges.

Figure 3.14 shows the emitter tip temperature plotted against the backstreaming current density, which is normalized against the emitter current density,

$$j_{em} = I_{em}/(2\pi R_{tip}^2), \tag{3.22}$$

where $R_{tip} \approx 10\,\mu\mathrm{m}$ is the emitter tip's radius of curvature. A value of j_{bs}/j_{em}=0.052% may cause

a ΔT =5 °C, which suggests that isothermal assumptions made when deriving ILIS thruster scaling laws may be invalidated if SSE is not appropriately mitigated. Figure 3.14 shows the total neutral mass loss versus normalized backstreaming current, where a value of j_{bs}/j_{em}=2.65% corresponding to an emitter tip temperature of 279 °C may cause the measured $\dot{m}_{neut} = 0.86\,\mu g\,s^{-1}$. The presented results suggest that mass loss via thermal effects are highly sensitive to backstreaming current, and that relatively modest backstreaming currents may significantly alter thruster performance. The temperature rise ceases at approximately 360 °C, when cooling due to propellant phase change equalizes with the heating due to backstreaming secondaries. Since the emitter cools as it evaporates propellant, our model suggests that thermal effects alone cannot cause decomposition of propellant. Therefore, neutral mass loss due to SSE-induced Ohmic dissipation is solely due to evaporation. The presented heat and mass flux analysis only examines thermal effects, yet other mechanisms may contribute to anomalous mass loss. Dissociation caused by heavy species impinging on propellant at the emitter's surface (see Chapter 2.1), and electrochemistry at the emission site are pathways for decomposition that is not described by our heat flux model.

The TRIM analysis by Magnusson et al. [87] estimates an IIEE yield of ~ 1 electron per incident ion at $\phi_{em} = 1850\,V$, which agrees well with experimental measurements of IIEE yields between ~ 0.75 and 1.25 electrons per ion at ϕ_{em} =2 kV to 3 kV [130]. Furthermore, Klosterman et al. [130] found that 85-90% of the backstreaming secondary current was collected by the emitter, lending credence to our mass flux model results suggesting the j_{bs}/j_{em} =2.65% required to induce the measured $\dot{m}_{neut} = 0.86\,\mu g\,s^{-1}$.

While SSE-induced Ohmic dissipation can detrimentally affect performance and life for ILIS thrusters, LMIS thrusters experience somewhat different consequences. The pure liquid metals used in LMIS devices do not undergo chemical decomposition as ionic liquids do when exposed to high temperatures, nor do they exhibit the same extent of temperature sensitivity. Furthermore, liquid metals have thermal conductivities orders of magnitude greater than ionic liquids, so they are much more effective at carrying heat away from the emission site. However, LMIS thrusters require active propellant heating to keep the propellant in a liquid state, so SSE-induced Ohmic

dissipation may cause localized heating that might affect the flow of propellant to the emitter structures.

One consequence of backstreaming secondaries on LMIS thrusters unrelated to Ohmic dissipation is the accumulation of material at the emitter tip, which modifies the Taylor cone base radius and subsequent thruster mass utilization efficiency [170]. Another consequence may be contamination of the emitters by sputtered extractor or beam target material. When performing post-fire examination of their indium LMIS, Tajmar et al. [13] observed stainless steel contamination on the porous tungsten emitters, and attributed the 2 kV to 4 kV increase in required extraction voltage to the accumulation of contaminants over the 500 hour performance test. A steadily increasing extraction voltage required to maintain the same level of emitter current is known as "emission decay," and has previously been observed in ILIS devices [43, 42]. Emission decay has been attributed to electrochemical degradation of ionic liquids at the electrode interface [171], which motivates the use of polarity alternation [43] and distal electrodes [44] to prevent the double layer potential from reaching the electrochemical window. However, even when applying alternating polarities and using distal electrodes, emission decay persists in ILIS thrusters [54].

Given the lack of electrochemical decomposition processes in liquid metals, and the common observation of emission decay among both LMIS and ILIS thrusters, contamination due to backstreaming secondary species may be another mechanism that contributes to emission decay in ILIS thrusters. Precipitate byproducts formed due to collision-induced dissociation, rheological changes that ionic liquids undergo when bombarded with high-energy electrons [126, 172], and accumulation of sputtered steel contaminants from the facility [13] likely promote pore clogging, increasing the emitter's hydraulic resistance, thus causing emission decay. Pore clogging due to backstreaming contaminants suggests that space weather may detrimentally impact ILIS thruster flight performance and life. However, incorporating SSE-mitigating elements into ILIS thruster designs may have the added benefit of ameliorating the effects of interactions with ambient space plasma.

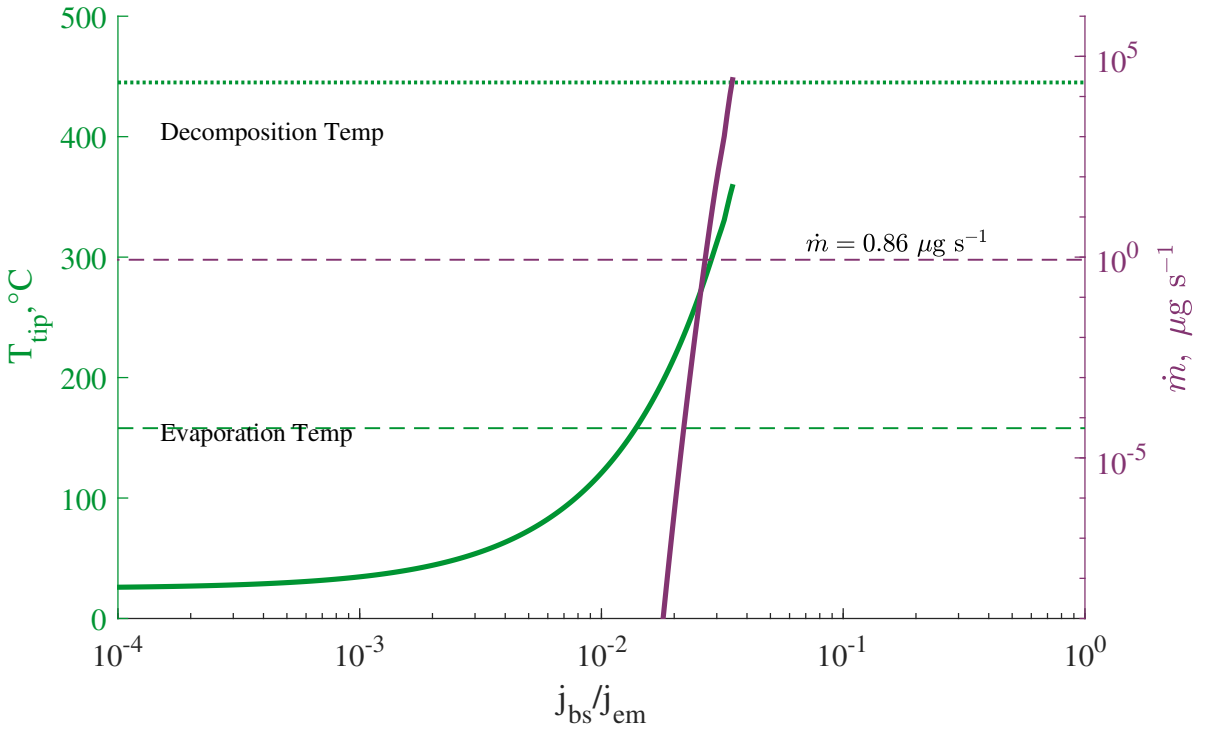

Figure 3.14: Emitter tip temperature and mass loss rate results from the presented analytical model. Backstreaming current density is normalized against the emission current density. (Left Axis): Propellant temperature at the emission site due to SSE-induced Ohmic dissipation, assuming a base temperature of 25 °C. The vaporization temperature threshold of [EMI]BF_4 is not well characterized, so the green dashed line marks the 158 °C where [EMI]BF_4 enthalpy of vaporization measurements have been obtained [9]. The green dotted line marks the 445 °C threshold where [EMI]BF_4 decomposes [10]. (Right Axis): Neutral mass flow rate as a function of the normalized backstreaming current density. The purple dashed line represents $\dot{m}_{neut} = 0.86\,\mu g\,s^{-1}$ measured on the AFET-2 thruster [3]. Based on our model, the experimentally measured neutral mass loss is achieved when j_{bs} =2.65% of the emitter current density, indicating the significance of even modest backstreaming currents on thruster facility effects.

3.5 SSE-Induced Glow Discharges in Electrospray Thrusters

3.5.1 Discussion

With the notion of omnipresent SSE in ground testing of electrospray thrusters, published observations of glow discharges in ILIS thrusters invite scrutiny of the possible mechanisms that may lead to glow from ILISs and LMISs operated in vacuum [11, 14, 173, 12, 174]. A few examples of glowing electrospray thrusters are shown in Figure 3.15. A glow discharge is a type of electrical discharge that is caused by the ionization of a gas surrounding a conductor [175]. Glow discharges are sustained by an electron avalanche, where free electrons are accelerated by an electric field and collide with neutral gas molecules, which produces additional free electrons, and so on. The resulting plasma consists of ions and neutral atoms that may become excited and then emit light when reverting to their ground state.

Electrical discharges have been identified as a failure mechanism in ILIS electrospray thrusters [44, 45]. However, previous studies focused on the formation of electrical arcs, which are distinct in character from glow discharges. Arc discharges are highly transient and have orders of magnitude higher current density than glow discharges, resulting in extreme temperatures and nearly instantaneous decomposition of propellant at the emission site. Arcing in electrosprays is relatively straightforward to identify by monitoring electrode current for transient overcurrent events, or using long-distance microscopy to monitor the emission site for bright sparks. Glow discharges have much lower current density and fainter light emission than arcs, which may cause glow discharges to go unnoticed during ILIS thruster testing, since very long shutter exposures may be required to observe thruster glow.

While electrosprays are used to generate charged particle beams, they are not technically considered plasma-generating devices since the electrospray ionization mechanism relies on the direct solvation of ions from an emission cone [176], rather than stochastic impact-ionization or thermionic emission processes in gaseous discharges. The ion evaporation process may induce rotational and vibrational energy in the emitted species [177], but spectra associated with rovibra-

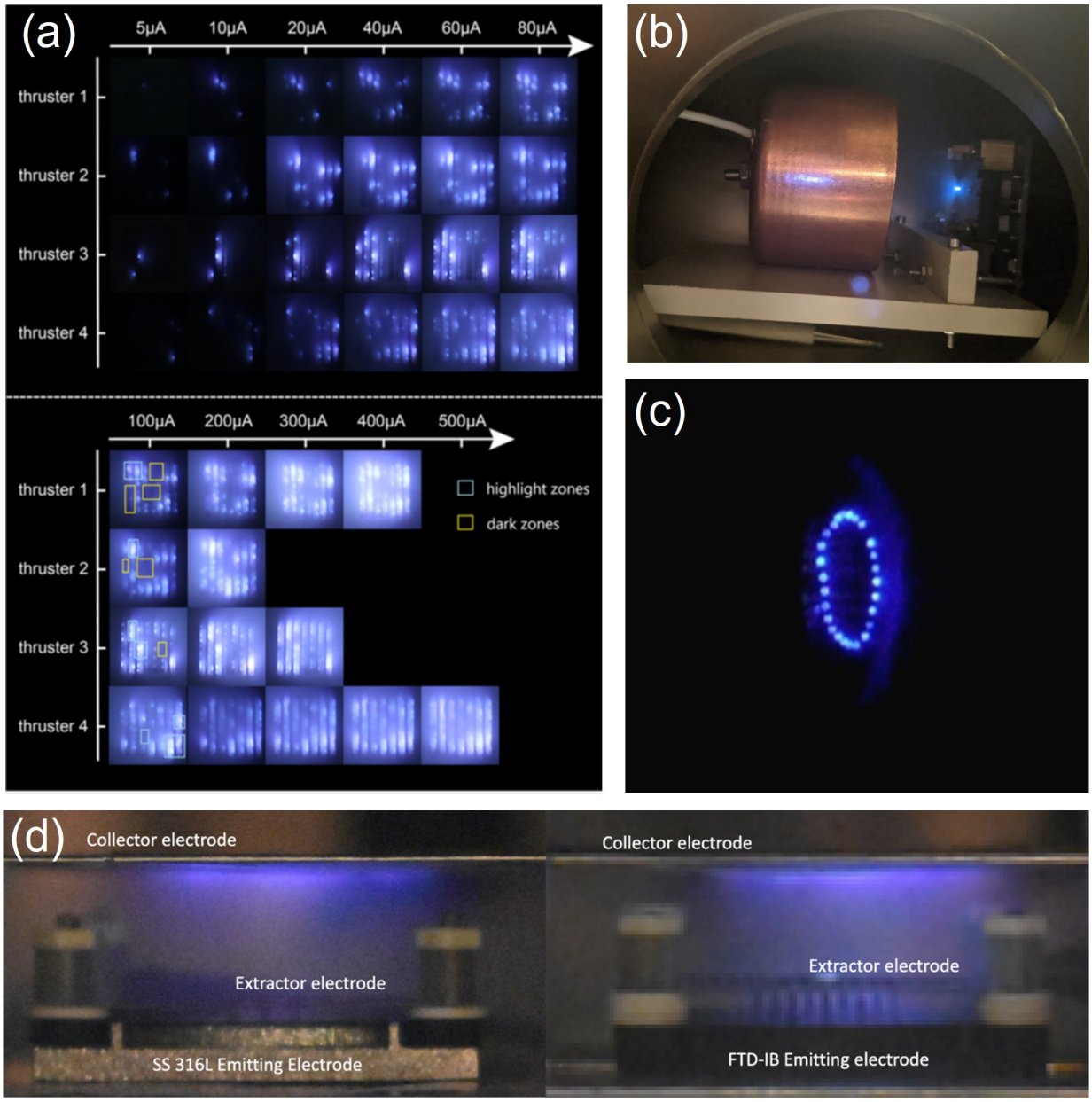

Figure 3.15: Glow discharge images. (a) Porous bulk ILIS thruster operating with [EMI]BF_4 reported by Chen et al. [11] that experienced persistent glow, although the authors also report some arc discharges at elevated emission currents. Reprinted from Ref [11] with permission from Elsevier. (b) Bright glow in a porous bulk thruster operating with [EMI]BF_4 reported by Bretti [12]. Reprinted from Ref [12] with permission from Michael Bretti. (c) An indium LMIS "crown emitter" during a 500 hour performance characterization reported by Tajmar et al. [13]. Reprinted from Ref [13] with permission from Elsevier. (d) Glow at the emission site and collector during the operation of an additively-manufactued ILIS thruster by Máximo et al. [14]. The collector is located 8.5 mm downstream of the thruster. Reprinted from Ref [14] with permission from Elsevier.

tional modes generally fall in the microwave to infrared range [108]. Electronic transitions are necessary to induce the visible wavelength glow seen in electrospray thrusters. Electron exchange does occur in electrospray devices, but not at the site of emission. All molecular constituents in a room temperature ionic liquid are charged, existing in a "pre-ionized" state. Electric double-layers form at biased conductive surfaces in contact with the ionic liquid, similar in principle to sheaths forming at boundaries in a plasma [43]. All electron charge transfer associated with electrospray ionization occurs within the electric double layer [42] inside of the ionic liquid, and does not manifest as a glow discharge in the plume.

3.5.2 Optical Emission Spectra of Electrospray Glows

The Highly Optimizable Apparatus for Groundbreaking Investigations of Electrosprays (HOAGIE) is a high-vacuum testing facility developed at the University of California, Los Angeles for characterizing the life- and performance-limiting mechanisms in electrospray propulsion devices [178, 144, 122, 179]. For the presented study, an ILIS was installed in HOAGIE such that the principal emission axis was orthogonal to the cylindrical chamber's axis, with the beam terminated by a hemicylindrical target. The beam target geometry permitted collection of the full ILIS plume, while maintaining $\sim 55\,\text{cm}$ of distance between the ILIS and nearest downstream surface. The chamber was pumped to high vacuum ($\sim 0.133\,\text{mPa}$) using a CTI-Cryogenics 10-inch cryogenic pump. All experiments were performed with the ionic liquid propellant 1-ethyl-3-methylimidazolium bis(trifluoromethylsulfonyl)imide , or [EMI]Im ($C_8H_{11}F_6N_3O_4S_2$). The propellant was conditioned and vacuum dried to ensure minimal water content, in accordance with best practices for ionic liquid electrospray operation [46]. Collection optics used in the presented experiment consisted of a multimode fiber coupled to a collimating lens positioned 15 cm from the ILIS, giving an approximately 1 cm spot size on the extractor face. The optical fiber was fed to an Ocean Insight FLAME series spectrometer, which has spectral resolution of 1.37 nm. A long-exposure camera was used to capture images of glow in the chamber. A diagram of the experiment setup is shown in Figure 3.16.

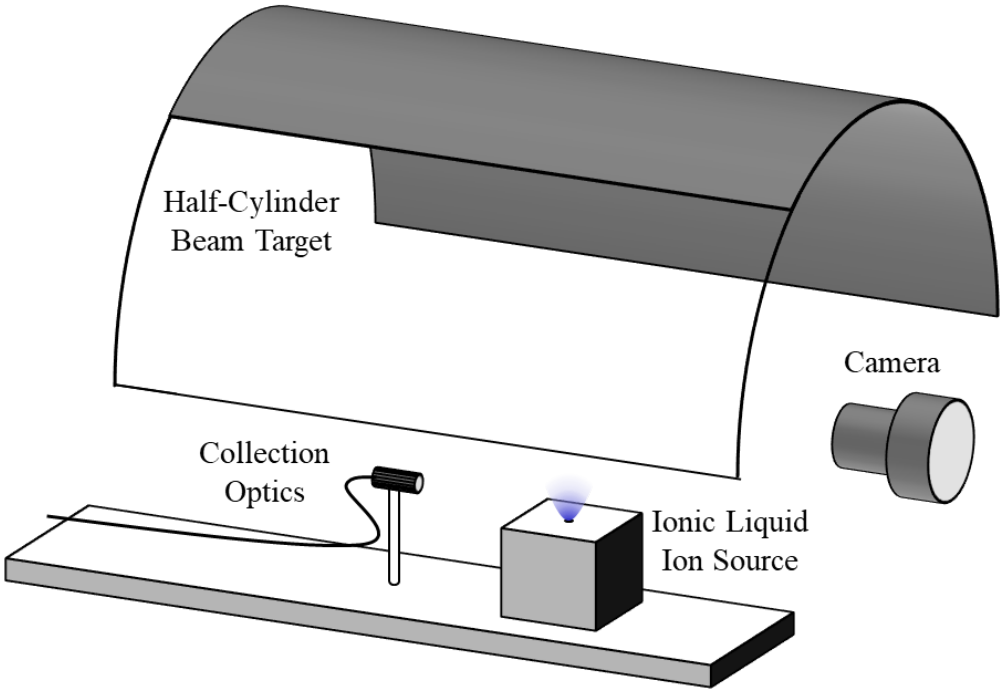

Figure 3.16: Optical emission spectroscopy setup

Figure 3.17 shows the beam target during and after operating the ILIS. The image taken during operation (left image) required 10's of seconds of exposure time to capture the observed glow, which illustrates the low intensity of optical emission for electrospray devices. To achieve sufficient signal-to-noise ratio, the OES study was carried out at the maximum emitter current operating point, where glow has the highest intensity. The operating point corresponded to a beam energy of approximately 2.5 keV. Results of the OES study shown in Figure 3.18 are broken down into three different emission structures of interest: nonmetal atomic lines, metal atomic lines, and molecular line shapes. All atomic spectra were compared to the NIST Atomic Spectra Database [180].

The first emission structures of interest are atomic lines of excited neutral and ionized nonmetal elements that constitute [EMI]Im, including hydrogen, carbon, nitrogen, oxygen, fluorine, and sulfur. Observation of the atomic constituents of [EMI]Im suggests that photon emission induced by dissociation of molecular ions contributes to the observed glow. Molecular dissociation

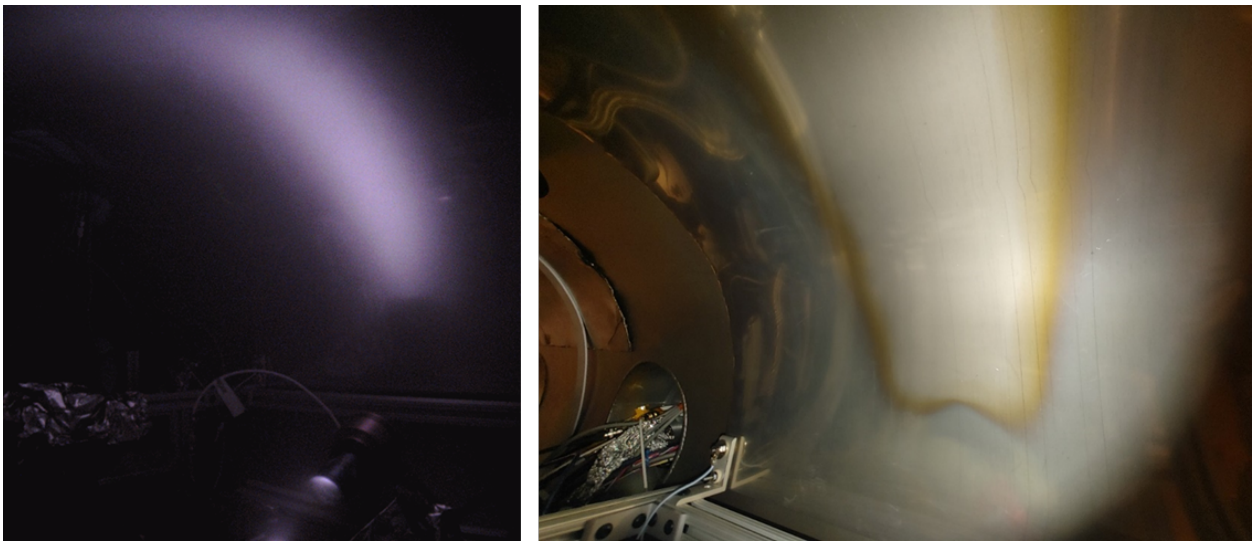

Figure 3.17: Left: Image of glow occurring at the beam target during operation of the ILIS. Right: Image of beam target post-testing.

occurs when the kinetic energy of impact is converted to internal energy of the molecule, which cleaves bonds and breaks the molecule into fragments. The specific energy threshold for molecular dissociation is approximately $1\,\mathrm{eV\,u^{-1}}$ with specific energy estimated as $e = q\phi_b/m$, where q is the ion charge, ϕ_b is the beam energy, and m is the mass in *amu*. For the ILIS operating point in the presented experiment, the specific energy of monomers, dimers, and trimers is $22.5\,\mathrm{eV\,u^{-1}}$, $4.9\,\mathrm{eV\,u^{-1}}$, $2.8\,\mathrm{eV\,u^{-1}}$, respectively. Therefore, even the largest expected charged molecules will be well above the dissociation threshold.

The second set of emission structures are atomic lines of excited neutral metallic elements that make up the ILIS extractor grid. The presence of atomic metal lines indicates that photon emission induced by kinetic sputtering also contributes to the observed glow. LMIS devices produce atomic metal ion beams instead of molecular ion beams, so glow observed in LMIS devices is likely dominated by sputter-induced photon emission. Sputtering of extractor grid material has significant implications for device lifetime [51].

The third emission structure of interest is the wide spectral band that emerges from 500 nm to 800 nm. In plasma discharges using complex gas mixtures, the abundance of molecular transitions

generate many line shapes that superpose to produce a wideband continuum spectrum [181, 182, 183]. The emergence of a wideband line shape in the electrospray glow spectra further supports the notion that the observed glow is due to photon emission induced by molecular ion dissociation. Analyzing molecular spectra requires *a priori* knowledge of the reaction products and temperatures to properly utilize spectral fitting algorithms or molecular transition databases. The temperature of the emitted species may likely be between 1 eV and 2 eV per EDF estimates obtained in Chapter 3.2.4. However, the dissociation products this system are unknown, so it is prohibitively challenging to attempt in-depth molecular band matching without results informed by molecular dynamics.

These findings show that the glows from electrospray devices are not directly caused by the electrospray emission process, but rather by photon emission due to high velocity impact of emitted species on downstream surfaces.

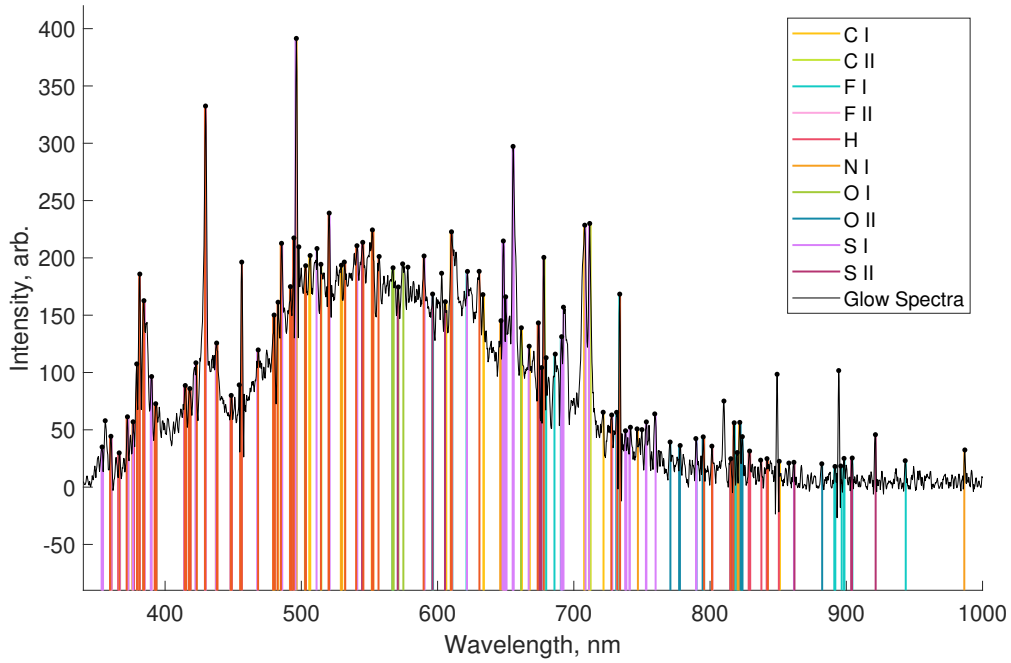

((a)) Nonmetal atomic lines.

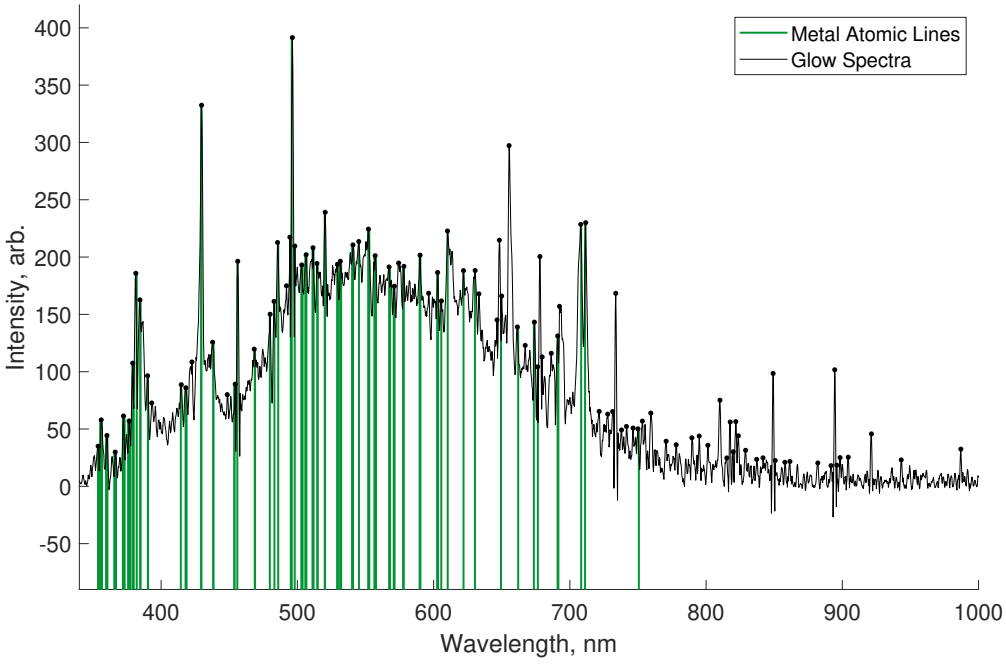

((b)) Metal atomic lines.

Figure 3.18: ILIS device spectra and lines matching the first 60 peaks.

3.6 Conclusions

The experimental and analytical studies presented in Chapter 3 examined the consequences of SSE on electrospray thruster behavior, including measurement uncertainty, thruster-to-facility coupling, performance loss, and potential life-limiting phenomena.

The beam target biasing experiment in Chapter 3.1 illustrated the coupling between thruster and facility that is caused by SSE. SSE can contribute to significant uncertainty in lifetime estimates if not appropriately mitigated. Different regimes of operation were identified based on the applied beam target bias, and the total facility current response.

Chapter 3.2 provided a detailed study of SSE-induced measurement uncertainty for plume current. The selective secondary species suppression technique discussed in Chapter 3.2.1 quantifies electrospray SSE by taking advantage of the bipolar sensitivity of secondaries to an applied voltage, and the large energy discrepancy between primary and secondary species. Selective suppression may be applied to correct any electrospray diagnostics that rely on current measurements, such as Faraday probes or other current collectors, such as those used in retarding potential analyzers (RPAs). To rigorously quantify positive and negative charge yields, a bespoke "SSE Probe" was developed and tested with an ionic liquid electrospray device. The SSE Probe was successfully employed to obtain SSE-corrected beam current measurements, which also provide positive and negative SSE yields (to be discussed in Chapter 4.3). The presented experimental data represent the first reported spatial distributions of positive and negative charge yields obtained in an ionic liquid electrospray plume.

The SEM micrographs discussed in Chapter 3.3 show different surfaces after exposure to electrospray plumes, providing insight into the phenomena that contribute to SSE. Images of the beam target exposed to a droplet-rich plume confirms the predicted onset of shock-induced desorption at elevated beam energies. Microscopy of an ILIS extractor reveals chemical etching likely due to reaction with dissociated molecular constituents. Both images provide visual evidence of SSE effects occurring in electrospray devices.

The heat and mass flux models in Chapter 3.4 show that backstreaming secondary species may induce Ohmic dissipation at the emission site. Backstreaming current density contributing to 0.052% of emitter current density can cause physical property variation in the ionic liquid that alters the thruster's emission characteristics, invalidating the isothermal assumption used to derive scaling laws. SSE-induced Ohmic dissipation may also cause anomalous neutral mass loss, which is a major performance limitation in ILIS thrusters. Secondary current density contributing to 2.65% of emitted current may cause the $0.86\,\mu g\,s^{-1}$ neutral mass flow rate observed in the AFET-2 thruster [3].

The results of the optical emission spectroscopy study in Chapter 3.5 strongly suggest that glow observed when operating ILIS devices in vacuum is caused by electron excitation resulting from surface impact phenomena such as sputtering and molecular dissociation. These findings support the hypothesis that surface-localized glow observed when operating ionic liquid electrosprays in high vacuum, whether on thruster components or at facility walls, is attributed to secondary species emission (SSE) caused by impact of high velocity primary species on surfaces. As a corollary, glow will not occur in electrospray devices if the emitted species do not impact surfaces. Therefore, glow for electrospray devices is primarily an indicator of plume impingement on the downstream electrodes of the electrospray device and downstream facility surfaces.

CHAPTER 4

Secondary Species Transport Model

Simulating electrospray emission for propulsion devices is a multi-scale/multi-physics modelling problem [133, 134, 55, 131, 122, 179, 184, 135, 185]. To rigorously predict the lifetime of electrospray devices, the UCLA Plasma & Space Propulsion Laboratory has adopted the strategy of discretizing the electrospray domain into different regions where certain physics dominate and others can be neglected [179]. Figure 1 shows a diagram of the domain discretization approach [55]. The PSPL electrohydrodynamic (EHD) emission model simulates the continuum process of electrified conical meniscus formation, conversion to a forced jet, and breakup into droplets [131, 186]. The Discretized Electrospray Lagrangian Interaction (DELI) model is an N-body approach to computing the interaction of the polydisperse species emitted from jet-breakup to produce plume shapes that may be analyzed with simple non-coulombic paraxial trajectories [55, 135]. The Propagation of Electrospray Plume Particles in the Exhaust Region (PEPPER) model is a Bayesian Inference approach to determining the trajectories of plumes that leave the interaction region, and travel downstream [184]. A final element of the modelling approach is interpreting computational simulation results to experimental measurements, and vice versa. Accordingly, the ESCARGOT model was developed to provide bidirectional interpretation between modelling results and experimental measurements. In other words, ESCARGOT can use modelled plume distributions to predict measured impingement currents, or take experimental current measurements to interpret to actual plume distributions that may be compared to models. SSE is the greatest contribution to discrepancies between model and experiment, so the formalism presented in Chapter 4 describes the emission and transport of secondary species within an electrospray thruster testing facility.

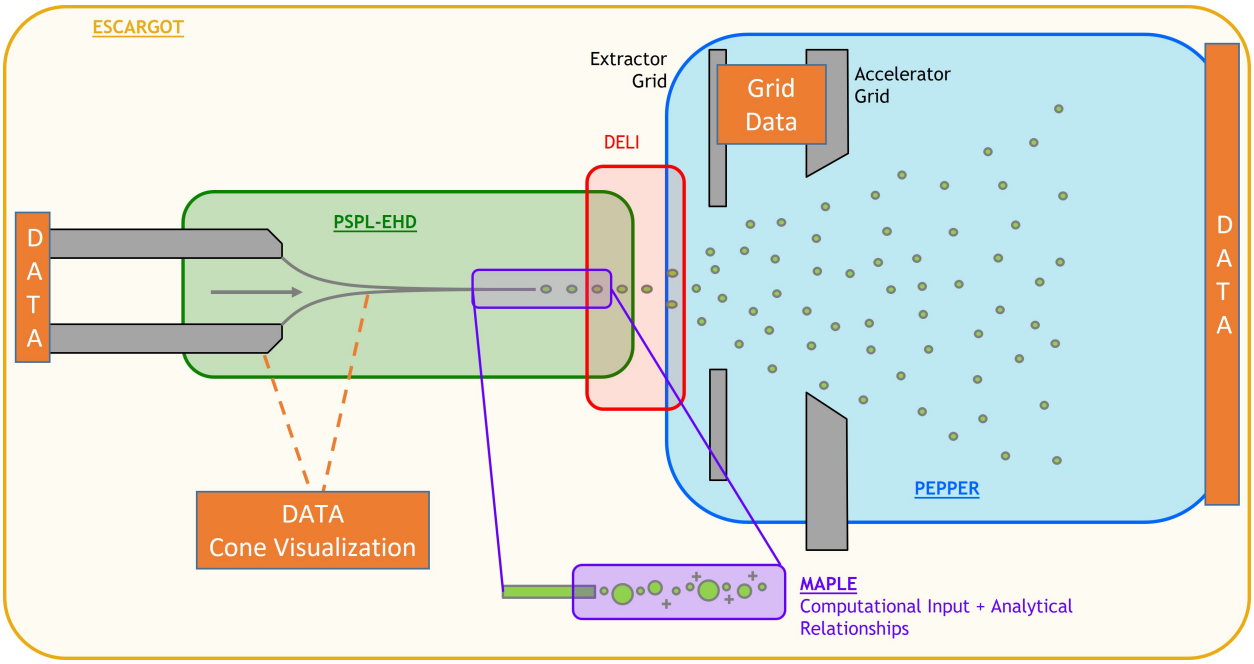

Figure 4.1: UCLA Electrospray Multi-scale/Multi-physics modelling overview.

4.1 Analytical Model Derivation

In this section, we will begin by deriving a general equation for relating measured current to the true primary impingement current. Next, we will develop a system of equations for a testing arragement of the Busek Colloid MicroNewton Thrusters (CMNT) tested at JPL.

4.1.1 Generalized Equation

To examine charge transport in an electrospray thruster testing facility, we assume a testing configuration where a beam target terminates the full extent of the thruster's plume, and is equipped with a transducer to report the captured plume current. Charge conservation serves as the basis for our model, where the current measured by a transducer must equal the sum of all current collected by and emitted from the electrode. In the idealized perspective of charge transport in electrospray thrusters, primary species are perfectly captured by any interception surfaces and no SSE occurs. Therefore, the ideal measured current at the i^{th} electrode (I_i^M) is simply equal to the plume current

intercepted by the electrode (J_i^P),

$$I_i^M = J_i^P \tag{4.1}$$

However, primary species in the plume are well above the threshold for secondary species emission (SSE), so we must consider the generation of secondary currents at each electrode [77]. Emitted currents induced by SSE (J_i^S) represent a loss of charged species from the surface, though the current's sign will depend on the charge polarity of both incoming and outgoing species. Furthermore, the secondary plume from each impinged surface will result in charge transport to upstream electrodes. The extent of charge transport between the j^{th} and i^{th} electrodes is modeled by the "dimensionless geometric factor", $\mathbb{G}_{j\to i}$. Chapter 4.2 will define $\mathbb{G}$ in detail, but for now it may be thought of as a parameter that relates charge emitted by one surface and collected by another. Accounting for emitted and collected secondary currents gives the following relationship between primary and secondary transport terms, and the measured current:

$$I_i^M = J_i^P - J_i^S + \sum_{j\in\mathbb{D}_1} \mathbb{G}_{j\to i} J_j^S, \tag{4.2}$$

where $\mathbb{D}_1$ is the set of electrodes downstream of the i^{th} electrode. SSE current is proportional to the incident primary current scaled by a yield parameter, $\gamma_i(\phi_{j-i})$, defined as the energy-dependent SSE yield of the i^{th} electrode, where ϕ_{j-i} represents the potential difference between the j^{th} and i^{th} electrodes. Since primary species may cause both positive and negative SSE, $\gamma_i(\phi_{j-i})$ consists of the sum of both yields. Furthermore, $\mathbb{G}$ is also driven by the charge polarity of emitted secondaries, so $\mathbb{G}$ must also represent both positive and negative charges.

Leaving all terms completely expanded leads to rather cumbersome expressions. To avoid too much complication, we adopt a matrix shorthand notation for the SSE yields and geometric factors:

$$\mathbf{\Gamma}_{i,j} = \left[\gamma_i^-(\phi_{j-i})\ ,\ -\gamma_i^+(\phi_{j-i})\right] \tag{4.3}$$

$$\mathbb{G}_{j\to i} = \left[\mathbb{G}^{-}_{j\to i}\ ,\ \mathbb{G}^{+}_{j\to i}\right] \tag{4.4}$$

Note the polarity of γ^{+} is due to emitted positive charges registering as negative measured current. Emitted secondary current may then be defined as:

$$J^{S}_{i} = \sum_{\pm} \mathbf{\Gamma}_{i,em} J^{P}_{i}, \tag{4.5}$$

where $\sum_{\pm}$ indicates that the resulting two-term matrix must be summed, and the *em* subscript denotes the emitter, since it is the electrode where all J^{P}_{i} originates from. Substituting equation 4.5 into equation 4.2 gives:

$$I^{M}_{i} = J^{P}_{i} - \sum_{\pm} \mathbf{\Gamma}_{i,em} J^{P}_{i} + \sum_{j\in\mathbb{D}_1} \left\langle \mathbf{\Gamma}_{i,j}, \mathbb{G}_{j\to i} \right\rangle \left(\sum_{\pm} \mathbf{\Gamma}_{j,em} J^{P}_{j}\right), \tag{4.6}$$

where the $\langle\ \rangle$ operator represents the inner product, such that

$$\left\langle \mathbf{\Gamma}_{i,j}, \mathbb{G}_{j\to i} \right\rangle = \gamma^{-}_{i}(\phi_{j-i})\mathbb{G}^{-}_{j\to i} - \gamma^{+}_{i}(\phi_{j-i})\mathbb{G}^{+}_{j\to i} \tag{4.7}$$

The least complex configuration possible for an electrospray thruster involves two electrodes: an emitter and an extractor. Many embodiments of ILIS thrusters use the simple emitter/extractor configuration [36, 54, 4, 187]. Again, the ESCARGOT model presumes the use of a beam target that both terminates the full extent of the plume, and is capable of reporting collected current. Therefore, the simplest set of electrodes that may be analyzed with ESCARGOT is $\mathbb{S} = \{\text{emitter},\ \text{extractor},\ \text{beam target}\}$.

For simple two-electrode thrusters, equation 4.6 is likely sufficient to model charge transport in an electrospray. Some electrospray thrusters, such as the CMNT, may incorporate an additional accelerator electrode to prevent electron backstreaming, similar to traditional gridded-ion thrusters [188, 31]. Furthermore, a total potential bias may be applied to the emitter and extrac-

tor to provide thrust enhancement. For example, the CMNT emitter and extractor are biased to 6 kV and 4.4 kV, respectively [31]. In more sophisticated thruster geometries, where electrodes are biased to very high voltages, it becomes necessary to consider third-order emission effects.

While secondaries are emitted with a very low temperature (< 5 eV), they will be accelerated up to primary energies by oppositely-charged electrodes in a manner similar to dynodes in electron multipliers [189]. Therefore, this dynode-like cascade must be considered to capture the possible emission of tertiary currents. Tertiary current is evaluated in the same manner as secondary currents, where $\mathbb{G}$ is used as a parameter to relate charge flux from one surface to another. Modifying equation 4.2 to include tertiary emission caused by secondaries, and collection of tertiary emission from all other electrodes gives:

$$I_i^M = J_i^P - J_i^S + \sum_{j\in\mathbb{D}_1} \sum_{\pm} \mathbb{G}_{j\to i} J_j^S - \sum_{j\in\mathbb{D}_1} J_{j\to i}^T + \sum_{k\in\mathbb{A}} \sum_{\pm} \mathbb{G}_{k\to i} \sum_{l\in\mathbb{D}_2} J_{l\to k}^T, \tag{4.8}$$

where $\mathbb{D}_2$ is the set of electrodes downstream of the l^{th} electrode, and $\mathbb{A}$ is the set of all electrodes in the thruster, excluding the i^{th} electrode, i.e. $i \notin \mathbb{A}$. Equation 4.8 essentially states that the measured current at an electrode is the aggregate of: (1) the intercepted plume current, (2) the emitted secondary current, (3) collected secondary current from all downstream electrodes, (4) emitted tertiary current due to collected secondary current, (5) and collected tertiary current from all upstream and downstream electrodes. Figure 4.2 provides a illustration of the behavior described by equation 4.8. A major takeaway from equations 4.2 and 4.8 is that the currents measured at different electrodes in a thruster do not reflect the actual impingement current due to the primary species in the plume.

Where dynode electron multipliers are tailored to provide a current gain by exploiting the high electron emission yield of oxide coatings, electrospray thruster SSE yields are less than unity, so current attenuates with each subsequent impact. Owing to the attenuating effect of SSE in electrosprays, we neglect higher-order emission.

Emitted tertiary current is defined as:

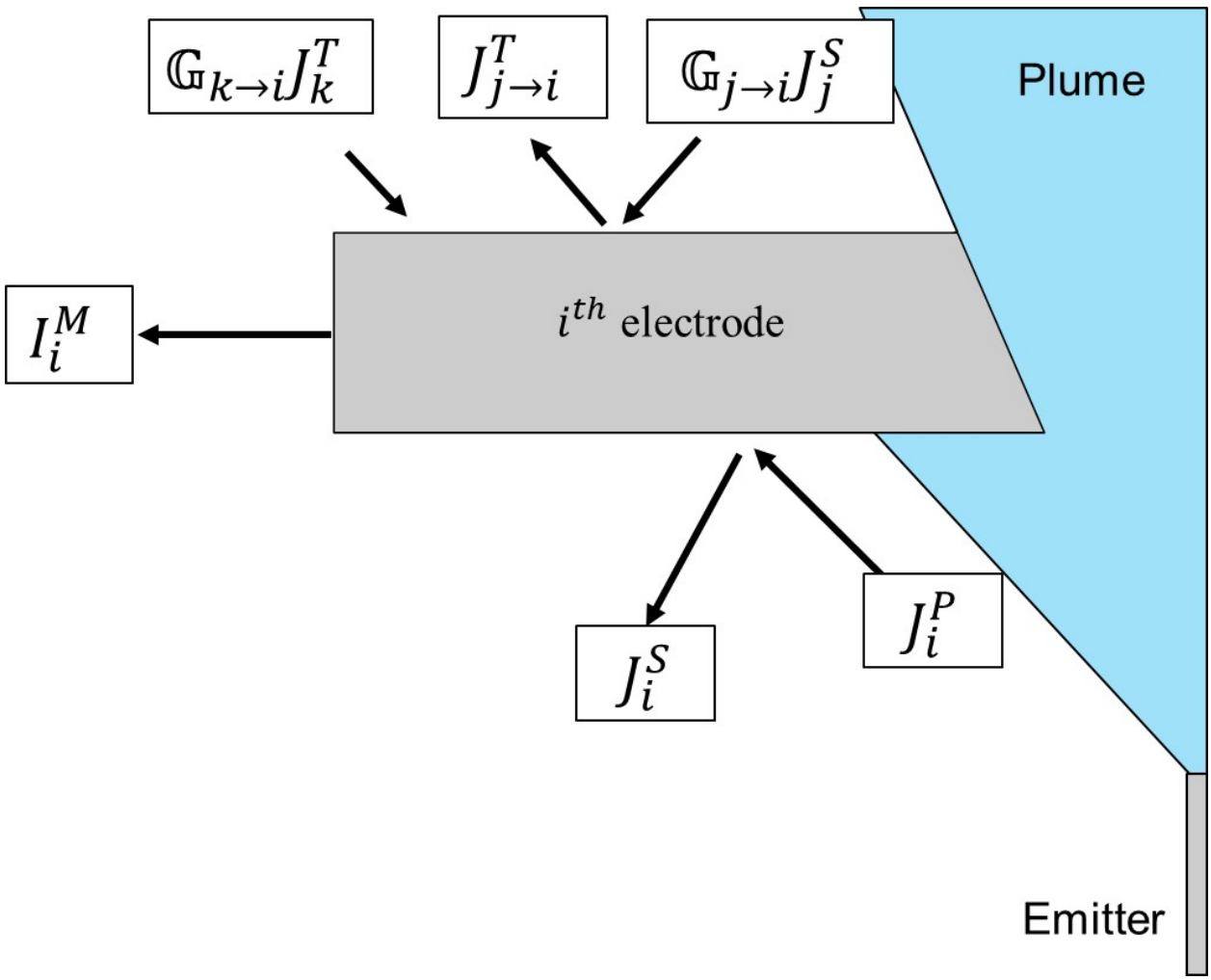

Figure 4.2: A graphic depicting the different currents collected and emitted by the i^{th} electrode.

$$J^T_{j\to i} = \langle \mathbf{\Gamma}_{i,j}, \mathbb{G}_{j\to i}\rangle J^S_j = \langle \mathbf{\Gamma}_{i,j}, \mathbb{G}_{j\to i}\rangle (\sum_{\pm} \mathbf{\Gamma}_{j,em} J^P_j) \tag{4.9}$$

The governing equation for charge transport in a complex electrospray thruster configuration (e.g. the Busek CMNT) can be obtained by substituting equations 4.5 and 4.9 into equation 4.8:

$$\begin{aligned} I^M_i = {} & J^P_i - \sum_{\pm} \mathbf{\Gamma}_{i,em} J^P_i \\ & + \sum_{j\in\mathbb{D}_1} \langle \mathbf{\Gamma}_{j,em}, \mathbb{G}_{j\to i}\rangle J^P_j \\ & - \sum_{j\in\mathbb{D}_1} \langle \mathbf{\Gamma}_{i,j}, \mathbb{G}_{j\to i}\rangle \left(\sum_{\pm} \mathbf{\Gamma}_{j,em} J^P_j \right) \\ & + \sum_{k\in\mathbb{A}} \langle \mathbf{\Gamma}_{k,em}, \mathbb{G}_{k\to i}\rangle \sum_{l\in\mathbb{D}_2} \langle \mathbf{\Gamma}_{k,l}, \mathbb{G}_{l\to k}\rangle J^P_k \end{aligned} \tag{4.10}$$

Both equation 4.6 and equation 4.10 give measured current as a function of geometric factor ($\mathbb{G}$), SSE yield (γ), and collected primary current of the n^{th} electrode (J^P_n). In the following sections, we will show how $\mathbb{G}$ may be obtained via numerical simulations, and γ may be obtained experimentally. With both $\mathbb{G}$ and γ defined, the only remaining unknowns are the J^P_n terms. If the thruster testing facility is built in a manner that fully terminates the plume and allows for complete measurement of the plume current, it's possible to construct a system of linear equations from the derived governing equations that provide a solution for the actual primary impingement current on each electrode.

4.1.2 Colloid MicroNewton Thruster (CMNT) Charge Transport Equations

In this section, we derive the system of equations for an electrospray thruster testing configuration as an example for how to apply the governing equations defined above. The objective of the present study is to examine SSE charge transport in the CMNT to better predict lifetime. Accordingly, the

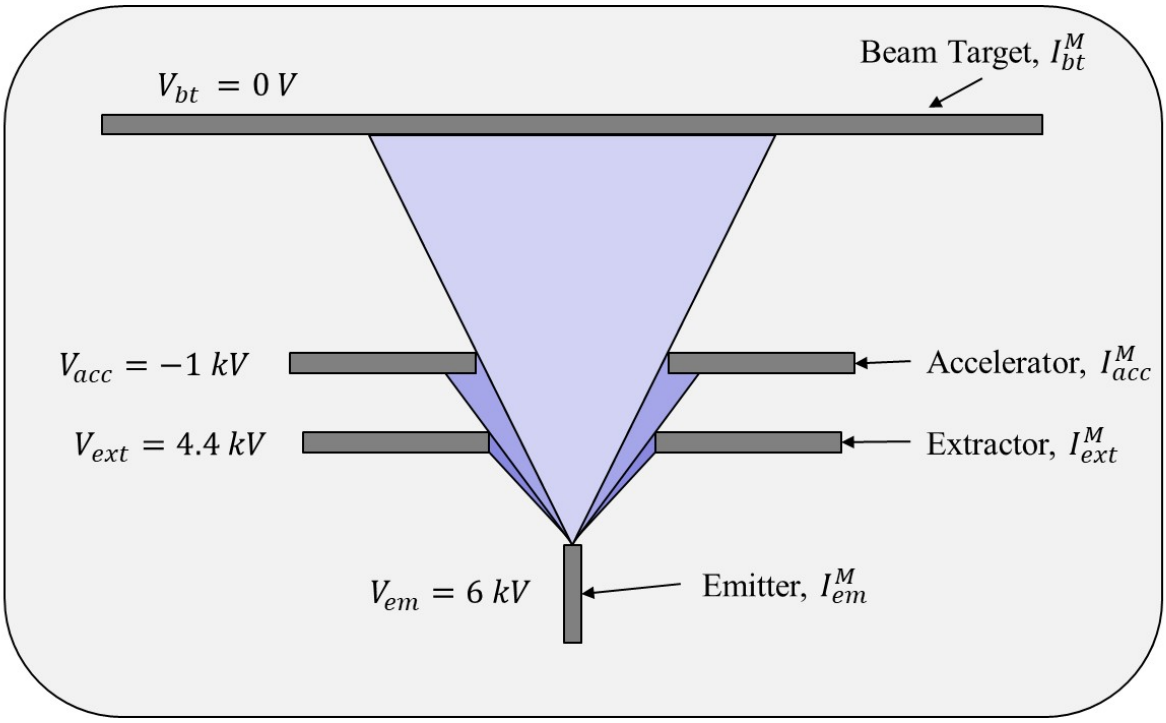

Figure 4.3: System diagram of the Busek CMNT testing configuration in the JPL MicroPropulsion Laboratory facility.

testing configuration discussed herein consists of a single-emitter embodiment of the CMNT that was studied at NASA JPL, and a simplified representation of the beam target.

A system diagram of the thruster geometry and associated potential biases are shown in Figure 4.3. The emitter, extractor, accelerator, and beam target electrodes will be denoted with the respective subscripts *em*, *ex*, *ac*, and *bt*. The ordered set of electrodes used to interpret the summations in the governing equations is $\mathbb{S} = \{em,\ ex,\ ac,\ bt\}$.

Using equation 4.8, we derive the current for each electrode:

$$
\begin{aligned}
I^M_{em} = & J^P_{total} + J^T_{ex\to em} + J^T_{ac\to em} + J^T_{bt\to em} \\
& - \sum_{\pm} \mathbb{G}_{ex\to em} \left(J^S_{ex} + J^T_{ac\to ex} + J^T_{bt\to ex} \right) \\
& - \sum_{\pm} \mathbb{G}_{ac\to em} \left(J^S_{ac} + J^T_{bt\to ac} \right) - \sum_{\pm} \mathbb{G}_{bt\to em} \left(J^S_{bt} \right)
\end{aligned} \tag{4.11}
$$

$$
\begin{aligned}
I^M_{ex} = & - J^P_{ex} - J^S_{ex} - (J^T_{ac\to ex} + J^T_{bt\to ex}) \\
& + \sum_{\pm} \mathbb{G}_{em\to ex} (J^T_{ex\to em} + J^T_{ac\to em} + J^T_{bt\to em}) \\
& + \sum_{\pm} \mathbb{G}_{ac\to ex} (J^S_{ac} + J^T_{bt\to ac}) + \sum_{\pm} \mathbb{G}_{bt\to ex} (J^S_{bt})
\end{aligned} \tag{4.12}
$$

$$
\begin{aligned}
I^M_{ac} = & - J^P_{ac} - J^S_{ac} - J^T_{bt\to ac} \\
& + \sum_{\pm} \mathbb{G}_{em\to ac} (J^T_{ex\to em} + J^T_{ac\to em} + J^T_{bt\to em}) \\
& + \sum_{\pm} \mathbb{G}_{ex\to ac} (J^T_{ac\to ex} + J^T_{bt\to ex}) + \sum_{\pm} \mathbb{G}_{bt\to ac} (J^S_{bt})
\end{aligned} \tag{4.13}
$$

$$
\begin{aligned}
I^M_{bt} = & - J^P_{bt} - J^S_{bt} \\
& + \sum_{\pm} \mathbb{G}_{em\to bt} (J^T_{ex\to em} + J^T_{ac\to em} + J^T_{bt\to em}) \\
& + \sum_{\pm} \mathbb{G}_{ex\to bt} (J^T_{ac\to ex} + J^T_{bt\to ex}) + \sum_{\pm} \mathbb{G}_{ac\to bt} (J^T_{bt\to ac})
\end{aligned} \tag{4.14}
$$

Expansion of equations 4.11 through 4.14 is facilitated by the use of Matlab's Symbolic Math Toolbox to accurately and rapidly perform symbolic computation. Equations 4.5 and 4.9 are sub-

stituted into equations 4.11 through 4.14 and all coefficients of J^P are collected:

$$
\begin{aligned}
I^M_{bt} &= -J^P_{total} \\
&+ J^P_{ex}\Bigg(\langle \mathbf{\Gamma}_{ex,em}, \mathbb{G}_{ex\to em}\rangle \sum_{\pm} \mathbf{\Gamma}_{em,ex} - \langle \mathbf{\Gamma}_{ex,em}, \mathbb{G}_{ex\to em}\rangle\Bigg) \\
&+ J^P_{ac}\Bigg(\langle \mathbf{\Gamma}_{ac,em}, \mathbb{G}_{ac\to em}\rangle \sum_{\pm} \mathbf{\Gamma}_{em,ac} - \langle \mathbf{\Gamma}_{ac,em}, \mathbb{G}_{ac\to em}\rangle \\
&\qquad - \langle \mathbf{\Gamma}_{ac,em}, \mathbb{G}_{ac\to ex}\rangle \langle \mathbf{\Gamma}_{ex,ac}, \mathbb{G}_{ex\to em}\rangle\Bigg) \\
&+ J^P_{bt}\Bigg(\langle \mathbf{\Gamma}_{bt,em}, \mathbb{G}_{bt\to em}\rangle \sum_{\pm} \mathbf{\Gamma}_{em,bt} - \langle \mathbf{\Gamma}_{bt,em}, \mathbb{G}_{bt\to em}\rangle \\
&\qquad - \langle \mathbf{\Gamma}_{bt,em}, \mathbb{G}_{bt\to ac}\rangle \langle \mathbf{\Gamma}_{ac,bt}, \mathbb{G}_{ac\to em}\rangle \\
&\qquad\qquad - \langle \mathbf{\Gamma}_{bt,em}, \mathbb{G}_{bt\to ex}\rangle \langle \mathbf{\Gamma}_{ex,bt}, \mathbb{G}_{ex\to em}\rangle\Bigg)
\end{aligned}
\tag{4.15}
$$

$$
\begin{aligned}
I^M_{ex} &= J^P_{ex}\Bigg(\langle \mathbf{\Gamma}_{em,ex}, \mathbb{G}_{em\to ex}\rangle \langle \mathbf{\Gamma}_{ex,em}, \mathbb{G}_{ex\to em}\rangle - \sum_{\pm} \mathbf{\Gamma}_{ex,em} - 1\Bigg) \\
&+ J^P_{ac}\Bigg(\langle \mathbf{\Gamma}_{ac,em}, \mathbb{G}_{ac\to ex}\rangle - \langle \mathbf{\Gamma}_{ac,em}, \mathbb{G}_{ac\to ex}\rangle \sum_{\pm} \mathbf{\Gamma}_{ex,ac} \\
&\qquad + \langle \mathbf{\Gamma}_{ac,em}, \mathbb{G}_{ac\to em}\rangle \langle \mathbf{\Gamma}_{em,ac}, \mathbb{G}_{em\to ex}\rangle\Bigg) \\
&+ J^P_{bt}\Bigg(\langle \mathbf{\Gamma}_{bt,em}, \mathbb{G}_{bt\to ex}\rangle - \langle \mathbf{\Gamma}_{bt,em}, \mathbb{G}_{bt\to ex}\rangle \sum_{\pm} \mathbf{\Gamma}_{ex,bt} \\
&\qquad + \langle \mathbf{\Gamma}_{bt,em}, \mathbb{G}_{bt\to em}\rangle \langle \mathbf{\Gamma}_{em,bt}, \mathbb{G}_{em\to ex}\rangle \\
&\qquad\qquad + \langle \mathbf{\Gamma}_{bt,em}, \mathbb{G}_{bt\to ac}\rangle \langle \mathbf{\Gamma}_{ac,bt}, \mathbb{G}_{ac\to ex}\rangle\Bigg)
\end{aligned}
\tag{4.16}
$$

$$
\begin{aligned}
I^M_{ac} = J^P_{ex}\Bigg(& \langle \mathbf{\Gamma}_{ex,em}, \mathbb{G}_{em\to ac}\rangle \langle \mathbf{\Gamma}_{em,ex}, \mathbb{G}_{ex\to em}\rangle \Bigg) \\
& + J^P_{ac}\Bigg(\langle \mathbf{\Gamma}_{ac,em}, \mathbb{G}_{ac\to em}\rangle \langle \mathbf{\Gamma}_{em,ac}, \mathbb{G}_{em\to ac}\rangle \\
& \quad + \langle \mathbf{\Gamma}_{ac,em}, \mathbb{G}_{ac\to ex}\rangle \langle \mathbf{\Gamma}_{ex,ac}, \mathbb{G}_{ex\to ac}\rangle \\
& \quad - \mathbf{\Gamma}_{ac,em} - 1 \Bigg) \\
& + J^P_{bt}\Bigg(\langle \mathbf{\Gamma}_{bt,em}, \mathbb{G}_{bt\to ac}\rangle - \langle \mathbf{\Gamma}_{bt,em}, \mathbb{G}_{bt\to ac}\rangle \sum_{\pm} \mathbf{\Gamma}_{ac,bt} \\
& \quad + \langle \mathbf{\Gamma}_{bt,em}, \mathbb{G}_{bt\to em}\rangle \langle \mathbf{\Gamma}_{em,bt}, \mathbb{G}_{em\to ac}\rangle \\
& \quad + \langle \mathbf{\Gamma}_{bt,em}, \mathbb{G}_{bt\to ex}\rangle \langle \mathbf{\Gamma}_{ex,bt}, \mathbb{G}_{ex\to ac}\rangle \Bigg)
\end{aligned}
\tag{4.17}
$$

$$
\begin{aligned}
I^M_{bt} = J^P_{ex}\Bigg(& \langle \mathbf{\Gamma}_{ex,em}\mathbb{G}_{em\to bt}\rangle \langle \mathbf{\Gamma}_{em,ex}, \mathbb{G}_{ex\to em}\rangle \Bigg) \\
& + J^P_{ac}\Bigg(\langle \mathbf{\Gamma}_{em,ac}, \mathbb{G}_{ac\to em}\rangle \langle \mathbf{\Gamma}_{ac,em}, \mathbb{G}_{em\to bt}\rangle \\
& \quad + \langle \mathbf{\Gamma}_{ac,em}, \mathbb{G}_{ac\to ex}\rangle \langle \mathbf{\Gamma}_{ex,ac}, \mathbb{G}_{ex\to bt}\rangle \Bigg) \\
& + J^P_{bt}\Bigg(\langle \mathbf{\Gamma}_{bt,em}\mathbb{G}_{bt\to em}\rangle \langle \mathbf{\Gamma}_{em,bt}\mathbb{G}_{em\to bt}\rangle \\
& \quad + \langle \mathbf{\Gamma}_{bt,em}, \mathbb{G}_{bt\to ac}\rangle \langle \mathbf{\Gamma}_{ac,bt}, \mathbb{G}_{ac\to bt}\rangle \\
& \quad + \langle \mathbf{\Gamma}_{bt,em}, \mathbb{G}_{bt\to ex}\rangle \langle \mathbf{\Gamma}_{ex,bt}, \mathbb{G}_{ex\to bt}\rangle - \mathbf{\Gamma}_{bt,em} + 1 \Bigg)
\end{aligned}
\tag{4.18}
$$

With the system of equations fully defined, the coefficients of the J^P terms may be used to define define elements in a coefficient matrix. Each element is defined as:

$$
\begin{aligned}
em_1 &= -1 \\
em_2 &= \langle \mathbf{\Gamma}_{ex,em}, \mathbb{G}_{ex\to em}\rangle \sum_{\pm} \mathbf{\Gamma}_{em,ex} - \langle \mathbf{\Gamma}_{ex,em}, \mathbb{G}_{ex\to em}\rangle \\
em_3 &= \langle \mathbf{\Gamma}_{ac,em}, \mathbb{G}_{ac\to em}\rangle \sum_{\pm} \mathbf{\Gamma}_{em,ac} - \langle \mathbf{\Gamma}_{ac,em}, \mathbb{G}_{ac\to em}\rangle \\
&\quad - \langle \mathbf{\Gamma}_{ac,em}, \mathbb{G}_{ac\to ex}\rangle \langle \mathbf{\Gamma}_{ex,ac}, \mathbb{G}_{ex\to em}\rangle \\
em_4 &= \langle \mathbf{\Gamma}_{bt,em}, \mathbb{G}_{bt\to em}\rangle \sum_{\pm} \mathbf{\Gamma}_{em,bt} - \langle \mathbf{\Gamma}_{bt,em}, \mathbb{G}_{bt\to em}\rangle \\
&\quad - \langle \mathbf{\Gamma}_{bt,em}, \mathbb{G}_{bt\to ac}\rangle \langle \mathbf{\Gamma}_{ac,bt}, \mathbb{G}_{ac\to em}\rangle \\
&\quad - \langle \mathbf{\Gamma}_{bt,em}, \mathbb{G}_{bt\to ex}\rangle \langle \mathbf{\Gamma}_{ex,bt}, \mathbb{G}_{ex\to em}\rangle
\end{aligned} \tag{4.19}
$$

$$
\begin{aligned}
ex_1 &= 0 \\
ex_2 &= \langle \mathbf{\Gamma}_{em,ex}, \mathbb{G}_{em\to ex}\rangle \langle \mathbf{\Gamma}_{ex,em}, \mathbb{G}_{ex\to em}\rangle - \sum_{\pm} \mathbf{\Gamma}_{ex,em} - 1) \\
ex_3 &= \langle \mathbf{\Gamma}_{ac,em}, \mathbb{G}_{ac\to ex}\rangle - \langle \mathbf{\Gamma}_{ac,em}, \mathbb{G}_{ac\to ex}\rangle \sum_{\pm} \mathbf{\Gamma}_{ex,ac} \\
&\quad + \langle \mathbf{\Gamma}_{ac,em}, \mathbb{G}_{ac\to em}\rangle \langle \mathbf{\Gamma}_{em,ac}, \mathbb{G}_{em\to ex}\rangle \\
ex_4 &= \langle \mathbf{\Gamma}_{bt,em}, \mathbb{G}_{bt\to ex}\rangle - \langle \mathbf{\Gamma}_{bt,em}, \mathbb{G}_{bt\to ex}\rangle \sum_{\pm} \mathbf{\Gamma}_{ex,bt} \\
&\quad + \langle \mathbf{\Gamma}_{bt,em}, \mathbb{G}_{bt\to em}\rangle \langle \mathbf{\Gamma}_{em,bt}, \mathbb{G}_{em\to ex}\rangle \\
&\quad + \langle \mathbf{\Gamma}_{bt,em}, \mathbb{G}_{bt\to ac}\rangle \langle \mathbf{\Gamma}_{ac,bt}, \mathbb{G}_{ac\to ex}\rangle
\end{aligned} \tag{4.20}
$$

$$
\begin{aligned}
ac_1 &= 0 \\
ac_2 &= \langle \mathbf{\Gamma}_{ex,em}, \mathbb{G}_{em\to ac} \rangle \langle \mathbf{\Gamma}_{em,ex}, \mathbb{G}_{ex\to em} \rangle \\
ac_3 &= \langle \mathbf{\Gamma}_{ac,em}, \mathbb{G}_{ac\to em} \rangle \langle \mathbf{\Gamma}_{em,ac}, \mathbb{G}_{em\to ac} \rangle \\
&\quad + \langle \mathbf{\Gamma}_{ac,em}, \mathbb{G}_{ac\to ex} \rangle \langle \mathbf{\Gamma}_{ex,ac}, \mathbb{G}_{ex\to ac} \rangle \\
&\quad - \mathbf{\Gamma}_{ac,em} - 1) \\
ac_4 &= \langle \mathbf{\Gamma}_{bt,em}, \mathbb{G}_{bt\to ac} \rangle - \langle \mathbf{\Gamma}_{bt,em}, \mathbb{G}_{bt\to ac} \rangle \sum_{\pm} \mathbf{\Gamma}_{ac,bt} \\
&\quad + \langle \mathbf{\Gamma}_{bt,em}, \mathbb{G}_{bt\to em} \rangle \langle \mathbf{\Gamma}_{em,bt}, \mathbb{G}_{em\to ac} \rangle \\
&\quad + \langle \mathbf{\Gamma}_{bt,em}, \mathbb{G}_{bt\to ex} \rangle \langle \mathbf{\Gamma}_{ex,bt}, \mathbb{G}_{ex\to ac} \rangle
\end{aligned} \tag{4.21}
$$

$$
\begin{aligned}
bt_1 &= 0 \\
bt_2 &= \langle \mathbf{\Gamma}_{ex,em} \mathbb{G}_{em\to bt} \rangle \langle \mathbf{\Gamma}_{em,ex}, \mathbb{G}_{ex\to em} \rangle \\
bt_3 &= \langle \mathbf{\Gamma}_{em,ac}, \mathbb{G}_{ac\to em} \rangle \langle \mathbf{\Gamma}_{ac,em}, \mathbb{G}_{em\to bt} \rangle \\
&\quad + \langle \mathbf{\Gamma}_{ac,em}, \mathbb{G}_{ac\to ex} \rangle \langle \mathbf{\Gamma}_{ex,ac}, \mathbb{G}_{ex\to bt} \rangle \\
bt_4 &= \langle \mathbf{\Gamma}_{bt,em} \mathbb{G}_{bt\to em} \rangle \langle \mathbf{\Gamma}_{em,bt} \mathbb{G}_{em\to bt} \rangle \\
&\quad + \langle \mathbf{\Gamma}_{bt,em}, \mathbb{G}_{bt\to ac} \rangle \langle \mathbf{\Gamma}_{ac,bt}, \mathbb{G}_{ac\to bt} \rangle \\
&\quad + \langle \mathbf{\Gamma}_{bt,em}, \mathbb{G}_{bt\to ex} \rangle \langle \mathbf{\Gamma}_{ex,bt}, \mathbb{G}_{ex\to bt} \rangle - \mathbf{\Gamma}_{bt,em} + 1
\end{aligned} \tag{4.22}
$$

Using the coefficients defined in 4.19 through 4.22, the system of equations may be expressed in $\mathbf{X}J^P = I^M$ matrix form:

$$\begin{bmatrix} -1 & em_2 & em_3 & em_4 \\ 0 & ex_2 & ex_3 & ex_4 \\ 0 & ac_2 & ac_3 & ac_4 \\ 0 & bt_2 & bt_3 & bt_4 \end{bmatrix} \begin{bmatrix} J^P_{total} \\ J^P_{ex} \\ J^P_{ac} \\ J^P_{bt} \end{bmatrix} = \begin{bmatrix} I^M_{em} \\ I^M_{ex} \\ I^M_{ac} \\ I^M_{bt} \end{bmatrix} \tag{4.23}$$

The left matrix, $\mathbf{X}$ consists of the $\mathbb{G}$ and γ terms that are obtained by numerical simulation and experiments, respectively. With the system of equations in matrix form, we now have a tool for converting between experimentally obtained measurements and computational modelling results. The next two sections will describe how to obtain the values for $\mathbb{G}$ and γ.

4.2 Geometric Factors

The "geometric factor" is a calibration parameter used to convert counts on a detector to differential fluxes and phase space densities [190, 191]. Mathematical models for the geometric factor have been derived in prior studies aimed at providing precision calibration for scientific instruments aboard spacecraft [192, 193, 190, 191, 194]. A presupposed response function, $\mathbb{R}(v)$, describes the probability of a particle entering an instrument being counted by the detector, and is nonzero in a limited region of velocity space. Given a distribution of particle energies and angles of incidence, a geometric factor, $[GF]$, is defined as the integral of $\mathbb{R}(v)$ over all phase space. Fundamentally, the geometric factor quantifies charge flux from one surface to another – a scenario that is identical to our concerns with secondary species transport. In this section, we will show that using a few assumptions, the geometric factor derivations presented in prior studies may be modified for our purposes. We will then discuss the numerical simulation methodology used to determine the dimensionless geometric factors.

4.2.1 Mathematical Formalism

Kessel et al. [192] derive a mathematical formalism for determining geometric factor using Faraday cup measurements of a calibrated ion beam. However, it is also possible to utilize their formalism to obtain a geometric factor with numerical particle tracking simulations [195, 191, 190]. Our approach is a slight modification of those reported in literature due to the differences in both the physical phenomena of interest, and the end application of the geometric factor. Kessel et al. [192] define $[GF]$ as

$$[GF] \equiv \int (\mathbf{u}' \cdot \mathbf{A}) \mathbb{R}(v_0 \mathbf{u}') d\mathbf{u}', \tag{4.24}$$

where $\mathbf{u}'$ is the velocity unit vector, v_0 is the center of the energy baseband, and $\mathbf{A}$ is the area vector of the detector aperture with direction along the instrument's inward normal. The derivation by Kessel et al. [192] arrives at a summation form of geometric factor calibration:

$$[GF] = \frac{eA_{FC}\Delta u' \Delta\theta \Delta\phi'}{T_{int}} \sum_l \sum_m \sum_n N/I \tag{4.25}$$

where e is elementary charge, A_{FC} is Faraday Cup detector area, $\Delta\mathbf{u}'$ and $\Delta\theta$ are the calibration beam velocity and angular widths, $\Delta\phi$ is azimuthal angle step, T_{int} is integration time, N is the particle count on the detector, I is calibration beam current, and the lmn subscripts indicate summation over polar angle, azimuthal angle, and velocity. Due to the $(\mathbf{u}' \cdot \mathbf{A})$ term in its definition, $[GF]$ naturally accounts for the detector's geometry, giving units $\mathrm{m}^2\mathrm{sr}$.

Rather than interpreting detector counts, the objective of our analysis is to determine the extent of current flux between two surfaces. Recognizing the similarity in geometry and mathematical formalism required to describe both problems, all that is necessary is a change in context and redefinition of several variables to apply the derived geometric factor to the secondary species transport problem.

The electrostatic analyzer calibration problem posed by Kessel et al. [192] consists of a cali-

brated ion beam introduced via an instrument aperture as an inlet, and a Faraday cup as an outlet for particles. For the secondary species transport problem, we instead have an impinged electrode surface as an inlet, and a collecting electrode surface as an outlet. As noted earlier, $[GF]$ naturally accounts for the inlet area, but we must redefine A_{FC} as outlet surface area A_{out} for our problem. Instead of solving the time integral to a fixed integration period, we leave the integral indefinite and solve to replace T_{int} with t. Next, we redefine the calibrated ion beam current, I, as the inlet current from the i^{th} electrode, I_i. The number of secondary particles emitted from the i^{th} surface is then defined as $M_i = I_i t/e$. The number of collected particles on the Faraday cup, N, is redefined to be the number of collected particles on the j^{th} outlet surface, N_j. We then rearrange equation 4.25 to make the expression entirely dimensionless:

$$\frac{[GF]}{A_{out}\Delta u'\Delta\theta\Delta\phi'} = \sum_l \sum_m \sum_n \frac{eN_j/t}{eM_i/t} \tag{4.26}$$

The dimensionless geometric factor relating the i^{th} and j^{th} electrode is then defined as $\mathbb{G}_{j\to i} = [GF]/(A_{out}\Delta u'\Delta\theta\Delta\phi')$, which results in the following expression:

$$\mathbb{G}_{j\to i} = \sum_l \sum_m \sum_n \frac{N_j}{M_i} \tag{4.27}$$

When determining the geometric factor using particle tracking simulations, the azimuthal step, polar step, and particle energies are parametrically swept, providing a locus of solutions [195]. Geometric factor is then obtained using equation 4.25 and summing the particle tracking solutions. The energy distribution function (EDF) of SSE is reasonably well defined for the plume of the CMNT (see Chapter 3.2.4), where the EDF can be approximated as Maxwellian with a temperature of $\sim$1 eV. Using COMSOL Multiphysics® as the simulation suite, the inlet parameters may be set to diffusely emit particles from a surface with a user-defined thermal velocity. Therefore, with a sufficiently high particle count, the summations in equation 4.27 are satisfied by essentially simulating all conditions simultaneously. Equation 4.27 can then be further simplified to

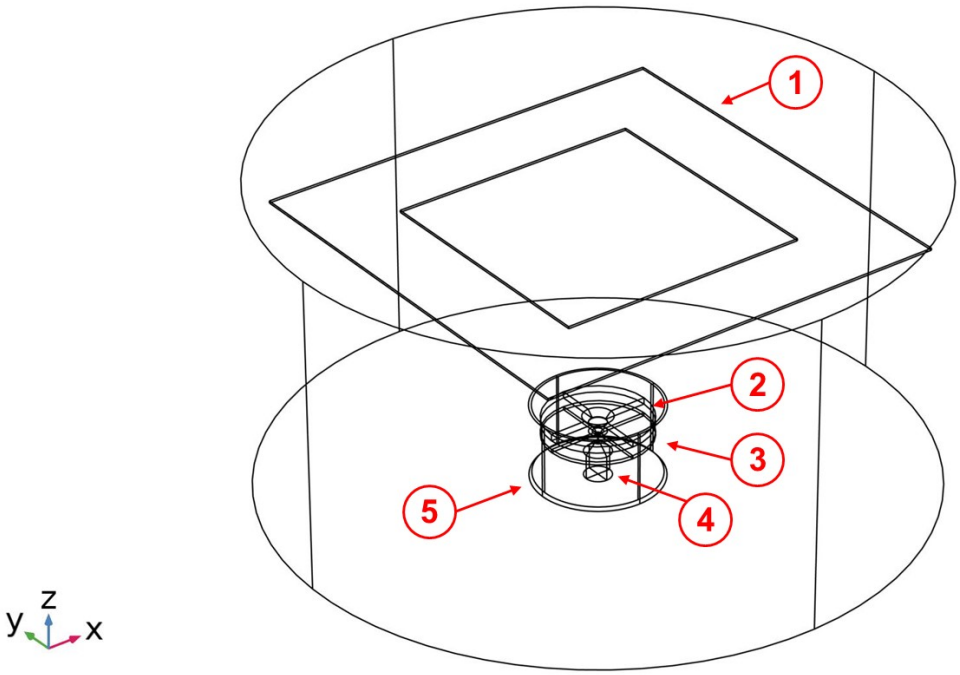

Figure 4.4: Wireframe rendering of the CMNT and Beam Target geometries modelled in COMSOL. Numbered callouts: (1) Beam target, (2) Accelerator, (3) Extractor, (4) Emitter, (5) Grounded thruster enclosure.

$$\mathbb{G}_{j\to i} = \frac{N_j}{M_i}, \tag{4.28}$$

where M_i are the number of particles released by the inlet surface, and N_j are the number of particles collected by an outlet surface. Expression 4.28 represents the definition of dimensionless geometric factor used in the ESCARGOT model.

4.2.2 Numerical Simulation Method

To model the dimensionless geometric factors, the thruster and testing facility geometries must be simulated using particle tracking software. Geometric factors are commonly obtained using commercial ion optics software, such as SIMION® [195, 194, 190]. For the present study, COMSOL

Multiphysics® was used to simulate particle trajectories. A 3D model of the CMNT and beam target used in the testing campaigns at JPL were constructed in the COMSOL environment. Figure 4.4 shows an isometric view of the thruster and beam target. The first step of the numerical study is conducting an electrostatics simulation. COMSOL's AC/DC Module was used to perform electrostatics simulations and obtain a solution for the electric field in the domain. COMSOL takes voltages assigned to the boundaries, and solves the Laplace equation to obtain potentials and fields throughout the simulation domain. All surfaces were considered conductors, except for the domain boundary, which was assigned a zero-charge boundary condition.

COMSOL uses the electrostatics solutions from its AC/DC Module to evaluate forces acting on particles with its Particle Tracing Module. Within the Particle Tracing Module, the release feature, particle counter features, and particle properties must be assigned. The "release feature" is the surface where particles that will be tracked by the simulation are introduced into the domain. The "particle counter features" are outlet surfaces that will catch and count particles.

The procedure for obtaining geometric factor involves running the simulation several times, where each simulation run assigns a different electrode surface as the inlet. All remaining surfaces are assigned as outlet surfaces, which instructs COMSOL to track statistics of incident particles. Using this method, it's possible to obtain several geometric factors with a single simulation run. After the simulations are complete, we may select different results to be tabulated. The "transmission probability," or "alpha" is ratio of the number of collected particles to the number of particles released at the inlet. Therefore, the transmission probability evaluated by COMSOL directly provides values for $\mathbb{G}$.

Since SSE consists of many different mechanisms, the resulting constituents will consist of a polydisperse population of particles (e.g. electrons, atomic ions, molecular ions, etc). Ostensibly, it is necessary to simulate a geometric factor for each specific charge species. However, the applied electrode biases are incredibly high ($-1\,\mathrm{kV}$ to $6\,\mathrm{kV}$) and emitted secondaries have very low energy ($<5\,\mathrm{eV}$) [196]. Owing to the large discrepancy between emitted species energy and electrode bias, the trajectories are insensitive to the particle's specific charge. As an example, a sensitivity

Table 4.1: Results of study examining geometric factor sensitivity particle mass

Particle	Mass	$\mathbb{G}_{bt\to ac}$
Electron	9.11×10^{-31} kg	0.14875
Proton	1.67×10^{-27} kg	0.14869
$[EMI]^+$	1.85×10^{-25} kg	0.14866
[EMI]Im Cluster	1.85×10^{-22} kg	0.14864

Table 4.2: Results of a numerical simulation campaign to determine geometric factors for all electrode combinations in the Busek CMNT testing arrangement at JPL. Each cell in the table represents $\mathbb{G}_{i\to j}$, where the rows denote the i^{th} electrode and the columns denote the j^{th} electrode. $\mathbb{G}_{i\to j}$ values were obtained for both positive and negative species.

		j^{th} Electrode							
		Positive Species				Negative Species			
		em	*ex*	*ac*	*bt*	*em*	*ex*	*ac*	*bt*
i^{th} Electrode	*em*	0	0.3449	0	0	0	0	0	0
	ex	0	0	0.05238	0.3137	0.9997	0	0	0
	ac	0	0	0	0	0.0115	0.4852	0	0.4150
	bt	0	0	0.22272	0	0	0	0	0

study was conducted where the mass of emitted species was varied to simulate an electron, proton, $[EMI]^+$ cation, and 1000-unit cluster of [EMI]Im. Of any other electrodes in the system, the beam target and accelerator have the greatest distance and lowest potential difference between them, making $\mathbb{G}_{bt\to ac}$ the most susceptible to specific charge variation. Table 4.1 shows the results of the mass sensitivity study, which indicates an overall insensitivity of $\mathbb{G}$ to specific charge.

The particle property that most significantly impacts the geometric factor is charge polarity. For instance, the accelerator's -1 kV bias will attract any positive species emitted from other electrodes, but will repel all negative species. Subsequently, we simulate both positive and negative SSE emission from each surface to fully define the geometric factors. Since the Busek CMNT uses

[EMI]Im as a propellant, positive species are assigned the mass of an $[EMI]^+$ cation, and negative species are assigned the mass of an Im^- anion in our simulations.

A numerical simulation campaign was conducted to determine the full set of $\mathbb{G}_{i\to j}$ for JPL's CMNT and beam target arrangement. The geometric factor results are shown in Table 4.2. A key takeaway from the simulation campaign is that for many cases, $\mathbb{G}_{i\to j}$ is zero. In most instances, the null value for $\mathbb{G}_{i\to j}$ is explained by the self-collection of opposite-charge species. For example, positive particles released from the negatively-biased accelerator's surface are entirely suppressed, resulting in $\mathbb{G}_{ac\to j} = 0$ for all j.

4.3 SSE Yields

With the governing equations derived analytically, and the geometric factors obtained numerically, the final horseman of this model-pocalypse is the SSE yield values. The SSE yield is defined as the number of emitted secondary charges per incident primary charge. As discussed in Chapter 3.2, the aforementioned SSE Probe may also be used to obtain both positive and negative SSE yields. Since I^S_-, I^S_+, and I^P are obtained with selective secondary species suppression, SSE yields can be determined by dividing equations 3.5 by equation 3.6:

$$\begin{aligned} \gamma_- &= \frac{I^S_-}{I^P} \\ \gamma_+ &= \frac{I^S_+}{I^P}, \end{aligned} \tag{4.29}$$

where γ_- is the negative species yield, and γ_+ is the positive species yield. It is worth emphasizing that the yields calculated by this method represent the aggregate charge yields of many simultaneous SSE processes occurring at the surface.

The collector in the SSE Probe described in Chapter 3.2.2 is comprised of a sample of porous stainless steel frit used to fabricate the CMNT extractor and accelerator electrodes, which allows

use of the SSE yield measurements to examine inter-electrode current transport in the thruster. All probe materials were cleaned in a two-stage ultrasonic bath beginning with acetone, and ending with isopropyl alcohol. Surface preparation is important because each distinct surface impact phenomenon encompassed by the term "SSE" is heavily dependent on surface state. Ionic liquid electrosprays are unique in that the emitted species should condense on any impinged surfaces, and so SSE phenomena should present a time-varying response due to changing surface morphology.

Ionic liquid electrosprays are unique in that the emitted species should condense on any impinged surfaces, and so SSE phenomena should present a time-varying response due to the accumulation of a film. However, the spatially-dependent onset of shock-induced desorption suggests that any collected propellant may be desorbed as the probe traverses across the center of the plume. The circumstances of surface morphology variation are far more complicated than one may expect, presenting a significant challenge in determining the most appropriate method of interpreting surface state. For the present studies, we disclose the important caveat that the SSE yields are sensitive to the collector's surface state, which may change throughout the experiment. Characterizing the extent of SSE yield sensitivity and measurement stability are subjects of on-going investigations.

4.3.1 SSE Yields Analysis and Discussion

In the plots shown in Figures 4.5 and 4.6, all error bars represent a single standard deviation from the mean of 250 samples per datapoint. Primary species potential is approximated as $V_{primary} \approx (V_{beam} - V_{TC})$, where V_{beam} is emitter bias potential, and V_{TC} is the Taylor cone voltage drop. For I_{beam}=260 nA, 400 nA, and 600 nA, Gamero-Castaño determined $V_{TC} \approx$200 V, 400 V, and 600 V, respectively [58].

The positive and negative SSE yields (γ_+ and γ_-) obtained at the center of the plume are shown as a function of beam potential for each I_{beam} setpoint in Figure 4.5. At the center of the plume, SSE yields obey an approximately linear dependence on primary potential. A disparity in the slopes for γ_+ and γ_- gives an intersection of the curves at $4.2\,\text{kV} \pm 250\,\text{V}$. At the primary species potential,

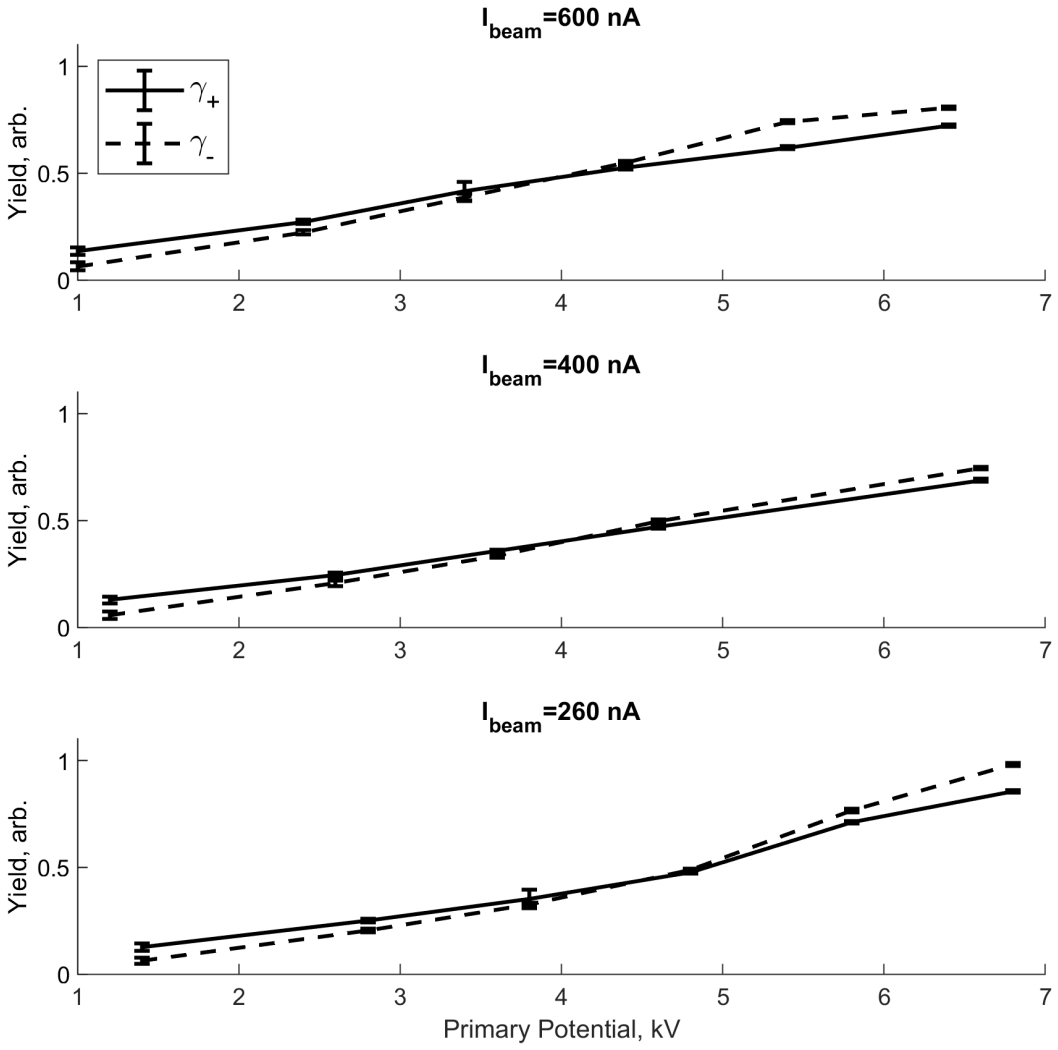

Figure 4.5: Centerline yields.

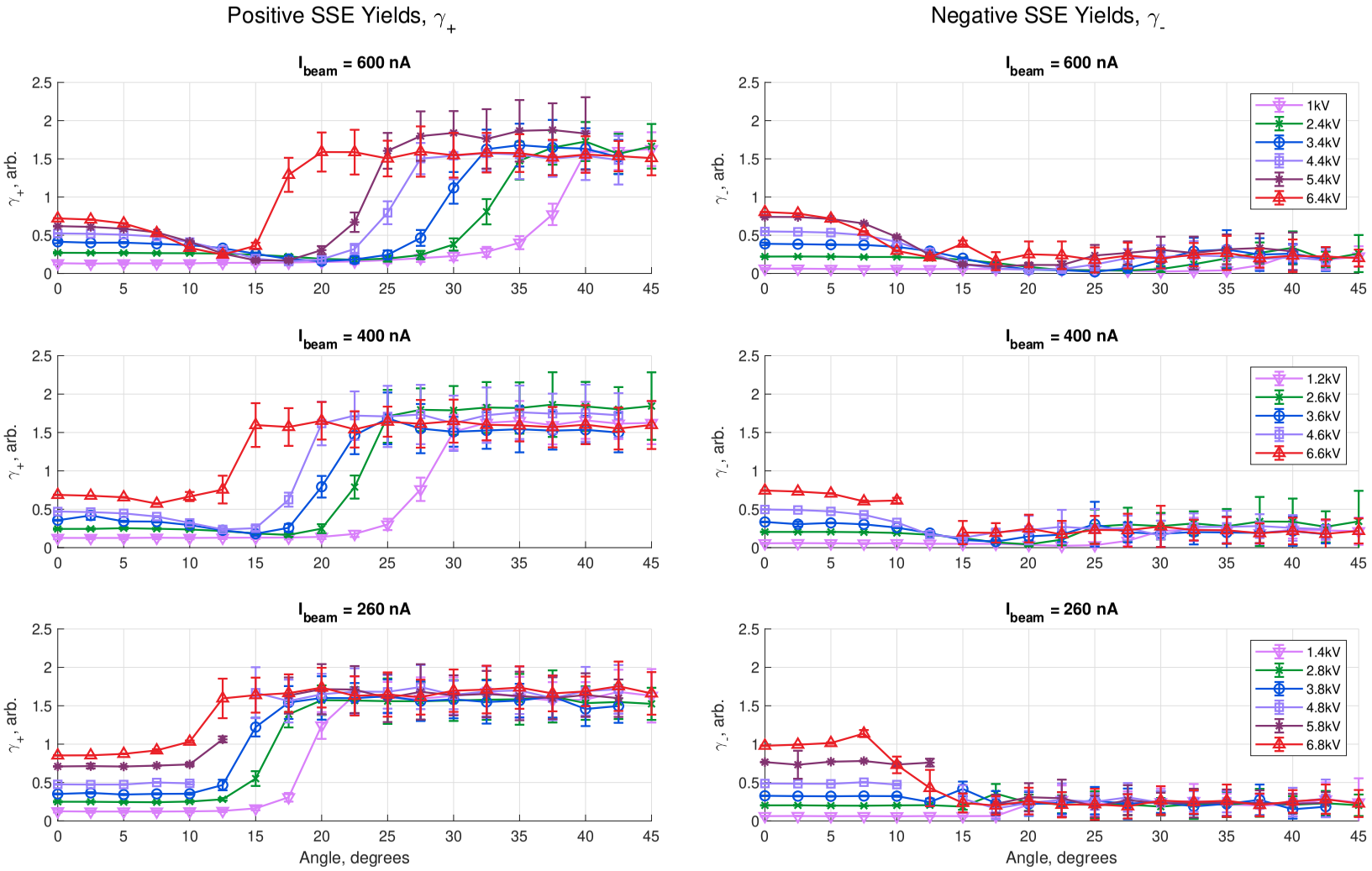

Figure 4.6: Angular distributions of positive and negative SSE yields (γ_+ and γ_-), over a parametric sweep of V_{beam} and I_{beam}. Left image: Positive SSE Yields. Right image: Negative SSE Yields.

the γ_+ values are greater than γ_- by $0.06-0.07$, whereas at the maximum primary species potential potential, the γ_- values are greater than γ_+ by approximately $0.08-0.15$. SSE yield disparities will introduce elevated uncertainty into plume current measurements if not accounted for in correction during data analysis.

The data shown in Figure 4.6 confirm that γ_+ and γ_- have a strong dependence on plume angle, beam voltage, and beam current. The angular distributions of γ_+ and γ_- exhibit different trends at higher angles, and have distinct dependencies on beam energy. Since SSE behavior is strongly linked to the primary species characteristics, the trends seen in the SSE measurements can be reasonably explained through the prevailing understanding of electrospray beam structure.

The ensuing discussion will first focus on the the beam voltage and angular dependencies for the $I_{beam} = 600\,\text{nA}$ dataset. At the lowest beam potentials, SSE yield appears relatively constant across the plume, with a concave upward increase in the yield at the highest resolved angles. Studies examining the structure of an electrospray plume in vacuum have shown that the mean specific charge of primary species obey remarkably similar angular distributions [150, 56]. Electrosprayed species are nearly monoenergetic, so higher specific charge species will have a greater terminal velocity. SSE yields are strongly dependent on the impact velocity of the primary species, so it's sensible to expect the specific charge distributions to correlate strongly with the SSE yields.

Two trends are observed with an increase in beam voltage: (1) the angular distribution appears to "tighten", where onset of the concave upward increase in yield occurs at smaller polar angles, and (2) a superposed Gaussian distribution emerges in the center of the plume with a monotonically increasing peak value. Tightening of the angular distribution with increasing beam voltage is consistent with the electrostatic lensing of primary species caused by the accelerator electrode [122, 184]. The Gaussian yield distribution that emerges at small polar angles is likely caused by ion impacts and droplet desorption, where each mechanism separately contributes to γ_- and γ_+.

A natural consequence of charged nanodroplet emission in vacuum is the solvation of ions from both the droplets, and the jet [58, 136]. Ions evaporated from droplets tend to be confined

by space charge potential within the beam, and focused onto the center axis. Droplet-born ions constitute about 15% to 25% of current at the center of the plume, and the ion population decays at higher angles. The observed Gaussian yield distributions of SSE yield in Figure 4.6 agree with experimentally and computationally resolved ion trajectories [56, 136]. At elevated beam voltages, high-specific charge ions are far above the specific energy threshold for onset of electron emission and molecular dissociation, so ions are likely the dominant contributors to γ_{-}.

As beam voltage increases, the droplet population traverses the threshold for shock-induced desorption, where secondaries emitted from desorption should be entirely positive [77]. The desorbed "dry patch" observed in Figure 3.10 reasonably agrees with the superposed Gaussian yield distribution, suggesting that desorption is a dominant contributor to positive SSE in the center of the plume at elevated beam energies. The extent to which ions and droplets each contribute to γ_{+} is challenging to evaluate, owing to the natural emission of ions from the charged primary droplets.

For the most part, the beam energy and angular trends hold for each I_{beam} case, with the exception of the superposed Gaussian yield distribution that emerges with increasing energy. As I_{beam} is reduced, the distributions trend towards more flat-topped distributions, e.g. super-Gaussian functions.

4.4 Application to Experimental Results

In previous sections, the governing equations were applied to the CMNT testing arrangement at JPL. Geometric factors were obtained using numerical simulations, and SSE yields were interpreted from experiments conducted on the CMNT. 260 nA, 400 nA, and 600 nA tests.

SSE yields are applied to the ESCARGOT model by selecting values at angles that correspond to emitter line-of-sight with the grids ($\theta > 35°$). Yields corresponding to the beam target were obtained by applying selective secondary species suppression analysis to the beam target biasing experiment data presented in Chapter 3.1.

Substituting values into the coefficients in 4.19 through 4.22, we arrive at a final matrix repre-

senting charge transport in the Busek CMNT. Using SSE yields obtained from the 600 nA experiment:

$$\begin{bmatrix} 1 & -0.035 & -2.6\times10^{-3} & -1.093\times10^{-6} \\ 0 & -1.036 & 0.3589 & 46.160\times10^{-6} \\ 0 & 0 & -1.8637 & 3.2\times10^{-3} \\ 0 & 0 & 0.5041 & 0.9854 \end{bmatrix} \begin{bmatrix} J^P_{total} \\ J^P_{ex} \\ J^P_{ac} \\ J^P_{bt} \end{bmatrix} = \begin{bmatrix} I^M_{em} \\ I^M_{ex} \\ I^M_{ac} \\ I^M_{bt} \end{bmatrix} \tag{4.30}$$

Using SSE yields obtained from the 400 nA experiment:

$$\begin{bmatrix} 1 & -0.0489 & -4.1\times10^{-3} & -3.433\times10^{-6} \\ 0 & -1.051 & 0.1897 & 1.4504\times10^{-4} \\ 0 & 0 & -1.7205 & 5.4\times10^{-3} \\ 0 & 0 & 0.5292 & 0.9748 \end{bmatrix} \begin{bmatrix} J^P_{total} \\ J^P_{ex} \\ J^P_{ac} \\ J^P_{bt} \end{bmatrix} = \begin{bmatrix} I^M_{em} \\ I^M_{ex} \\ I^M_{ac} \\ I^M_{bt} \end{bmatrix} \tag{4.31}$$

Using SSE yields obtained from the 300 nA experiment:

$$\begin{bmatrix} 1 & -0.054 & -2.0\times10^{-3} & -5.4105\times10^{-6} \\ 0 & -1.057 & 0.2311 & 2.2859\times10^{-4} \\ 0 & 0 & -1.9491 & 7.7\times10^{-3} \\ 0 & 0 & 0.7165 & 0.9644 \end{bmatrix} \begin{bmatrix} J^P_{total} \\ J^P_{ex} \\ J^P_{ac} \\ J^P_{bt} \end{bmatrix} = \begin{bmatrix} I^M_{em} \\ I^M_{ex} \\ I^M_{ac} \\ I^M_{bt} \end{bmatrix} \tag{4.32}$$

Inverting each coefficient matrix and multiplying it by the measured current matrix provides solutions for the actual impingement currents, J^P_i. Since J^P_{total} represents the total emitted cur-

rent, and the remaining terms represent the true primary current collected by each electrode, the solutions should obey:

$$J^P_{total} - (J^P_{ex} + J^P_{ac} + J^P_{bt}) = 0, \tag{4.33}$$

where the negative sign indicates that emitted and collected primary species should have opposite current polarities. Equation 4.33 is an indicator of the relative accuracy of the model. Three operating setpoints were analyzed using the ESCARGOT model. The interpreted results are shown in Table 4.3.

The $\sum I^M$ is the aggregate of all measured currents, and $\sum I^P$ is the current conservation expression in equation 4.33. Ideally, the measured current should also be conserved but $\sum I^M$ shows that there is an approximately 10 nA discrepancy in experimental measurements for each operating point. The considerable violation of current conservation in the experiment measurements is due to loss of secondary current from the beam target to the vacuum chamber. For the ESCARGOT model output, currents are conserved to $<$20 pA, which suggests that the model appropriately interprets the emission and transport of secondary species.

The accelerator and extractor currents exhibit significant differences between measured and true current. When positive species are collected by an electrode or when negative species are emitted, the current transducer registers a negative current, and vice versa. The accelerator collects positive primary and secondary species, and emits negative secondaries, so all phenomena occurring at the accelerator contributes to negative measured current. The extractor collects both positive primaries and negative secondaries, which means that the currents introduced by both polarities of charge may negate each other. Indeed, enough negative secondary current is collected on the extractor that the polarity is positive in the experiment measurements. True accelerator current is 39% to 64% lower than measured current. Neglecting the sign flip, the true extractor current is 41% to 76% greater than measured current. The significant differences in measured and interpreted current underscores why accounting for SSE is critical for evaluating electrospray thrusters.

Table 4.3: True impingement currents obtained using ESCAR-GOT to interpret currents measured in JPL's CMNT testing setup.

Current Setpoint	Measured Current	True Current
300 nA	$I^M_{em} = 300.9605\,\text{nA}$	$J^P_{total} = 300.9298\,\text{nA}$
	$I^M_{ex} = 0.3654\,\text{nA}$	$J^P_{ex} = -0.5161\,\text{nA}$
	$I^M_{ac} = -1.3265\,\text{nA}$	$J^P_{ac} = -0.5087\,\text{nA}$
	$I^M_{bt} = -289.5881\,\text{nA}$	$J^P_{bt} = -299.9092\,\text{nA}$
	$\sum I^M = 10.4112\,\text{nA}$	$\sum J^P = -0.0042\,\text{nA}$
400 nA	$I^M_{em} = 401.0512\,\text{nA}$	$J^P_{total} = 401.0293\,\text{nA}$
	$I^M_{ex} = 0.2140\,\text{nA}$	$J^P_{ex} = -0.3774\,\text{nA}$
	$I^M_{ac} = -1.0498\,\text{nA}$	$J^P_{ac} = -0.6397\,\text{nA}$
	$I^M_{bt} = -390.2597\,\text{nA}$	$J^P_{bt} = -399.9956\,\text{nA}$
	$\sum I^M = 9.9373\,\text{nA}$	$\sum J^P = 0.016\,59\,\text{nA}$
600 nA	$I^M_{em} = 602.8110\,\text{nA}$	$J^P_{total} = 602.7966\,\text{nA}$
	$I^M_{ex} = 0.2028\,\text{nA}$	$J^P_{ex} = -0.3611\,\text{nA}$
	$I^M_{ac} = -1.1941\,\text{nA}$	$J^P_{ac} = -0.4280\,\text{nA}$
	$I^M_{bt} = -593.4510\,\text{nA}$	$J^P_{bt} = -602.0275\,\text{nA}$
	$\sum I^M = 8.3543\,\text{nA}$	$\sum J^P = -0.0200\,\text{nA}$

4.5 Conclusions

Chapter 4 discussed a charge conservation formalism for resolving secondary species transport in electrospray thrusters. The derived ESCARGOT model provides the true impingement currents based on two variables: geometric factors, and SSE yields. Geometric factors describe the inter-electrode transport of charged species. SSE yields are a measure of the amount of secondary species emitted per incident primary. The ESCARGOT model is applied to a testing arrangement of the Busek CMNT operated at JPL. Geometric factors for the setup were obtained using COMSOL Multiphysics®, and SSE yields were obtained in experiments conducted at JPL (discussed in Chapter 3.2.3) [196, 197].

All geometric factors and SSE yields were substituted into the system of equations, and the true impingement currents were found for three different thruster operating points. The true accelerator impingement current was found to be 39% to 64% lower than the uncorrected measurements, and true extractor impingement was found to be 41% to 76% higher. The significant discrepancy between uncorrected current measurements and true impingement currents determined by ESCARGOT emphasizes the need to account for SSE to improve confidence in using terrestrial qualification efforts for in-space life prediction. While the study presented herein highlighted the use of ESCARGOT to interpret experimental measurements, the model may also take outputs from computational simulations of the plume and provide predictions for experimental measurements. Thus the ESCARGOT model serves as an important link between lifetime prediction models and thruster lifetime qualification testing.

CHAPTER 5

Strategies for Mitigating Facility Effects

The analyses presented in Chapter 2 showed that electrospray thrusters always operate above the thresholds for onset of SSE. Several practical considerations are suggested that may minimize the impact of SSE on thruster behavior based on SSE phenomena discussed throughout the presented paper. The key to minimizing vacuum facility effects for electrospray thrusters is to minimize SSE and its effects on the thruster operation. To this end, two guiding principles should be followed: (1) SSE should be minimized through the use of an effective beam target for the thruster plume. (2) The facility and thruster should be arranged to minimize primary beam impingement on other facility and thruster surfaces, as well as minimize the effects of secondary species on the thruster plume, thruster surfaces, and diagnostics.

Flat beam target geometries should be avoided to limit the reflection and impingement of secondary species on the thruster. Instead, presenting an angled surface to the thruster plume minimizes the sputtering yield and diverts emitted secondaries away from the thruster. For example, chevron or merlon-style beam target configurations have been successfully employed in LMIS thruster testing to limit target sputtering and backstreaming secondaries [198]. Demmons et al. [123] presented a corrugated beam target geometry designed for mitigating SSE during thruster lifetime testing. Ensuring adequate thruster-to-target distance ($> 1\,\mathrm{m}$) and applying a modest target bias potential ($> 100\,\mathrm{V}$) that matches the polarity of the emitter potential may suppress secondary species that would otherwise backstream and impinge on the emitter. Collector and beam target biasing has been successfully employed in LMIS/FEEP thruster testing to mitigate secondary electron emission [39, 13, 198, 38]. With ILIS thrusters, the presence of both anionic and cationic secondary

species suggests that more sophisticated beam target arrangements and biasing schemes may be necessary, such as the electrode arrangement tested in Section 3.1. As discussed above, the beam target used in the presented experiments was located only $\sim$0.1 m downstream of the thruster, so complexity of the beam target design trades with the distance between the target and thruster.

To reduce thruster complexity, negatively-biased accelerator electrodes are not commonly used on ILIS thrusters, yet the sensitivity of the emitter to SSE-induced Ohmic dissipation suggests accelerator electrodes may be necessary to prevent backstreaming current. All diagnostics that rely on current measurements (e.g. Faraday probes, time-of-flight spectrometers, retarding potential analyzers, etc) must also be designed with SSE-suppression techniques in mind, since secondary currents may contribute to considerable uncertainty.

Material choice is an important consideration for electrospray thruster testing facilities, yet material responses to ionic liquid droplet or molecular ion impacts have not been adequately studied. Indium LMIS/FEEP thrusters have utilized targets comprised of solid indium to minimize contamination owing to backstreaming sputterants [38, 170]. However, coating a target with ionic liquid propellant is costly and likely will not produce the same benefits because emitted secondary species that backstream to the thruster are comprised of dissociated constituents ejected from the impact site. Generally, facility materials that will intercept the plume should consist of conductive materials that are minimally reactive and exhibit lower sputtering and secondary electron yields, such as stainless steel, graphite, or refractory metals.

While SSE may be minimized by implementing appropriate beam target geometries and biasing schemes, the extent of the uncertainty caused by any persisting SSE effects are unknown. To that end, we recommend a basic SSE quantification test as a baseline step for electrospray thruster evaluation, where a biased beam target is swept over a modest voltage range to evaluate the extent of impact that SSE imposes on thruster electrode measurements. Applying the generalized governing equations for the ESCARGOT model defined in Chapter 4 may allow thruster operators to interpret currents measured on thruster electrodes and facility walls as a strategy for mitigating SSE.

CHAPTER 6

Conclusions and Future Work

6.1 Summary of Conclusions

The work discussed herein consists of the first comprehensive study of secondary species emission (SSE) in the context of electrospray propulsion. The primary conclusions from this work are as follows:

1. SSE has a significant effect on electrospray thruster life, performance, facility effects, and spacecraft interactions.

2. SSE behavior can be effectively monitored and mitigated in a terrestrial vacuum test environment.

3. SSE behavior can be modeled using a combination of analytical charge conservation, experimental SSE yield measurements, and computational evaluation of geometric factors.

Through an overview of the theory and onset thresholds for different SSE mechanisms, it has been shown that SSE should always occur for electrospray thrusters. SSE may result in the emission of a diverse population of secondary species, including electrons, ions, oligomeric clusters, and droplets. The charge state of secondary species may be positive, negative, or neutral.

The experimental and analytical studies presented in Chapter 3 examined the consequences of SSE on electrospray thruster behavior, including measurement uncertainty, thruster-to-facility coupling, performance loss, and potential life-limiting phenomena.

The beam target biasing experiment in Chapter 3.1 illustrated the coupling between thruster and facility that is caused by SSE. SSE can contribute to significant uncertainty in lifetime estimates if not appropriately mitigated. Different regimes of operation were identified based on the applied beam target bias, and the total facility current response. Chapter 3.2 provided a detailed study of SSE-induced measurement uncertainty for plume current. The selective secondary species suppression technique discussed in Chapter 3.2.1 quantifies electrospray SSE by taking advantage of the bipolar sensitivity of secondaries to an applied voltage, and the large energy discrepancy between primary and secondary species. To rigorously quantify positive and negative charge yields, a bespoke "SSE Probe" was developed and tested with an ionic liquid electrospray device. The SSE Probe was successfully employed to obtain SSE-corrected beam current measurements, as well as positive and negative SSE yields. The reported experimental data represent the first reported spatial distributions of positive and negative charge yields obtained in an ionic liquid electrospray plume.

The SEM micrographs discussed in Chapter 3.3 show different surfaces after exposure to electrospray plumes, providing insight into the phenomena that contribute to SSE. Images of the beam target exposed to a droplet-rich plume confirms the predicted onset of shock-induced desorption at elevated beam energies. Microscopy of an ILIS extractor reveals chemical etching likely due to reactions with dissociated molecular constituents. Both images provide visual evidence of SSE effects occurring in electrospray devices.

The heat and mass flux models in Chapter 3.4 show that backstreaming secondary species may induce Ohmic dissipation at the emission site. Backstreaming current density contributing to 0.052% of emitter current density can cause physical property variation in the ionic liquid that alters the thruster's emission characteristics, invalidating the isothermal assumption used to derive scaling laws. SSE-induced Ohmic dissipation may also cause anomalous neutral mass loss, which is a major performance limitation in ILIS thrusters. Secondary current density contributing to 2.65% of emitted current may cause the $0.86\,\mu g\,s^{-1}$ neutral mass flow rate observed in the AFET-2 thruster [3].

The results of the optical emission spectroscopy study in Chapter 3.5 strongly suggest that glow observed when operating ILIS devices in vacuum is caused by electron excitation resulting from surface impact phenomena such as sputtering and molecular dissociation. Atomic lines for constituents of the [EMI]Im propellant, and metals from the thruster were observed. A broadband spectral emission line shape was observed that is likely due to molecular emission. Glow for electrospray devices is primarily an indicator of plume impingement on the downstream electrodes of the electrospray device and downstream facility surfaces.

In Chapter 4, the governing equations for the ESCARGOT model were derived. The ESCARGOT model provides the true plume impingement currents based on geometric factors, and SSE yields. ESCARGOT was applied to a testing arrangement of the Busek CMNT operated at JPL. Geometric factors for the setup were obtained using COMSOL Multiphysics®, and SSE yields were obtained in an experiment conducted at JPL (discussed in Chapter 3.2.3). While ESCARGOT was applied to interpret experimental measurements, the model may also take outputs from computational simulations of the plume and provide predictions for experimental measurements. Thus the ESCARGOT model serves as an important link between lifetime prediction models and thruster testing.

Finally, recommended practices for mitigating SSE were discussed. The main recommendations are (1) ensure an adequate beam target that is sufficiently distant from the thruster, (2) choose appropriate materials for components that will be exposed to the plume, (3) sweep the beam target to examine thruster sensitivity to facility effects, and (4) apply the generalized ESCARGOT model to the thruster and facility to mitigate uncertainty due to SSE.

6.2 Future Work

6.2.1 Deposited Droplet Mass

Understanding mass loss and deposition due to splashing and desorption of droplets is key to quantifying measurement uncertainty. Quartz crystal microbalance (QCM) probes are the main diagnostic used for characterizing mass flux profiles for droplet-mode thruster plumes [144]. The angular distribution of mass flux in a plume is used to estimate the extent of grid impingement, and serves as the primary method of evaluating thruster lifetime. QCM diagnostics are subject to desorption or splashing of incident droplets, which introduces uncertainty to the mass flux measurements. Splashing mass deposition models are necessary to accurately relate QCM measurements to plume mass flux profiles, thereby providing accurate assessments of thruster life. Mass deposition models have been developed for macroscale droplets to study fuel injection in combustion engines or aircraft icing [199, 200, 201], and for microscale droplets for inkjet or electrohydrodynamic printing [202, 203]. By contrast, electrospray thruster droplets have diameters on the order of 10's to 100's of nanometers, undergo impacts onto thin films at extremely low ambient pressure, and may be charged to a reasonably large fraction of the Rayleigh limit. Therefore, the validity of adapting existing mass deposition models for droplet-mode electrospray thrusters is dubious.

Nanodroplet impact studies rely almost exclusively on theoretical frameworks or molecular dynamics (MD) simulations [114, 115, 116] and are extremely challenging to validate experimentally. Furthermore, the behavior of ionic liquids at the nanoscale is unique to fluids commonly modelled in nanodroplet impact MD simulations. To adequately address uncertainty due to splashing, models must be developed to capture the deposited mass fraction of charged nanodroplet impacts in vacuum. The velocity, incidence angle, and film thickness are important contributors to deposited mass fraction that must be considered.

6.2.2 Emission Site Heating

Self-heating via viscous and Ohmic dissipation and external-heating via SSE-induced Ohmic dissipation may contribute to anomalous neutral mass loss, thus reducing thruster I_{sp} and efficiency. Evidence of emission site heating comes from analytical and computational models [160, 161, 77], so a key research gap is the experimental validation of temperature profiles on ILIS thruster emitters. Such experimental approaches are challenging, as direct temperature measurements of the emission site aren't possible with traditional temperature probes (e.g. thermocouples) due to the very small geometries involved (emitter height $< 500\,\mu m$ and tip curvature $< 20\,\mu m$). Furthermore, direct probing of the emitter is not possible without altering the electric field or potentially interfering with flow, thus disrupting the emission process.

Non-invasive temperature measurements are optimal, but present their own set of challenges. The temperature range of interest is 300 K to 700 K, which corresponds to maximum blackbody wavelengths of $\sim$4 µm to 10 µm. Therefore, optics designed for infrared wavelengths are necessary for thermal imaging microscopy of the emission site. Long-distance microscopy is commonly used to image electrospray thrusters emission sites [178, 122, 179], yet to the authors' knowledge, there are no commercially available long distance microscopes capable of imaging mid-infrared wavelengths.

6.2.3 Plume Structure

The plume deposition pattern examined in Section 3.3.1 may be explained by the existence of a subsidiary plume consisting of pseudo-neutral species born from the coulombic fission process. Since pseuo-neutrals are born before they've been completely accelerated, and their trajectories are relatively unchanged by the accelerator electrode's potential, their angular distribution should be the same with or without a negatively-biased accelerator. Therefore, the pseudo-neutral population may be identified by taking RPMA plume sweeps of JPL's embodiment of the CMNT with and without an applied accelerator bias.

6.2.4 Molecular Dynamics

Based on the presented findings, we recommend investigations of the observed wideband molecular line shape. Infrared spectroscopy may provide important insights since molecular rovibrational resonances occur in the infrared range. Molecular dynamics simulations capable of emulating covalent bonds would enable predictions of the dissociation products and their temperatures, which are key to accurately analyzing molecular spectra. Predicting molecular dissociation products is also critical for understanding ensuing chemical reactions with the surface material, which is relevant to ionic liquid electrospray thruster interactions with spacecraft, and ILIS for other applications such as materials processing and mass spectrometry.

6.2.5 Spacecraft Interactions

SSE has been extensively discussed in this dissertation in the context of facility effects. It is likely that primary species impingement will also have a significant impact on spacecraft components that intercept the plume. Further examination of how primary impacts affect surfaces is necessary to inform appropriate thruster design and integration with the spacecraft.

6.2.6 SSE Behavior and Properties

SSE yields calculated by selective secondary species suppression described in Chapter 3.2.1 represent the aggregate yields of many simultaneous SSE processes occurring at the surface due to the impact of the [EMI]Im species emitted by the electrospray. Therefore, an important extension of the presented research would involve partitioning SSE yields by the specific charge of incident primary species in the plume. A deficiency in predicting electrospray lifetime using accumulated mass is the lack of accounting for mass of backstreaming secondaries. Mass spectrometry of secondary species emitted by ion and droplet impacts on thruster-relevant surfaces would inform the extent of mass accumulation due to secondaries.

6.2.7 Neutral Species

A final remark: the models and experiments discussed herein completely neglect the behavior of neutral species. It is highly likely that the emitted secondaries contains a neutral population, particularly with the presence of shock-induced desorption discussed in Chapter 3.3.1. Neutral secondary mass may conflate post-test mass accumulation measurements, and is difficult to mitigate due to it's insensitivity to electric and magnetic fields. Future work should endeavor to examine the behavior of neutrals, and to determine appropriate methods of mitigating neutral SSE.

Appendix A

Mass Flux Model

K_1 and K_3 are pre-exponential constants associated with the Langmuir and Arrhenius equations. For [EMI]Im, $K_1 = 7.6 \times 10^6 \text{kgs}^{-1}\text{K}^{-1/2}$, and $K_3 = 2.4 \times 10^{11} \text{kgs}^{-1}$ were found by regression of data obtained via Thermogravimetric Analysis Mass Spectrometry (TGA-MS) [162].

K_2 is an area scaling constant that accounts for the surface area of the thermogravimetric apparatus' crucible used to determine K_1 [162], and is evaluated by:

$$K_2 = \frac{A_{em}}{A_{crucible}}, \tag{A.1}$$

where A_{em} is the surface area of the emitter, and $A_{crucible}$ is the area of the crucible. To evaluate K_2, the Q50 TGA-MS used by Chen et al. [162] has a crucible area of $A_{crucible} = 2.14\,\text{cm}^2$.

Appendix B

Material properties for [EMI]Im and [EMI]BF_4

Table B.1: Material properties for [EMI]Im and [EMI]BF_4 at 293 K

Property	Symbol	[EMI]Im	Reference	[EMI]BF_4	Reference
Density	ρ	$1518.48\,\mathrm{kg/m^3}$	[204]	$1252.2\,\mathrm{kg/m^3}$	[10]
Viscosity	μ	$0.03246\,\mathrm{Pa\,s}$	[205, 155]	$0.03607\,\mathrm{Pa\,s}$	[10, 157]
Surface Tension	γ	$0.0359\,\mathrm{N\,m^{-1}}$	[206]	$0.0452\,\mathrm{N\,m^{-1}}$	[207]
Electrical Conductivity	κ	$0.921\,\mathrm{S\,m^{-1}}$	[205, 156]	$1.59\,\mathrm{S\,m^{-1}}$	[208, 158]
Thermal Conductivity	k	$0.12\,\mathrm{W\,m^{-1}\,K}$	[204]	$0.2\,\mathrm{W\,m^{-1}\,K}$	[10]
Relative Permittivity	ε_r	12.25	[209]	14.8	[210]
Speed of Sound	c_0	$1250\,\mathrm{m\,s^{-1}}$	[211]	$1640\,\mathrm{m\,s^{-1}}$	[212]
Heat of Vaporization	ΔH_{vap}	$120\,\mathrm{kJ\,mol^{-1}}$	[163]	$128\,\mathrm{kJ\,mol^{-1}}$	[9]
Activation Energy	E_a	$118\,\mathrm{kJ\,mol^{-1}}$	[213]	$124\,\mathrm{kJ\,mol^{-1}}$	[214]
Decomposition Temperature	T_{dec}	350 °C	[162]	445 °C	[10]

Bibliography

[1] E. Kulu, “Nanosats database,” 2021. [Online]. Available: www.nanosats.eu

[2] M. R. Natisin, H. L. Zamora, W. A. McGehee, N. I. Arnold, Z. A. Holley, M. R. Holmes, and D. Eckhardt, “Fabrication and characterization of a fully conventionally machined, high-performance porous-media electrospray thruster,” *Journal of Micromechanics and Microengineering*, vol. 30, no. 11, p. 115021, sep 2020.

[3] M. R. Natisin, H. L. Zamora, Z. A. Holley, N. Ivan Arnold, W. A. McGehee, M. R. Holmes, and D. Eckhardt, “Efficiency mechanisms in porous-media electrospray thrusters,” *Journal of Propulsion and Power*, pp. 1–10, May 2021.

[4] E. Petro, A. Bruno, P. Lozano, L. E. Perna, and D. Freeman, “Characterization of the tile electrospray emitters,” ser. AIAA Propulsion and Energy Forum. American Institute of Aeronautics and Astronautics, Aug 2020. [Online]. Available: https://doi.org/10.2514/6.2020-3612

[5] T. Randolph and J. Ziemer, “Microthruster propulsion for the space technology 7 (ST7) technology demonstration mission,” ser. Joint Propulsion Conferences. American Institute of Aeronautics and Astronautics, Jul 2006, 0. [Online]. Available: https://doi.org/10.2514/6.2006-4320

[6] J. K. Ziemer, T. Randolph, V. Hruby, D. Spence, N. Demmons, T. Roy, W. Connolly, E. Ehrbar, J. Zwahlen, and R. Martin, “Colloid microthrust propulsion for the space technology 7 (st7) and lisa missions,” *AIP Conference Proceedings*, vol. 873, no. 1, pp. 548–555, Nov 2006. [Online]. Available: https://doi.org/10.1063/1.2405097

[7] E. Grustan-Gutierrez and M. Gamero-Castaño, “Microfabricated electrospray thruster array with high hydraulic resistance channels,” *Journal of Propulsion and Power*, vol. 33, no. 4, pp. 984–991, Jul 2017. [Online]. Available: https://doi.org/10.2514/1.B36268

[8] Keithley, *Low Level Measurements Handbook*. Keithley Instruments, 2004.

[9] D. H. Zaitsau, K. Fumino, V. N. Emel'yanenko, A. V. Yermalayeu, R. Ludwig , and S. P. Verevkin, "Structure–property relationships in ionic liquids: A study of the anion dependence in vaporization enthalpies of imidazolium-based ionic liquids," *ChemPhysChem*, vol. 13, no. 7, pp. 1868–1876, May 2012.

[10] M. E. Valkenburg, R. L. Vaughn, M. Williams, and J. S. Wilkes, "Thermochemistry of ionic liquid heat-transfer fluids," *Thermochimica Acta*, vol. 425, no. 1, pp. 181–188, Jan 2005.

[11] C. Chen, M. Chen, W. Fan, and H. Zhou, "Effects of non-uniform operation of emission sites on characteristics of a porous electrospray thruster," *Acta Astronautica*, vol. 178, pp. 192–202, Jan 2021.

[12] M. Bretti, "AIS-ILIS1 ionic liquid ion source electrospray thruster V6, ignition test 6," Applied Ion Systems, Tech. Rep., December 2020, Available at https://appliedionsystems.com/wp-content/uploads/2020/09/AIS-TR-015-Ignition-Test-6-of-AIS-ILIS1-V6-08-21-2020.pdf.

[13] M. Tajmar, I. Vasiljevich, and W. Grienauer, "High current liquid metal ion source using porous tungsten multiemitters," *Ultramicroscopy*, vol. 111, no. 1, pp. 1–4, Dec 2010.

[14] D. V. M. Máximo and L. F. Velásquez-García, "Additively manufactured electrohydrodynamic ionic liquid pure-ion sources for nanosatellite propulsion," *Additive Manufacturing*, vol. 36, p. 101719, Dec 2020.

[15] PolySat Staff, "Cal poly cubesat laboratory, 2018-2019 annual report," 2019. [Online]. Available: http://mstl.atl.calpoly.edu/CubeSatAnnualReport18-19.pdf

[16] J. Muller, R. Hofer, and J. Ziemer, "Survey of propulsion technologies applicable to cubesats," in *Joint Army-Navy-NASA-Air Force (JANNAF)*, Colorado Springs, CO, May 2010. [Online]. Available: https://ntrs.nasa.gov/citations/20100032899

[17] "Mitigation of orbital debris in the new space age," Federal Communications Commission, Washington, DC, Tech. Rep., 2020, fCC-20-54. [Online]. Available: fcc.gov/document/fcc-updates-orbital-debris-mitigation-rules-new-space-age-0

[18] A. Lawrence, M. L. Rawls, M. Jah, A. Boley, F. Di Vruno, S. Garrington, M. Kramer, S. Lawler, J. Lowenthal, J. McDowell, and M. McCaughrean, "The case for space environmentalism," *Nature Astronomy*, vol. 6, no. 4, pp. 428–435, Apr 2022. [Online]. Available: https://doi.org/10.1038/s41550-022-01655-6

[19] M. Gomez Jenkins, D. Krejci, and P. Lozano, "Cubesat constellation management using ionic liquid electrospray propulsion," *Acta Astronautica*, vol. 151, pp. 243–252, 2018.

[20] G. I. Taylor, "Disintegration of water drops in an electric field," *Proceedings of the Royal Society of London. Series A. Mathematical and Physical Sciences*, vol. 280, no. 1382, pp. 383–397, Jul 1964. [Online]. Available: https://doi.org/10.1098/rspa.1964.0151

[21] L. Rayleigh, "On the equilibrium of liquid conducting masses charged with electricity," *The Philosophical Magazine*, vol. 14, pp. 184–186, 1882.

[22] Nobel Prize Outreach, "The nobel prize in chemistry 2002," 2002. [Online]. Available: https://www.nobelprize.org/prizes/chemistry/2002/summary/

[23] J. B. Fenn, M. Matthias, M. C. Kai, W. S. Fu, and C. M. Whitehouse, "Electrospray ionization for mass spectrometry of large biomolecules," *Science*, vol. 246, no. 4926, pp. 64–71, Oct 1989.

[24] M. M. Hohman, M. Shin, G. Rutledge, and M. P. Brenner, "Electrospinning and electrically forced jets. I. stability theory," *Physics of Fluids*, vol. 13, no. 2201, 2001.

[25] ——, "Electrospinning and electrically forced jets. II. applications," *Physics of Fluids*, vol. 13, no. 2221, 2001.

[26] A. Jaworek, "Electrospray droplet sources for thin film deposition," *Journal of Materials Science*, vol. 42, no. 1, pp. 266–297, Jan 2007.

[27] K. CLARK, "Survey of electric propulsion capability," ser. Joint Propulsion Conferences. American Institute of Aeronautics and Astronautics, Oct 1974. [Online]. Available: https://doi.org/10.2514/6.1974-1082

[28] M. Gamero-Castano and V. Hruby, "Electrospray as a source of nanoparticles for efficient colloid thrusters," *Journal of Propulsion and Power*, vol. 17, no. 5, pp. 977–987, Sep 2001. [Online]. Available: https://doi.org/10.2514/2.5858

[29] J. Ziemer and S. Merkowitz, "Microthrust propulsion for the lisa mission," ser. Joint Propulsion Conferences. American Institute of Aeronautics and Astronautics, Jul 2004. [Online]. Available: https://doi.org/10.2514/6.2004-3439

[30] J. Ziemer, "Colloid microthruster flight performance results from space technology 7 disturbance reduction system," in *International Electric Propulsion Conference*, Sept 2009, http://electricrocket.org/IEPC/IEPC-2009-242.pdf.

[31] J. Ziemer, C. Marrese-Reading, C. Dunn, A. Romero-Wolf, C. Cutler, S. Javidnia, T. Li, I. Li, G. Franklin, P. Barela, O. Hsu, P. Maghami, J. O'Donnell, J. Slutsky, J. I. Thorpe, N. Demmons, V. Hruby, and L. P. Team, "Colloid microthruster flight performance results from space technology 7 disturbance reduction system," in *International Electric Propulsion Conference*, Oct 2017, https://ntrs.nasa.gov/archive/nasa/casi.ntrs.nasa.gov/20170010216.pdf.

[32] B. Mennesson, A. Kiessling, and K. Warfield, "Habex: Habitable exoplanet observatory interim report," Astronomy, Physics and Space Technology Directorate, Jet Propulsion Laboratory, Tech. Rep., August 2018.

[33] National Academies of Sciences Engineering and Medicine, *Pathways to Discovery in Astronomy and Astrophysics for the 2020s*. Washington, DC: The National Academies Press,

2021. [Online]. Available: https://www.nap.edu/catalog/26141/pathways-to-discovery-in-astronomy-and-astrophysics-for-the-2020s

[34] Y.-h. Chiu and R. A. Dressler, "Ionic liquids for space propulsion," ser. ACS Symposium Series, vol. 975. American Chemical Society, Aug 2007, pp. 138–160.

[35] D. G. Courtney and H. Shea, "Influences of porous reservoir laplace pressure on emissions from passively fed ionic liquid electrospray sources," *Applied Physics Letters*, vol. 107, no. 10, p. 103504, Sep 2015.

[36] P. Lozano and M. Martínez-Sánchez, "Ionic liquid ion sources: characterization of externally wetted emitters," *Journal of Colloid and Interface Science*, vol. 282, no. 2, pp. 415–421, Feb 2005.

[37] D. G. Courtney, "Ionic liquid ion source emitter arrays fabricated on bulk porous substrates for spacecraft propulsion," Ph.D. dissertation, Massachusetts Institute of Technology, 2011.

[38] C. Marrese-Reading, J. Polk, J. Muller, A. Owens, M. Tajmar, C. Spindt, and R. Fink, "In-feep thruster ion beam neutralization with thermionic and field emission cathodes," in *International Electric Propulsion Conference*, Oct 2001, http://electricrocket.org/IEPC/290_1.pdf.

[39] M. Tajmar, A. Genovese, and W. Steiger, "Indium field emission electric propulsion microthruster experimental characterization," *Journal of Propulsion and Power*, vol. 20, no. 2, pp. 211–218, Mar 2004.

[40] P. C. Lozano, B. L. Wardle, P. Moloney, and S. Rawal, "Nanoengineered thrusters for the next giant leap in space exploration," *MRS Bulletin*, vol. 40, no. 10, pp. 842–849, Oct 2015.

[41] P. Lozano and M. Martinez-Sanchez, "Efficiency estimation of emi-bf4 ionic liquid electrospray thrusters," in *Joint Propulsion Conferences*. American Institute of Aeronautics and Astronautics, Jul 2005.

[42] D. G. Courtney, S. Dandavino, and H. Shea, "Comparing direct and indirect thrust measurements from passively fed ionic electrospray thrusters," *Journal of Propulsion and Power*, vol. 32, no. 2, pp. 392–407, Mar 2016.

[43] P. Lozano and M. Martínez-Sánchez, "Ionic liquid ion sources: suppression of electrochemical reactions using voltage alternation," *Journal of Colloid and Interface Science*, vol. 280, no. 1, pp. 149–154, Dec 2004.

[44] N. Brikner and P. C. Lozano, "The role of upstream distal electrodes in mitigating electrochemical degradation of ionic liquid ion sources," *Applied Physics Letters*, vol. 101, no. 19, p. 193504, Nov 2012.

[45] N. A. Brikner, "On the identification and mitigation of life-limiting mechanisms of ionic liquid ion sources envisaged for propulsion of microspacecraft," Ph.D. dissertation, Massachusetts Institute of Technology, 2015.

[46] D. Conroy and J. Ziemer, "Water contaminant mitigation in ionic liquid propellant," in *International Electric Propulsion Conference*, Sept 2009, https://trs.jpl.nasa.gov/handle/2014/44687.

[47] "TILE Propulsion," 2021. [Online]. Available: https://accion-systems.com/tile-propulsion/

[48] "BET-300P multi-axis precision electrospray thruster system," 2021. [Online]. Available: https://www.busek.com/bet-300p

[49] N. R. Demmons, D. Courtney, N. Alvarez, and Z. Wood, "Component-level development and testing of a colloid micro-thruster (cmt) system for the lisa mission," in *AIAA Propulsion and Energy Forum*, Aug 2019, https://doi.org/10.2514/6.2019-3815.

[50] N. R. Demmons, Z. Wood, and N. Alvarez, "Characterization of a high thrust, pressure-fed electrospray thruster for precision attitude control applications," in *AIAA Propulsion and Energy Forum*, Aug 2019.

[51] A. Thuppul, P. L. Wright, A. L. Collins, J. Ziemer, and R. E. Wirz, "Lifetime considerations for electrospray thrusters," *Aerospace*, 2020.

[52] J. Ziemer, C. M. Marrese-Reading, S. M. Arestie, D. G. Conroy, L. S. D., N. R. Demmons, M. Gamero-Castaño, and R. E. Wirz, "Lisa colloid microthruster technology development plan and progress," in *International Electric Propulsion Conference*, Sept 2019, http://electricrocket.org/2019/895.pdf.

[53] P. Lozano and M. Martinez-Sanchez, "Efficiency estimation of emi-bf4 ionic liquid electrospray thrusters," in *Joint Propulsion Conferences*. American Institute of Aeronautics and Astronautics, Jul 2005.

[54] D. Krejci, F. Mier-Hicks, R. Thomas, T. Haag, and P. Lozano, "Emission characteristics of passively fed electrospray microthrusters with propellant reservoirs," *Journal of Spacecraft and Rockets*, vol. 54, no. 2, pp. 447–458, Mar 2017.

[55] M. J. Davis, A. L. Collins, and R. E. Wirz, "Electrospray plume evolution via discrete simulations," in *36th International Electric Propulsion Conference*, ser. IEPC-2019-590, 2019. [Online]. Available: http://electricrocket.org/2019/590.pdf

[56] M. Gamero-Castaño, "The structure of electrospray beams in vacuum," *Journal of Fluid Mechanics*, vol. 604, p. 339–368, 2008.

[57] W. Deng and A. Gomez, "Influence of space charge on the scale-up of multiplexed electrosprays," *Journal of Aerosol Science*, vol. 38, no. 10, pp. 1062–1078, Oct 2007.

[58] M. Gamero-Castaño and A. Cisquella-Serra, "Electrosprays of highly conducting liquids: A study of droplet and ion emission based on retarding potential and time-of-flight spectrometry," *Phys. Rev. Fluids*, vol. 6, p. 013701, Jan 2021.

[59] S. Clark. (2020) Spacex's starlink network surpasses 400-satellite mark after successful

launch. [Online]. Available: https://spaceflightnow.com/2020/04/22/spacexs-starlink-network-surpasses-400-satellite-mark-after-successful-launch/

[60] D. A. Herman, T. Tofil, W. Santiago, H. Kamhawi, J. E. Polk, J. S. Snyder, R. R. Hofer, F. Picha, J. Jackson, and M. Allen, "Overview of the development and mission application of the advanced electric propulsion system (aeps)," in *35th International Electric Propulsion Conference*, ser. IEPC-2017-284, 2017.

[61] J. D. White, "Test like you fly: Assessment and implementation process," Aerospace Corp, Corporate Chief Engineering Office, Enterprise Mission Assurance, Tech. Rep., January 2010, TOR-2010(8591)-6.

[62] E. Dale, B. Jorns, and A. Gallimore, "Future directions for electric propulsion research," *Aerospace*, vol. 7, no. 9, 2020. [Online]. Available: https://www.mdpi.com/2226-4310/7/9/120

[63] S. E. Cusson, M. Byrne, B. Jorns, and A. Gallimore, "Investigation into the use of cathode flow fraction to mitigate pressure-related facility effects on a magnetically shielded hall thruster," in *AIAA Propulsion and Energy 2019 Forum*. [Online]. Available: https://arc.aiaa.org/doi/abs/10.2514/6.2019-4077

[64] R. R. Hofer and J. R. Anderson, "Finite pressure effects in magnetically shielded hall thrusters," in *50th AIAA/ASME/SAE/ASEE Joint Propulsion Conference*. [Online]. Available: https://arc.aiaa.org/doi/abs/10.2514/6.2014-3709

[65] W. Huang, H. Kamhawi, and T. Haag, "Facility effect characterization test of nasa's hermes hall thruster," in *52nd AIAA/SAE/ASEE Joint Propulsion Conference*. [Online]. Available: https://arc.aiaa.org/doi/abs/10.2514/6.2016-4828

[66] M. Nakles and W. Hargus, "Background pressure effects on internal and near-field ion velocity distribution of the bht-600 hall thruster," in *44th AIAA/ASME/SAE/ASEE Joint*

Propulsion Conference & Exhibit. [Online]. Available: https://arc.aiaa.org/doi/abs/10.2514/6.2008-5101

[67] R. Spektor and W. G. Tighe, "Laser induced fluorescence measurements in a hall thruster as a function of background pressure," in *52nd AIAA/SAE/ASEE Joint Propulsion Conference*. [Online]. Available: https://arc.aiaa.org/doi/abs/10.2514/6.2016-4624

[68] D. L. Brown and A. D. Gallimore, "Evaluation of facility effects on ion migration in a hall thruster plume," *Journal of Propulsion and Power*, vol. 27, no. 3, pp. 573–585, 2011.

[69] C. J. Scolese, "Low earth orbit spacecraft charging design handbook," National Aeronautics and Space Administration, Tech. Rep., June 2007, NASA-HDBK-4006.

[70] J. D. Frieman, J. A. Walker, M. L. R. Walker, V. Khayms, and D. Q. King, "Electrical facility effects on hall thruster cathode coupling: Performance and plume properties," *Journal of Propulsion and Power*, vol. 32, no. 1, pp. 251–264, 2016.

[71] J. A. Walker, J. D. Frieman, M. L. R. Walker, V. Khayms, D. King, and P. Y. Peterson, "Electrical facility effects on hall-effect-thruster cathode coupling: Discharge oscillations and facility coupling," *Journal of Propulsion and Power*, vol. 32, no. 4, pp. 844–855, Jul 2016.

[72] J. Dunning and J. Sankovic, "Nasa's electric propulsion program," in *36th AIAA/ASME/SAE/ASEE Joint Propulsion Conference and Exhibit*. [Online]. Available: https://arc.aiaa.org/doi/abs/10.2514/6.2000-3145

[73] S. J. Araki, R. S. Martin, D. Bilyeu, and J. W. Koo, "Sm/murf: Current capabilities and verification as a replacement of afrl plume simulation tool coliseum," ser. AIAA Propulsion and Energy Forum. American Institute of Aeronautics and Astronautics, Jul 2016, 0. [Online]. Available: https://doi.org/10.2514/6.2016-4939

[74] I. D. Boyd, "Numerical modeling of spacecraft electric propulsion thrusters," *Progress in Aerospace Sciences*, vol. 41, no. 8, pp. 669–687, Nov 2005. [Online]. Available: https://www.sciencedirect.com/science/article/pii/S0376042106000029

[75] D. M. Goebel, O. Filimonova, J. R. Anderson, I. Katz, S. Leifer, and J. E. Polk, "Definitive high voltage solar array testing in space and thruster plume plasma environments," in *13th Spacecraft Charging Technology Conference*, June 2014. [Online]. Available: http://www.cosmophysics.ru/Sctc2014/184_Goebel.pdf

[76] H. Bruining, *Physics and Applications of Secondary Electron Emission*. Pergamon, 1962.

[77] N. M. Uchizono, A. L. Collins, C. Marrese-Reading, S. M. Arestie, J. K. Ziemer, and R. E. Wirz, "The role of secondary species emission in vacuum facility effects for electrospray thrusters," *Journal of Applied Physics*, vol. 130, no. 14, p. 143301, 2021.

[78] B. A. Brusilovsky, "Kinetic ion-induced electron emission from the surface of random solids," *Applied Physics A*, vol. 50, no. 1, pp. 111–129, Jan 1990.

[79] S. Y. Lai, A. Brown, J. C. Vickerman, and D. Briggs, "The relationship between electron and ion induced secondary electron imaging: A review with new experimental observations," *Surface and Interface Analysis*, vol. 8, no. 3, pp. 93–111, 1986.

[80] J. Axelsson, C. T. Reimann, and B. U. R. Sundqvist, "Secondary electron emission from surfaces impacted by multiply-charged polyatomic ions," *Nuclear Instruments and Methods in Physics Research Section B: Beam Interactions with Materials and Atoms*, vol. 88, no. 1-2, pp. 131–137, 1994.

[81] J. Axelsson, E. S. Parilis, C. T. Reimann, P. Sullivan, and B. U. R. Sundqvist, "Electron emission from conducting surfaces impacted by multiply-charged polyatomic ions," *Nuclear Instruments and Methods in Physics Research Section B: Beam Interactions with Materials and Atoms*, vol. 101, no. 4, pp. 343–356, 1995.

[82] R. J. Beuhler and L. Friedman, "Threshold studies of secondary electron emission induced by macro-ion impact on solid surfaces," *Nuclear Instruments and Methods*, vol. 170, no. 1-3, pp. 309–315, 1980.

[83] W. O. Hofer, "Emission of atoms and electrons from high-density collision cascades in metals," *Nuclear Instruments and Methods*, vol. 170, no. 1-3, pp. 275–279, 1980.

[84] Y. Xu, Y. K. Bae, R. J. Beuhler, and L. Friedman, "Secondary electron analysis of polymeric ions generated by an electrospray ion source," *The Journal of Physical Chemistry*, vol. 97, no. 46, pp. 11 883–11 886, 1993.

[85] Y. Le Beyec, "Cluster impacts at kev and mev energies: Secondary emission phenomena," *International Journal of Mass Spectrometry and Ion Processes*, vol. 174, no. 1, pp. 101–117, Mar 1998.

[86] M. Gamero-Castaño, "Characterization of the electrosprays of 1-ethyl-3-methylimidazolium bis(trifluoromethylsulfonyl) imide in vacuum," *Physics of Fluids*, vol. 20, no. 3, p. 032103, Mar 2008.

[87] J. Magnusson, A. L. Collins, and R. E. Wirz, "Lifetime considerations for electrospray thrusters," *Aerospace*, 2020.

[88] M. L. Yu, *Charged and excited states of sputtered atoms*. Berlin, Heidelberg: Springer Berlin Heidelberg, 1991.

[89] J. K. Nørskov and B. I. Lundqvist, "Secondary-ion emission probability in sputtering," *Phys. Rev. B*, vol. 19, pp. 5661–5665, Jun 1979. [Online]. Available: https://link.aps.org/doi/10.1103/PhysRevB.19.5661

[90] M. Schlüter, C. Hopf, and W. Jacob, "Chemical sputtering of carbon by combined exposure to nitrogen ions and atomic hydrogen," *New Journal of Physics*, vol. 10, no. 5, p. 053037, May 2008.

[91] E. Sacher, J. F. Currie, and A. Yelon, "Electronegativity effects in chemical sputtering," *Surface Science*, vol. 220, no. 1, pp. L679–L686, Oct 1989.

[92] A. Wucher, "Molecular ionization probability in cluster-sims," *Journal of Vacuum Science & Technology B*, vol. 36, no. 3, p. 03F123, May 2018.

[93] L. Sleno and D. A. Volmer, "Ion activation methods for tandem mass spectrometry," *Journal of Mass Spectrometry*, vol. 39, no. 10, pp. 1091–1112, 2004.

[94] R. G. Cooks, "Special feature: Historical. collision-induced dissociation: Readings and commentary," *Journal of Mass Spectrometry*, vol. 30, no. 9, pp. 1215–1221, 1995.

[95] M. De Silva, A. C. Brown, and A. L. Patrick, "Thermal- and collision-induced dissociation studies of functionalized imidazolium-based ionic liquid cations," *Journal of Mass Spectrometry*, vol. 55, no. 9, p. e4518, Sep 2020.

[96] compiled by Alan D. McNaught and A. Wilkinson, *Compendium of chemical terminology : IUPAC recommendations*. Second edition. Oxford [Oxfordshire] ; Malden, MA : Blackwell Science, 1997., 1997, at head of title: International Union of Pure and Applied Chemistry.;Bibliography: pages 447-450. [Online]. Available: https://search.library.wisc.edu/catalog/999830115402121

[97] R. W. Giese, "Electron-capture mass spectrometry: recent advances," *Journal of chromatography. A*, vol. 892, no. 1-2, pp. 329–346, Sep 2000.

[98] R. C. Dougherty, "Negative chemical ionization mass spectrometry," *Analytical Chemistry*, vol. 53, no. 4, pp. 625–636, Apr 1981.

[99] S. E. Unger, R. J. Day, and R. G. Cooks, "Possitive and negative secondary ion mass spectra and mass-analyzed ion kinetic energy spectra of some amides, amines and related compounds: Mechanisms in molecular sims," *International Journal of Mass Spectrometry and Ion Physics*, vol. 39, no. 2, pp. 231–255, Jul 1981.

[100] J. F. Mahoney, J. Perel, S. A. Ruatta, P. A. Martino, S. Husain, K. Cook, and T. D. Lee, "Massive cluster impact mass spectrometry: A new desorption method for the analysis of large biomolecules," *Rapid Communications in Mass Spectrometry*, vol. 5, no. 10, pp. 441–445, Oct 1991.

[101] J. F. Mahoney, J. Perel, T. D. Lee, P. A. Martino, and P. Williams, "Shock wave model for sputtering biomolecules using massive cluster impacts," *Journal of the American Society for Mass Spectrometry*, vol. 3, no. 4, pp. 311–317, May 1992.

[102] A. Delcorte, O. A. Restrepo, K. Hamraoui, and B. Czerwinski, "Cluster impacts in organics: microscopic models and universal sputtering curves," *Surface and Interface Analysis*, vol. 46, no. S1, pp. 46–50, 2014.

[103] C. Yan and Q. Y. Zhang, "Study on low-energy sputtering near the threshold energy by molecular dynamics simulations," *AIP Advances*, vol. 2, no. 3, p. 032107, Sep 2012. [Online]. Available: https://doi.org/10.1063/1.4738951

[104] S. Rauschenbach, R. Vogelgesang, N. Malinowski, J. W. Gerlach, M. Benyoucef, G. Costantini, Z. Deng, N. Thontasen, and K. Kern, "Electrospray ion beam deposition: Soft-landing and fragmentation of functional molecules at solid surfaces," *ACS Nano*, vol. 3, no. 10, pp. 2901–2910, Oct 2009. [Online]. Available: https://doi.org/10.1021/nn900022p

[105] H.-P. Cheng and U. Landman, "Controlled deposition, soft landing, and glass formation in nanocluster-surface collisions," *Science*, vol. 260, no. 5112, pp. 1304–1307, May 1993. [Online]. Available: https://doi.org/10.1126/science.260.5112.1304

[106] K. Bromann, C. Félix, H. Brune, W. Harbich, R. Monot, J. Buttet, and K. Kern, "Controlled deposition of size-selected silver nanoclusters," *Science*, vol. 274, no. 5289, pp. 956–958, Nov 1996. [Online]. Available: https://doi.org/10.1126/science.274.5289.956

[107] C. O. Reinhold, P. S. Krstic, and S. J. Stuart, "Time scales of chemical sputtering of carbon," *Nuclear Instruments and Methods in Physics Research Section B: Beam*

Interactions with Materials and Atoms, vol. 258, no. 1, pp. 274–277, May 2007. [Online]. Available: https://www.sciencedirect.com/science/article/pii/S0168583X06014042

[108] M. Spearrin, "Introduction to Spectroscopy," Lecture, May 2018, University of California, Los Angeles, MAE252P - Low Temperature Plasmas.

[109] J. E. Field, J. P. Dear, and J. E. Ogren, "The effects of target compliance on liquid drop impact," *Journal of Applied Physics*, vol. 65, no. 2, pp. 533–540, Jan 1989.

[110] M. Gamero-Castaño, "Retarding potential and induction charge detectors in tandem for measuring the charge and mass of nanodroplets," *Review of Scientific Instruments*, vol. 80, no. 5, p. 053301, May 2009.

[111] J. Fernández de la Mora, "On the outcome of the coulombic fission of a charged isolated drop," *Journal of Colloid and Interface Science*, vol. 178, no. 1, pp. 209–218, Mar 1996.

[112] C. Mundo, M. Sommerfeld, and C. Tropea, "Droplet-wall collisions: Experimental studies of the deformation and breakup process," *International Journal of Multiphase Flow*, vol. 21, no. 2, pp. 151–173, Apr 1995.

[113] W. Zhou, D. Loney, F. L. Degertekin, D. W. Rosen, and A. G. Fedorov, "What controls dynamics of droplet shape evolution upon impingement on a solid surface?" *AIChE Journal*, vol. 59, no. 8, pp. 3071–3082, Aug 2013.

[114] X.-H. Li, X.-X. Zhang, and M. Chen, "Estimation of viscous dissipation in nanodroplet impact and spreading," *Physics of Fluids*, vol. 27, no. 5, p. 052007, May 2015.

[115] B.-X. Li, X.-H. Li, and M. Chen, "Spreading and breakup of nanodroplet impinging on surface," *Physics of Fluids*, vol. 29, no. 1, p. 012003, Jan 2017.

[116] J. Koplik and R. Zhang, "Nanodrop impact on solid surfaces," *Physics of Fluids*, vol. 25, no. 2, p. 022003, Feb 2013.

[117] C. W. Visser, P. E. Frommhold, S. Wildeman, R. Mettin, D. Lohse, and C. Sun, "Dynamics of high-speed micro-drop impact: numerical simulations and experiments at frame-to-frame times below 100 ns," *Soft Matter*, vol. 11, no. 9, pp. 1708–1722, 2015.

[118] L. Xu, W. W. Zhang, and S. R. Nagel, "Drop splashing on a dry smooth surface," *Phys. Rev. Lett.*, vol. 94, p. 184505, May 2005.

[119] B. R. Mitchell, T. E. Bate, J. C. Klewicki, Y. P. Korkolis, and B. L. Kinsey, "Experimental investigation of droplet impact on metal surfaces in reduced ambient pressure," *Procedia Manufacturing*, vol. 10, pp. 730–736, Jan 2017.

[120] R. L. Vander Wal, G. M. Berger, and S. D. Mozes, "The splash/non-splash boundary upon a dry surface and thin fluid film," *Experiments in Fluids*, vol. 40, no. 1, pp. 53–59, Jan 2006.

[121] K.-L. Pan and C.-Y. Hung, "Droplet impact upon a wet surface with varied fluid and surface properties," *Journal of Colloid and Interface Science*, vol. 352, no. 1, pp. 186–193, Dec 2010.

[122] A. L. Collins, A. Thuppul, P. L. Wright, N. M. Uchizono, H. Huh, M. J. Davis, J. Ziemer, N. R. Demmons, and R. E. Wirz, "Assessment of grid impingement for electrospray thruster lifetime," in *36th International Electric Propulsion Conference*, ser. IEPC-2019-213, 2019. [Online]. Available: http://electricrocket.org/2019/213.pdf

[123] N. R. Demmons, N. Alvarez, Z. D. Wood, J. Knott, A. Margousian, D. D'Amato, and J. K. Ziemer, "Characterization of life-limiting factors for a colloid micro-newton thruster (CMNT) for the LISA mission," ser. AIAA Propulsion and Energy Forum. American Institute of Aeronautics and Astronautics, Jul 2021.

[124] G. Lenguito, J. Fernandez de la Mora, and A. Gomez, "Scaling up the power of an electrospray microthruster," *Journal of Micromechanics and Microengineering*, vol. 24, no. 5, p. 055003, Apr 2014.

[125] C. Marrese-Reading, J. Ziemer, M. Gamero-Castano, D. Bame, N. Demmons, and V. Hruby, "Plasma potential measurements in the plume of a colloid micro-newton thruster," in *42nd AIAA/ASME/SAE/ASEE Joint Propulsion Conference & Exhibit*, 2006.

[126] K. J. Terhune, L. B. King, K. He, and J. Cumings, "Radiation-induced solidification of ionic liquid under extreme electric field," *Nanotechnology*, vol. 27, no. 37, p. 375701, Aug 2016.

[127] P. Kidd and H. Shelton, "Life test (4350 hours) of an advanced colloid thruster module," ser. International Electric Propulsion Conference. American Institute of Aeronautics and Astronautics, Oct 1973.

[128] T. Coles, T. Fedkiw, and P. Lozano, "Investigating ion fragmentation in electrospray thruster beams," ser. Joint Propulsion Conferences. American Institute of Aeronautics and Astronautics, Jul 2012.

[129] C. Ma and C. Ryan, "Plume particle energy analysis of an ionic liquid electrospray ion source with high emission density," *Journal of Applied Physics*, vol. 129, no. 8, p. 083302, Feb 2021.

[130] M. Klosterman, J. Rovey, and D. A. Levin, "Ion-induced electron emission from EMIM-BF4 electrospray plume-surface interactions," in *AIAA SciTech Forum*. American Institute of Aeronautics and Astronautics, Jan 2021. [Online]. Available: https://doi.org/10.2514/6.2021-1975

[131] H. Huh and R. E. Wirz, "Numerical simulation of electrospray extraction for highly conductive propellants," in *36th International Electric Propulsion Conference*, ser. IEPC-2019-565, 2019. [Online]. Available: http://electricrocket.org/2019/565.pdf

[132] B. Ferda, "Retarding potential analyzer theory and design," 2015. [Online]. Available: https://w3.pppl.gov/ppst/docs/ferda.pdf

[133] E. M. Petro, M. Cezairli, M. Schroeder, and P. C. Lozano, "Investigation of electrospray plume composition during voltage transients," in *36th International Electric Propulsion Conference*, ser. IEPC-2019-794, 2019. [Online]. Available: https://electricrocket.org/2019/794.pdf

[134] P. Lozano, "Studies on the ion-droplet mixed regime in colloid thrusters," Ph.D. dissertation, Massachusetts Institute of Technology, 2003.

[135] M. J. Breddan, D. R. Curry, M. Sharma, M. O. Richmond, A. L. Collins, L. Brieda, and R. E. Wirz, "Electrospray plume modeling: Study on drag influence," ser. AIAA SciTech Forum. American Institute of Aeronautics and Astronautics, Dec 2021. [Online]. Available: https://doi.org/10.2514/6.2022-1358

[136] M. Gamero-Castaño and M. Galobardes-Esteban, "Electrospray propulsion: Modeling of the beams of droplets and ions of highly conducting propellants," *Journal of Applied Physics*, vol. 131, no. 1, p. 013307, Jan 2022. [Online]. Available: https://doi.org/10.1063/5.0073380

[137] F. F. Chen, "Lecture notes on langmuir probe diagnostics," ser. IEEE-ICOPS. Institute of Electrical and Electronics Engineers, Jun 2003. [Online]. Available: https://www.seas.ucla.edu/~ffchen/Publs/Chen210R.pdf

[138] H. M. Mott-Smith and I. Langmuir, "The theory of collectors in gaseous discharges," *Phys. Rev.*, vol. 28, pp. 727–763, Oct 1926.

[139] M. Baird, R. McGee-Sinclair, K. Lemmer, and W. Huang, "Time-resolved ion energy measurements using a retarding potential analyzer," *Review of Scientific Instruments*, vol. 92, no. 7, p. 073306, Jul 2021. [Online]. Available: https://doi.org/10.1063/5.0039621

[140] S. T. Lai and C. Miller, "Retarding potential analyzer: Principles, designs, and space applications," *AIP Advances*, vol. 10, no. 9, p. 095324, Sep 2020. [Online]. Available: https://doi.org/10.1063/5.0014266

[141] C. L. Enloe, "High-resolution retarding potential analyzer," *Review of Scientific Instruments*, vol. 65, no. 2, pp. 507–508, Feb 1994. [Online]. Available: https://doi.org/10.1063/1.1145167

[142] K. L. Busch, "Detecting ions in mass spectrometers with the faraday cup," *Spectroscopy*, vol. 26, no. 11, Nov 2011. [Online]. Available: https://www.spectroscopyonline.com/view/detecting-ions-mass-spectrometers-faraday-cup

[143] R. P. Doerner, D. G. Whyte, and D. M. Goebel, "Sputtering yield measurements during low energy xenon plasma bombardment," *Journal of Applied Physics*, vol. 93, no. 9, pp. 5816–5823, May 2003, https://doi.org/10.1063/1.1566474.

[144] A. Thuppul, A. L. Collins, P. L. Wright, N. M. Uchizono, and R. E. Wirz, "Mass flux and current density distributions of electrospray plumes," *Journal of Applied Physics*, vol. 130, no. 10, p. 103301, Sep 2021.

[145] SpecialChem. Volume resistivity - electrical properties of polymers. [Online]. Available: https://omnexus.specialchem.com/polymer-properties/properties/volume-resistivity

[146] Pasternack. Flexible rg-58 coax cable. [Online]. Available: https://www.pasternack.com/images/ProductPDF/RG58C-U.pdf

[147] M. J. Druyvesteyn, "Der niedervoltbogen," *Zeitschrift für Physik*, vol. 64, no. 11, pp. 781–798, Sep 1930. [Online]. Available: https://doi.org/10.1007/BF01773007

[148] R. B. Lobbia and B. E. Beal, "Recommended practice for use of langmuir probes in electric propulsion testing," *Journal of Propulsion and Power*, vol. 33, no. 3, pp. 566–581, May 2017. [Online]. Available: https://doi.org/10.2514/1.B35531

[149] G. Z. Li and R. E. Wirz, "Persistent sputtering yield reduction in plasma-infused foams," *Phys. Rev. Lett.*, vol. 126, p. 035001, Jan 2021. [Online]. Available: https://link.aps.org/doi/10.1103/PhysRevLett.126.035001

[150] A. Thuppul, A. L. Collins, P. L. Wright, N. M. Uchizono, and R. E. Wirz, "Spatially-resolved mass flux and current measurements of electrospray plumes," in *36th International Electric Propulsion Conference*, ser. IEPC-2019-571, 2019. [Online]. Available: http://electricrocket.org/2019/571.pdf

[151] A. L. Collins, P. L. Wright, N. M. Uchizono, and R. E. Wirz, "Neutral mass flux measurements of an electrospray plume," in *37th International Electric Propulsion Conference*, ser. IEPC-2022-227, 2022.

[152] P. Wright and R. E. Wirz, "Transient flow in porous electrospray emitters," ser. AIAA Propulsion and Energy Forum. American Institute of Aeronautics and Astronautics, Jul 2021. [Online]. Available: https://doi.org/10.2514/6.2021-3437

[153] N. M. Uchizono, A. L. Collins, P. L. Wright, and R. E. Wirz, "Electrospray thruster facility effects: Characterization and mitigation," in *37th International Electric Propulsion Conference*, ser. IEPC-2022-219, 2022.

[154] C. S. Tedmon, D. A. Vermilyea, and J. H. Rosolowski, "Intergranular corrosion of austenitic stainless steel," *Journal of The Electrochemical Society*, vol. 118, no. 2, p. 192, 1971. [Online]. Available: https://doi.org/10.1149/1.2407966

[155] M. Tariq, P. J. Carvalho, J. A. Coutinho, I. M. Marrucho, J. N. C. Lopes, and L. P. Rebelo, "Viscosity of (c2–c14) 1-alkyl-3-methylimidazolium bis(trifluoromethylsulfonyl)amide ionic liquids in an extended temperature range," *Fluid Phase Equilibria*, vol. 301, no. 1, pp. 22–32, Feb 2011.

[156] H. Tokuda, K. Hayamizu, K. Ishii, M. A. B. H. Susan, and M. Watanabe, "Physicochemical properties and structures of room temperature ionic liquids. 2. variation of alkyl chain length in imidazolium cation," *The Journal of Physical Chemistry B*, vol. 109, no. 13, pp. 6103–6110, Apr 2005.

[157] C. M. S. S. Neves, K. A. Kurnia, J. A. P. Coutinho, I. M. Marrucho, J. N. C. Lopes, M. G. Freire, and L. P. N. Rebelo, "Systematic study of the thermophysical properties of imidazolium-based ionic liquids with cyano-functionalized anions," *The Journal of Physical Chemistry B*, vol. 117, no. 35, pp. 10 271–10 283, Sep 2013.

[158] J. Vila, B. Fernández-Castro, E. Rilo, J. Carrete, M. Domínguez-Pérez, J. R. Rodríguez, M. García, L. M. Varela, and O. Cabeza, "Liquid–solid–liquid phase transition hysteresis loops in the ionic conductivity of ten imidazolium-based ionic liquids," *Fluid Phase Equilibria*, vol. 320, pp. 1–10, Apr 2012.

[159] F. J. Higuera, "Model of the meniscus of an ionic-liquid ion source," *Phys. Rev. E*, vol. 77, p. 026308, Feb 2008. [Online]. Available: https://link.aps.org/doi/10.1103/PhysRevE.77.026308

[160] M. Gamero-Castaño, "Dissipation in cone-jet electrosprays and departure from isothermal operation," *Phys. Rev. E*, vol. 99, p. 061101, Jun 2019.

[161] M. Magnani and M. Gamero, "Modeling of ion emission from a liquid meniscus," in *AIAA Propulsion and Energy 2021 Forum*. [Online]. Available: https://arc.aiaa.org/doi/abs/10.2514/6.2021-3434

[162] Y. Chen, Y. Cao, Y. Shi, Z. Xue, and T. Mu, "Quantitative research on the vaporization and decomposition of [emim][tf2n] by thermogravimetric analysis–mass spectrometry," *Industrial & Engineering Chemistry Research*, vol. 51, no. 21, pp. 7418–7427, May 2012. [Online]. Available: https://doi.org/10.1021/ie300247v

[163] H. Luo, G. A. Baker, and S. Dai, "Isothermogravimetric determination of the enthalpies of vaporization of 1-alkyl-3-methylimidazolium ionic liquids," *The Journal of Physical Chemistry B*, vol. 112, no. 33, pp. 10 077–10 081, Aug 2008. [Online]. Available: https://doi.org/10.1021/jp805340f

[164] K. Chatterjee, A. Hazra, D. Dollimore, and K. S. Alexander, "Estimating vapor pressure curves by thermogravimetry: a rapid and convenient method for characterization of pharmaceuticals," *European Journal of Pharmaceutics and Biopharmaceutics*, vol. 54, no. 2, pp. 171–180, Sep 2002.

[165] I. Langmuir, "The vapor pressure of metallic tungsten," *Phys. Rev.*, vol. 2, pp. 329–342, Nov 1913.

[166] J. Rojas-Herrera, I. Jivanescu, D. Freeman, D. Krejci, C. Fucetola, and L. Paulo, "Porous materials for ion-electrospray spacecraft microengines," *Journal of Nanomechanics and Micromechanics*, vol. 7, no. 3, p. 04017006, Sep 2017.

[167] S. M. Arestie, "Porous material and process development for electrospray propulsion applications," Master's thesis, Massachusetts Institute of Technology, 2014.

[168] K. Guo, Z. Hu, H. Song, X. Du, L. Zhong, and X. Chen, "Low-density graphene/carbon composite aerogels prepared at ambient pressure with high mechanical strength and low thermal conductivity," *RSC Advances*, vol. 5, no. 7, pp. 5197–5204, 2015.

[169] F. Hemberger, S. Weis, G. Reichenauer, and H.-P. Ebert, "Thermal transport properties of functionally graded carbon aerogels," *International Journal of Thermophysics*, vol. 30, no. 4, pp. 1357–1371, Aug 2009.

[170] M. Tajmar, "Development of a lifetime prediction model for indium FEEP thrusters," in *Joint Propulsion Conferences*. American Institute of Aeronautics and Astronautics, Jul 2005.

[171] J. F. d. l. Mora, G. J. Van Berkel, C. G. Enke, R. B. Cole, M. Martinez-Sanchez, and J. B. Fenn, "Electrochemical processes in electrospray ionization mass spectrometry," *Journal of Mass Spectrometry*, vol. 35, no. 8, pp. 939–952, Aug 2000.

[172] M. Shirai, T. Tanigaki, S. Aizawa, H. S. Park, T. Matsuda, and D. Shindo, "In situ electron holographic study of ionic liquid," *Ultramicroscopy*, vol. 146, pp. 125–129, Nov 2014.

[173] B. L. P. Gassend, "A fully microfabricated two-dimensional electrospray array with applications to space propulsion," Ph.D. dissertation, Massachusetts Institute of Technology, 2007.

[174] L. Grimaud, D. Krejci, and B. Seifert, "The IFM Micro FEEP thruster: a modular design for smallsat propulsion," in *36th International Electric Propulsion Conference*, ser. IEPC-2019-A675, 2019.

[175] A. Bogaerts, *Glow Discharge Mass Spectrometry, Methods*. Oxford: Elsevier, Jan 1999.

[176] I. G. Loscertales and J. Fernández de la Mora, "Experiments on the kinetics of field evaporation of small ions from droplets," *The Journal of Chemical Physics*, vol. 103, no. 12, pp. 5041–5060, Sep 1995.

[177] W. D. Luedtke, U. Landman, Y.-H. Chiu, D. J. Levandier, R. A. Dressler, S. Sok, and M. S. Gordon, "Nanojets, electrospray, and ion field evaporation: Molecular dynamics simulations and laboratory experiments," *The Journal of Physical Chemistry A*, vol. 112, no. 40, pp. 9628–9649, Oct 2008.

[178] N. M. Uchizono, A. L. Collins, A. Thuppul, P. L. Wright, D. Q. Eckhardt, J. Ziemer, and R. E. Wirz, "Emission modes in electrospray thrusters operating with high conductivity ionic liquids," *Aerospace*, vol. 7, no. 10, 2020.

[179] R. E. Wirz, A. L. Collins, A. Thuppul, P. L. Wright, N. M. Uchizono, M. J. Davis, J. K. Ziemer, and N. R. Demmons, "Electrospray thruster performance and lifetime investigation for the lisa mission," ser. AIAA Propulsion and Energy Forum. American Institute of Aeronautics and Astronautics, Aug 2019. [Online]. Available: https://doi.org/10.2514/6.2019-3816

[180] A. Kramida, Yu. Ralchenko, J. Reader, and and NIST ASD Team, NIST Standard Reference Database Number 78, Atomic Spectra Database (ver. 5.9), [Online]. Available: https://physics.nist.gov/asd [2022, April 4]. National Institute of Standards and Technology, Gaithersburg, MD.

[181] G. Garcia-Cosio, H. Martinez, M. Calixto-Rodriguez, and A. Gomez, "Dc discharge experiment in an ar/n2/co2 ternary mixture: A laboratory simulation of the martian ionosphere's plasma environment," *Journal of Quantitative Spectroscopy and Radiative Transfer*, vol. 112, no. 18, pp. 2787–2793, Dec 2011.

[182] A. Yanguas-Gil, J. L. Hueso, J. Cotrino, A. Caballero, and A. R. González-Elipe, "Reforming of ethanol in a microwave surface-wave plasma discharge," *Applied Physics Letters*, vol. 85, no. 18, pp. 4004–4006, Nov 2004.

[183] Y. Li, R. Zhou, F. Qi, D. Zhou, R. Zhou, J. Wan, Y. Xian, P. J. Cullen, X. Lu, and K. K. Ostrikov, "Plasma-enabled liquid ethanol conversion for hydrogen production: discharge characteristics and process control," *Journal of Physics D: Applied Physics*, vol. 53, no. 17, p. 174001, Feb 2020.

[184] S. M. Parmar, A. L. Collins, and R. E. Wirz, "Electrospray plume modeling for rapid life and performance analysis," ser. AIAA SciTech Forum. American Institute of Aeronautics and Astronautics, Dec 2021. [Online]. Available: https://doi.org/10.2514/6.2022-1357

[185] N. Nuwal, V. A. Azevedo, M. R. Klosterman, S. Budaraju, D. A. Levin, and J. L. Rovey, "Multiscale modeling of fragmentation in an electrospray plume," *Journal of Applied Physics*, vol. 130, no. 18, p. 184903, Nov 2021. [Online]. Available: https://doi.org/10.1063/5.0064711

[186] H. Huh and R. E. Wirz, "Electrohydrodynamic simulation of electrospray thruster extraction," ser. AIAA SciTech Forum. American Institute of Aeronautics and Astronautics, Dec 2021. [Online]. Available: https://doi.org/10.2514/6.2022-1359

[187] T. Fedkiw, Z. D. Wood, and N. R. Demmons, "Environmental and lifetime testing of the bet-300-p electrospray thruster," ser. AIAA Propulsion and Energy Forum. American Institute of Aeronautics and Astronautics, Aug 2020. [Online]. Available: https://doi.org/10.2514/6.2020-3614

[188] J. R. Brophy, "Nasa's deep space 1 ion engine (plenary)," *Review of Scientific Instruments*, vol. 73, no. 2, pp. 1071–1078, Feb 2002. [Online]. Available: https://doi.org/10.1063/1.1432470

[189] Hamamatsu, *Photomultiplier Tubes, Basics and Applications*. Hamamatsu, 2017. [Online]. Available: https://www.hamamatsu.com/content/dam/hamamatsu-photonics/sites/documents/99_SALES_LIBRARY/etd/PMT_handbook_v4E.pdf

[190] G. R. Lewis, C. S. Arridge, D. R. Linder, L. K. Gilbert, D. O. Kataria, A. J. Coates, A. Persoon, G. A. Collinson, N. André, P. Schippers, J. Wahlund, M. Morooka, G. H. Jones, A. M. Rymer, D. T. Young, D. G. Mitchell, A. Lagg, and S. A. Livi, "The calibration of the cassini–huygens caps electron spectrometer," *Planetary and Space Science*, vol. 58, no. 3, pp. 427–436, Feb 2010. [Online]. Available: https://www.sciencedirect.com/science/article/pii/S0032063309003535

[191] G. A. Collinson, J. C. Dorelli, L. A. Avanov, G. R. Lewis, T. E. Moore, C. Pollock, D. O. Kataria, R. Bedington, C. S. Arridge, D. J. Chornay, U. Gliese, A. Mariano, A. C. Barrie, C. Tucker, C. J. Owen, A. P. Walsh, M. D. Shappirio, and M. L. Adrian, "The geometric factor of electrostatic plasma analyzers: A case study from the fast plasma investigation for the magnetospheric multiscale mission," *Review of Scientific Instruments*, vol. 83, no. 3, p. 033303, Mar 2012. [Online]. Available: https://doi.org/10.1063/1.3687021

[192] R. L. Kessel, A. D. Johnstone, A. J. Coates, and R. A. Gowen, "Space plasma measurements with ion instruments," *Review of Scientific Instruments*, vol. 60, no. 12, pp. 3750–3761, Dec 1989. [Online]. Available: https://doi.org/10.1063/1.1141075

[193] A. D. Johnstone, A. J. Coates, B. Wilken, W. Studemann, W. Weiss, R. C. Irelli, V. Formisano, H. Borg, S. Olsen, J. D. Winningham, D. A. Bryant, and S. J. Kellock, "The giotto three-dimensional positive ion analyser," *Journal of Physics E: Scientific Instruments*, vol. 20, no. 6, pp. 795–805, jun 1987. [Online]. Available: https://doi.org/10.1088/0022-3735/20/6/038

[194] G. A. Collinson, D. O. Kataria, A. J. Coates, S. M. E. Tsang, C. S. Arridge, G. R. Lewis, R. A. Frahm, J. D. Winningham, and S. Barabash, "Electron optical study of the venus express ASPERA-4 electron spectrometer (ELS) top-hat electrostatic analyser," *Measurement Science and Technology*, vol. 20, no. 5, p. 055204, apr 2009. [Online]. Available: https://doi.org/10.1088/0957-0233/20/5/055204

[195] P. D. G. de Melo, I. H. Tan, J. J. Barroso, and R. S. Dallaqua, "Numerical simulation of the geometric factor of a cylindrical electrostatic analyzer to monitor electron precipitation in the south atlantic magnetic anomaly," *IEEE Transactions on Plasma Science*, vol. 44, no. 6, pp. 1009–1017, 2016. [Online]. Available: https://doi.org/10.1109/TPS.2016.2558320

[196] N. M. Uchizono, A. L. Collins, C. Marrese-Reading, S. M. Arestie, J. K. Ziemer, and R. E. Wirz, "Positive and negative secondary species emission behavior for an ionic liquid electrospray," *Applied Physics Letters (Submitted)*, 2022.

[197] N. M. Uchizono, R. E. Wirz, A. L. Collins, C. Marrese-Reading, S. M. Arestie, and J. K. Ziemer, "A diagnostic for quantifying secondary species emission from electrospray devices," *Review of Scientific Instruments (Submitted)*, 2022.

[198] A. Genovese, M. Tajmar, and W. Steiger, "Indium FEEP endurance test: Preliminary results," in *27th International Electric Propulsion Conference*, ser. IEPC-01-289, Pasadena, CA, 2001.

[199] W. Samenfink, A. Elsäßer, K. Dullenkopf, and S. Wittig, "Droplet interaction with shear-

driven liquid films: analysis of deposition and secondary droplet characteristics," *International Journal of Heat and Fluid Flow*, vol. 20, no. 5, pp. 462–469, Oct 1999.

[200] R. Schmehl, H. Rosskamp, M. Willmann, and S. Wittig, "Cfd analysis of spray propagation and evaporation including wall film formation and spray/film interactions," *International Journal of Heat and Fluid Flow*, vol. 20, no. 5, pp. 520–529, Oct 1999.

[201] R. Honsek, W. G. Habashi, and M. S. Aubé, "Eulerian modeling of in-flight icing due to supercooled large droplets," *Journal of Aircraft*, vol. 45, no. 4, pp. 1290–1296, Jul 2008.

[202] L. Zhang, T. Ku, X. Cheng, Y. Song, and D. Zhang, "Inkjet droplet deposition dynamics into square microcavities for oleds manufacturing," *Microfluidics and Nanofluidics*, vol. 22, no. 4, p. 47, Apr 2018.

[203] A. Zolfaghari, T. Chen, and A. Y. Yi, "Additive manufacturing of precision optics at micro and nanoscale," vol. 1, no. 1, p. 012005, apr 2019.

[204] A. P. Fröba, H. Kremer, and A. Leipertz, "Density, refractive index, interfacial tension, and viscosity of ionic liquids [emim][etso4], [emim][ntf2], [emim][n(cn)2], and [oma][ntf2] in dependence on temperature at atmospheric pressure," *The Journal of Physical Chemistry B*, vol. 112, no. 39, pp. 12 420–12 430, Oct 2008. [Online]. Available: https://doi.org/10.1021/jp804319a

[205] C. Schreiner, S. Zugmann, R. Hartl, and H. J. Gores, "Fractional walden rule for ionic liquids: Examples from recent measurements and a critique of the so-called ideal kcl line for the walden plot," *Journal of Chemical & Engineering Data*, vol. 55, no. 5, pp. 1784–1788, May 2010. [Online]. Available: https://doi.org/10.1021/je900878j

[206] M. Geppert-Rybczyńska, J. K. Lehmann, and A. Heintz, "Surface tensions and the gibbs excess surface concentration of binary mixtures of the ionic liquid 1-ethyl-3-methylimidazolium bis[(trifluoromethyl)sulfonyl]imide with tetrahydrofuran and

acetonitrile," *Journal of Chemical & Engineering Data*, vol. 56, no. 4, pp. 1443–1448, Apr 2011. [Online]. Available: https://doi.org/10.1021/je101146f

[207] S. Zhang, N. Sun, X. He, X. Lu, and X. Zhang, "Physical properties of ionic liquids: Database and evaluation," *Journal of Physical and Chemical Reference Data*, vol. 35, no. 4, pp. 1475–1517, Dec 2006.

[208] J. Pitawala, J. Scheers, P. Jacobsson, and A. Matic, "Physical properties, ion–ion interactions, and conformational states of ionic liquids with alkyl-phosphonate anions," *The Journal of Physical Chemistry B*, vol. 117, no. 27, pp. 8172–8179, Jul 2013.

[209] C. Daguenet, P. J. Dyson, I. Krossing, A. Oleinikova, J. Slattery, C. Wakai, and H. Weingärtner, "Dielectric response of imidazolium-based room-temperature ionic liquids," *The Journal of Physical Chemistry B*, vol. 110, no. 25, pp. 12 682–12 688, Jun 2006. [Online]. Available: https://doi.org/10.1021/jp0604903

[210] T. Singh and A. Kumar, "Static dielectric constant of room temperature ionic liquids: Internal pressure and cohesive energy density approach," *The Journal of Physical Chemistry B*, vol. 112, no. 41, pp. 12 968–12 972, Oct 2008.

[211] M. Dzida, E. Zorębski, M. Zorębski, M. Żarska, M. Geppert-Rybczyńska, M. Chorążewski, J. Jacquemin, and I. Cibulka, "Speed of sound and ultrasound absorption in ionic liquids," *Chemical Reviews*, vol. 117, no. 5, pp. 3883–3929, Mar 2017.

[212] H. Zarei and V. Keley, "Density and speed of sound of binary mixtures of ionic liquid 1-ethyl-3-methylimidazolium tetrafluoroborate, n,n-dimethylformamide, and n,n-dimethylacetamide at temperature range of 293.15–343.15 k: Measurement and pc-saft modeling," *Journal of Chemical & Engineering Data*, vol. 62, no. 3, pp. 913–923, Mar 2017.

[213] J. P. Armstrong, C. Hurst, R. G. Jones, P. Licence, K. R. J. Lovelock, C. J. Satterley, and

I. J. Villar-Garcia, “Vapourisation of ionic liquids,” *Phys. Chem. Chem. Phys.*, vol. 9, pp. 982–990, 2007.

[214] A. Deyko, K. R. J. Lovelock, J.-A. Corfield, A. W. Taylor, P. N. Gooden, I. J. Villar-Garcia, P. Licence, R. G. Jones, V. G. Krasovskiy, E. A. Chernikova, and L. M. Kustov, “Measuring and predicting vaph298 values of ionic liquids,” *Phys. Chem. Chem. Phys.*, vol. 11, pp. 8544–8555, 2009.